

**TECTONIC AND MAGMATIC CONTROLS ON EXTENSION AND CRUSTAL
ACCRETION IN BACKARC BASINS, INSIGHTS FROM THE LAU BASIN AND
SOUTHERN MARIANA TROUGH**

A DISSERTATION SUBMITTED TO THE GRADUATE DIVISION OF THE UNIVERSITY
OF HAWAI‘I AT MĀNOA IN PARTIAL FULFILLMENT OF THE REQUIREMENTS FOR
THE DEGREE OF

DOCTOR OF PHILOSOPHY
IN
GEOLOGY AND GEOPHYSICS

MAY 2017

By

Jonathan D. Sleeper

Dissertation Committee:

Fernando Martinez, Chairperson

Patricia Fryer

Richard Hey

Michael J. Mottl

John Sinton

Keywords: Lau Basin; Mariana Trough; backarc basin; seafloor spreading; subduction zone

ACKNOWLEDGEMENTS

I would like to express my gratitude and appreciation to all those who have supported, helped, and encouraged me throughout this long journey. First and foremost, I would like to thank my advisor, Fernando, for his constant support, advice, and patience throughout the nearly nine years that we worked together on both my Master's and Doctoral projects. I learned more from my conversations with him over the years than all of the classes I've taken or papers that I have read, and no one else has had a greater influence on the scientist that I have become. Thank you also to my committee members, Drs. Patricia Fryer, Richard Hey, Michael J. Mottl, and John Sinton, for their support and advice to improve this dissertation. I also would like to thank the teachers that I have had throughout my career as a geologist, both from San Jose State University, where my educational foundation in geology was laid, and at UH Mānoa, where my horizons expanded beyond the realm of continental geology to the depths of the oceans and the large-scale processes of plate tectonics. I would also like to thank all of the administrative staff at UH who have helped me with the sometimes complicated logistical aspects of grad school: Lily, Grace, Susan, Evelyn, Alison, Leona, Marcie, and others who I'm sure I missed. On a personal level, I would like to thank my family for their constant support and advice to help me get through this challenging period of my life. Thank you to all of my friends that I have made throughout my time here at UH for the support and the good memories that will last a lifetime, and to my old friends who have been there since before I ever considered going to graduate school. Mahalo to all!

ABSTRACT

This dissertation examines magmatic and tectonic processes in backarc basins, and how they are modulated by plate- and mantle-driven mechanisms. Backarc basins initiate by tectonic rifting near the arc volcanic front and transition to magmatic seafloor spreading. As at mid-ocean ridges (MORs), spreading can be focused in narrow plate boundary zones, but we also describe a diffuse spreading mode particular to backarc basins. At typical MORs away from hot spots and other melting anomalies, spreading rate is the primary control on the rate of mantle upwelling and decompression melting. At backarc spreading centers, water derived from the subducting slab creates an additional mantle-driven source of melt and buoyant upwelling. Furthermore, because basins open primarily in response to trench rollback, which is inherently a non-rigid process, backarc extensional systems often have to respond to a constantly evolving stress regime, generating complex tectonics and unusual plate boundaries not typically found at MORs. The interplay between these plate- and mantle-driven processes gives rise to the variety of tectonic and volcanic morphologies peculiar to backarc basins.

Chapter 2 is focused on the Fonualei Rift and Spreading Center in the Lau Basin. The southern portion of the axis is spreading at ultraslow (<20 mm/yr) opening rates in close proximity to the arc volcanic front and axial morphology abruptly changes from a volcanic ridge to spaced volcanic cones resembling arc volcanoes. Spreading rate and arc proximity appear to control transitions between two-dimensional and three-dimensional mantle upwelling and volcanism. In the second study (Chapter 3), I develop a new model for the rollback-driven kinematic and tectonic evolution of the Lau Basin, where microplate tectonics creates rapidly changing plate boundary configurations. The third study (Chapter 4) focuses on the southern Mariana Trough and the transitions between arc rifting, seafloor spreading, and a new mode of "diffuse spreading," where new crust is accreted in broad zones rather than along a narrow spreading axis, apparently controlled by a balance between slab water addition and its extraction due to melting and crustal accretion.

TABLE OF CONTENTS

Acknowledgements	i
Abstract	ii
List of tables	vi
List of figures	vii
List of abbreviations and symbols.....	ix
Chapter 1. Introduction	1
1.1 Overview	1
1.2 Background	1
1.3 Dissertation structure and chapter summaries	5
Chapter 2. The Fonualei Rift and Spreading Center: Effects of ultraslow spreading and arc proximity on backarc crustal accretion	10
2.1 Introduction	11
2.2 Geologic setting and background	13
2.2.1 Northeast Lau Basin	13
2.2.2 The Fonualei Rift and Spreading Center	13
2.3 Methodology	15
2.3.1 Geophysical data sets and processing	15
2.3.2 FRSC axial segmentation	17
2.3.3 Gravity data	19
2.4 Observations and results	19
2.4.1 FRSC morphology: Segment-by-segment descriptions	19
2.4.1.1 Arc-distal segments: MTJ-S1 and MTJ-S2	21
2.4.1.2 Transitional segments: FRSC1 and FRSC2	21
2.4.1.3 Arc-proximal segments: FRSC3 and FRSC4	23
2.4.1.4 Arc-like segments: FRSC5 and FRSC6	25
2.4.2 Gravity anomalies	25
2.5 Discussion	27
2.5.1 General trends with arc proximity, comparison with ELSC/VFR	27
2.5.1.1 FRSC-S morphology: Along-axis melt focusing due to ultraslow spreading rates?	29

2.5.1.2	FRSC-S morphology: Rifting versus spreading?	31
2.5.1.3	Morphologic correlations with the arc	31
2.5.1.4	Geochemical correlations with the arc	33
2.5.1.5	Arc-distal segments	33
2.5.1.6	Morphologic correlations with hot spot-proximal ridges	36
2.5.2	Model of mantle wedge structure	36
2.5.3	Opening rate effects on the volcanic expression of backarc crustal accretion	37
2.6	Conclusions	40
Chapter 3.	Geology and kinematics of the Niufo'ou microplate in the northern Lau Basin ..	42
3.1	Introduction	43
3.2	Tectonic setting and kinematics	44
3.2.1	Present-day tectonics in the Lau Basin	44
3.2.2	Lau Basin kinematics	46
3.3	Geophysical data sets and processing	48
3.4	Plate boundary observations and interpretations	50
3.4.1	Niufo'ou-Tonga plate boundary: Morphologic evidence for slower spreading rates	51
3.4.1.1	Niufo'ou-Tonga plate boundary: Magnetic anomaly modeling and a new Euler pole	51
3.4.1.2	Model setup and Euler pole location	53
3.4.1.3	Magnetic modeling results: Slow to ultraslow spreading along the FRSC/MTJ-S	54
3.4.2	Central Lau Spreading Center, Lau Extensional Transform Zone, Peggy Ridge, and the nature of the Australia-Niufo'ou plate boundary	57
3.4.2.1	Central Lau Spreading Center morphology	58
3.4.2.2	Central Lau Spreading Center opening rates	60
3.4.2.3	Lau Extensional Transform Zone: Extensional structures	63
3.4.2.4	Lau Extensional Transform Zone: Strike-slip structures	65
3.4.3	Australia-Tonga plate boundary: Evidence for increasing opening rates over time	67

3.5	Lau Basin kinematic model	68
3.5.1	New Lau Basin three-plate kinematic model	68
3.5.2	Niuafu'ou-Tonga southern boundary and the Niuatoputapu plate	75
3.5.3	The nature of Peggy Ridge and insights into A-N boundary evolution	76
3.5.4	Implications for rigid plate models and the dynamic nature of backarc basins	77
3.6	Conclusions	78
Chapter 4. Diffuse spreading, a new mode of crustal accretion in the southern Mariana Trough backarc basin		80
4.1	Introduction	81
4.2	Geologic background: southern Mariana Trough	82
4.2.1	Mariana Trough opening and tectonics	82
4.2.2	Volcanism in the southern Mariana Trough	86
4.3	Methodology: Geophysical data sets and processing	89
4.4	Observations and results	90
4.4.1	Southwest Mariana Rift morphology	91
4.4.2	Diffuse volcanic zone morphology	93
4.4.3	MGR flank “organized spreading” morphology	98
4.4.4	Seismicity in the southern Mariana Trough	100
4.5	Discussion	101
4.5.1	Summary of observations on the mode of opening in the southern Mariana Trough	102
4.5.2	Diffuse spreading vs. segmented rifting	103
4.5.3	Diffuse spreading vs. organized spreading	106
4.5.4	Hydrous lithosphere model	107
4.5.5	Melt production within the DSZ: Passive plate-driven melting vs. active buoyancy-driven melting	109
4.6	Conclusions	110
Chapter 5. Conclusion		112
References		114

LIST OF TABLES

<i>Table 2.1:</i> FRSC/MTJ-S segment measurements and statistics	41
<i>Table 3.1:</i> GPS velocities, predicted velocities, and predicted spreading rates	71

LIST OF FIGURES

<i>Figure 1.1:</i> Conceptual 3-D model of mantle wedge structure	4
<i>Figure 1.2:</i> Compiled bathymetric map of the Lau Basin	6
<i>Figure 1.3:</i> Compiled bathymetric map of the southern Mariana Trough	8
<i>Figure 2.1:</i> Lau Basin location map	14
<i>Figure 2.2:</i> Compiled bathymetry map of the northeast Lau Basin	16
<i>Figure 2.3:</i> Geophysical data along the FRSC/MTJ-S	18
<i>Figure 2.4:</i> MTJ-S morphology	20
<i>Figure 2.5:</i> FRSC-N morphology	22
<i>Figure 2.6:</i> FRSC-C morphology	24
<i>Figure 2.7:</i> FRSC-S morphology	26
<i>Figure 2.8:</i> Mantle Bouguer anomaly	28
<i>Figure 2.9:</i> Bathymetry maps comparing type examples of FRSC/MTJ-S morphology and ELSC/VFR morphology	30
<i>Figure 2.10:</i> Oblique Mercator bathymetry map of the FRSC/MTJ-S	32
<i>Figure 2.11:</i> Side-by-side comparison of on- and off-axis morphology	35
<i>Figure 2.12:</i> Schematic maps comparing the simplified morphology of the arc volcanic front and backarc in four different regions	39
<i>Figure 3.1:</i> Lau Basin bathymetry and location map	45
<i>Figure 3.2:</i> Zellmer and Taylor [2001] three-plate kinematic model	47
<i>Figure 3.3:</i> Geophysical data along the FRSC/MTJ-S	49
<i>Figure 3.4:</i> Niuafu'ou-Tonga boundary geology and tectonics	52
<i>Figure 3.5:</i> Magnetic profile modeling results	55
<i>Figure 3.6:</i> Geology of the Australia-Niuafu'ou boundary	59
<i>Figure 3.7:</i> Australia-Niuafu'ou magnetic interpretation	61
<i>Figure 3.8:</i> Australia-Niuafu'ou boundary tectonics	63

<i>Figure 3.9: New Lau Basin three-plate kinematic model</i>	70
<i>Figure 3.10: Regional map showing Euler pole locations</i>	72
<i>Figure 3.11: Lau Basin Brunhes kinematic model</i>	74
<i>Figure 4.1: Regional bathymetric map</i>	83
<i>Figure 4.2: Compiled bathymetric map of the southern Mariana Trough</i>	85
<i>Figure 4.3: Generalized map of southern Mariana Trough seafloor fabric</i>	87
<i>Figure 4.4: Detailed bathymetry maps showing type morphologies</i>	92
<i>Figure 4.5: Interpreted sonar imagery of study area and cross-sections</i>	94
<i>Figure 4.6: Mantle Bouguer anomaly and seismicity</i>	97
<i>Figure 4.7: Samples of fine-scale bathymetry with IMI-30 backscatter imagery</i>	100
<i>Figure 4.8: Hydrous lithosphere model</i>	108

LIST OF ABBREVIATIONS AND SYMBOLS

BASC	Backarc spreading center
MOR	Mid-ocean ridge
OSC	Overlapping spreading center
MORB	Mid-ocean ridge basalt
FRSC	Fonualei Rift and Spreading Center
MTJ(-S)	Mangatolu Triple Junction (southern branch)
NELSC	Northeast Lau Spreading Center
ELSC	Eastern Lau Spreading Center
VFR	Valu Fa Ridge
LETZ	Lau Extensional Transform Zone
CLSC	Central Lau Spreading Center
PR	Peggy Ridge
NWLSC	Northwest Lau Spreading Center
ILSC	Intermediate Lau Spreading Center
MGR	Malaguana-Gadao Ridge
SEMFR	Southeast Mariana Forearc Rifts
SWMR	Southwest Mariana Rift
DVZ	Diffuse volcanic zone
GSC	Galapagos Spreading Center
RR	Reykjanes Ridge
N-T	Niufo'ou-Tonga
A-T	Australian-Tonga
A-N	Australian-Niufo'ou
GMT	Generic Mapping Tools
GPS	Global positioning system
H ₂ O	Water
SiO ₂	Silicon dioxide
ZT01	<i>Zellmer and Taylor</i> [2001]
2-D	Two-dimensional
3-D	Three-dimensional
Ma, My	Million years ago, Million years
AVR	Axial volcanic ridge
CMT	Centroid moment tensor
GMT	Generic Mapping Tools

CHAPTER 1: INTRODUCTION

1.1 Overview

This dissertation investigates tectonic and magmatic processes associated with extension and crustal accretion in backarc basins. The three studies contained herein focus on features within the Lau Basin and Mariana Trough, but many of the interpretations and implications are broadly relevant to other subduction zones and backarc basins. The general approach can be considered “top-down,” where we use geologic and geophysical observations of tectonic and volcanic features on the seafloor to gain insight into plate-driven tectonic processes and basin kinematics, as well as deeper mantle-driven magmatic processes that shape these features and control the evolution of the basin. These observations are used to develop conceptual and kinematic models that reveal new insights into the structure of the mantle wedge, the interplay between plate-driven and mantle-driven processes, and how they control the mode and seafloor expression of backarc extension and crustal accretion. All three of the studies included herein as Chapters 2, 3, and 4 utilize a combination of new and previously collected geophysical data as the primary data sets for analysis and interpretation. Data sets include sonar data from multibeam, shallow-, and deep-towed systems, gravity data from ship-based gravimeters and derived from satellite altimetry, magnetic data collected with both a surface-towed magnetometer and an aeromagnetic survey, and seismicity data obtained from the Global Centroid Moment Tensor database and the International Seismological Centre reviewed event catalogue. The geologic and geophysical observations are also correlated with published geochemical analyses where available to gain further insight into magmatic processes.

1.2 Background

The concept of extension in a convergent margin may initially seem counterintuitive, but it is key to remember that subduction is driven by foundering of a negatively buoyant plate into the mantle [McKenzie, 1969] rather than two plates "crashing" into each other. As the subducting slab sinks, strong coupling at the plate interface due to the "trench suction" force [Elsasser, 1971; Forsyth and Uyeda, 1975] causes the slab to pull the overlying plate seaward, inducing trench-normal extensional stress. This causes the trench axis to "roll back" and migrate seaward as basin extension proceeds, in a process that is called trench or slab rollback [Dewey, 1980; Moberly, 1972]. Since the initial recognition of the extensional origin of backarc basins in the

1970's [e.g. *Elsasser*, 1971; *Karig*, 1970, 1971; *Moberly*, 1972] our understanding of tectonic and magmatic processes in subduction zones and backarc basins has steadily increased, and we now have a good general model for how these complex environments evolve over time. Prior to the initiation of extension, water derived from the subducting slab causes buoyant upwelling and flux melting in the overlying mantle wedge, building the chain of volcanoes known as the arc volcanic front [*Tatsumi*, 1986; *Tatsumi and Eggins*, 1995]. Extension always begins with a phase of rifting, initiating within ~50 km of the arc where the crust is thickest and the lithosphere is weakest [*Molnar and Atwater*, 1978; *Taylor and Karner*, 1983]. Rifting ultimately transitions into focused seafloor spreading along a narrow axis fundamentally similar to that at mid-ocean ridges (MORs) [e.g. *Hussong and Uyeda*, 1981]. At both backarc spreading centers (BASCs) and MORs, mantle upwelling and decompression melting is driven by plate divergence, and the rate of upwelling and melting varies primarily with spreading rate [*Reid and Jackson*, 1981]. In the backarc setting, fluids released from the subducting slab are a complex mixture of water, dissolved minerals, and other gases, but water is the primary fluid component that affects mantle melting behavior [*Stolper and Newman*, 1994; *Kelley et al.*, 2006] and rheology [*Karato et al.*, 1986; *Hirth and Kohlstedt*, 1996, 2003]. Hydrous flux melting provides an additional source of melt that varies independently of spreading rate [*Stolper and Newman*, 1994; *Sinton and Fryer*, 1987], and instead varies primarily with proximity to the arc volcanic front, where it is at a maximum [*Hawkins and Melchior*, 1985; *Tatsumi and Eggins*, 1995; *Kelley et al.*, 2006]. Other plate-driven factors include changes in opening geometry and extensional stresses due to the non-rigid nature of trench rollback or buoyant lithosphere impinging on the trench, complicating basin evolution over time. Other mantle-driven factors related to water beyond hydrous flux melting include changes in the rheology of the mantle wedge and the lithosphere. The addition of water reduces the viscosity of the mantle wedge [*Billen and Gurnis*, 2001; *Hirth and Kohlstedt*, 1996, 2003], which may facilitate more vigorous convection and allow for relatively sharp boundaries between domains of more and less hydrous mantle [*Dunn and Martinez*, 2011; *Sleeper and Martinez*, 2014]. The continuous flux of water near the arc volcanic front may also act to counter mantle dehydration during melting, creating weak hydrous lithosphere [*Martinez et al.*, 2012] that may allow for broad plate boundary zones. (This concept is explored in Chapter 4.) Thus, the characteristics of backarc basin extensional systems are controlled by the interplay

between plate-driven and mantle-driven processes, a theme that connects all three of the studies herein.

The variable effects of mantle-driven and plate-driven processes are expressed in the geologic, geophysical, and geochemical characteristics of backarc spreading centers (BASCs). Systematic trends in morphology, axial depth, and lava composition have been identified in the Mariana [Martinez *et al.*, 2000], east Scotia [Leat *et al.*, 2000], Manus [Sinton *et al.*, 2003], and Lau backarc basins, associated with varying proximity to the arc volcanic front, indicating a predominant mantle wedge control on melting over spreading rate within a certain distance of the arc [Pearce *et al.*, 1995; Taylor and Martinez, 2002]. One of the best-studied and clearest examples of these effects is the Eastern Lau Spreading Center (ELSC) and its southern extension, Valu Fa Ridge (VFR), in the Lau Basin. The Lau Basin is associated with the Tonga subduction zone in the southwest Pacific, where the Pacific and Australian plates are in convergence. The Lau Basin accommodates opening between the Australian Plate in the western half of the basin and the Tonga Plate, which includes the forearc and active Tofua arc volcanic front, along with the backarc crust in the eastern half of the basin. In the central Lau Basin, a third smaller plate, the Niuafu'ou microplate [Zellmer and Taylor, 2001], is caught between the Australian and Tonga plates, with extension partitioned between the eastern and western boundaries. The ELSC and VFR form the boundary between the Australian and Tonga plates in the southern half of the basin. Segments within ~70 km of the Tofua arc volcanic front show systematic along-axis trends in axial morphology, depth, and faulting [Martinez *et al.*, 2006; Sleeper and Martinez, 2014] crustal structure and thickness [Harding *et al.*, 2000; Martinez and Taylor, 2003; Jacobs *et al.*, 2007], and composition of axial lavas [Jenner *et al.*, 1987; Vallier *et al.*, 1991; Pearce *et al.*, 1995; Escrig *et al.*, 2009] with arc proximity. The arc-proximal segments are defined by a shallow volcanic ridge [Wiedicke and Collier, 1993], thick crust, and lava compositions with strong affinities to typical island arc lavas [Martinez and Taylor, 2003]. As distance to the arc increases the axis deepens, faults increase in abundance and throw, the crust thins, and geochemical indicators of subduction influence in axial lavas decrease [Escrig *et al.*, 2009]. These changes are analogous to those observed at MORs as spreading rate decreases, but in the case of the ELSC/VFR spreading rates actually increase from 47 to 103 mm/yr northward [Sleeper and Martinez, 2016] as the axis becomes deeper and less magmatic. This indicates that the dominant control on ridge characteristics along arc-proximal segments is mantle-driven

hydrous flux melting and buoyant upwelling. *Sleeper and Martinez* [2014] showed that the variations with arc proximity are not a simple linear decrease in subduction influence as the axis migrates away from the arc; rather, superimposed on this linear trend are distinct peaks in both axial topography and geochemical indicators of subduction influence [*Escrig et al.*, 2009] associated with the projected locations of the adjacent arc volcanoes along slab flow lines. Correlations between the axis and arc volcanoes along slab flow lines are interpreted to result from "fingers" of more hydrous mantle (rather than hotter mantle [*Tamura et al.*, 2002]) extending down the slab from the arc to the axis [*Sleeper and Martinez*, 2014] separated by zones of less hydrous mantle, all within a hydrous, low viscosity mantle wedge. Along the arc-

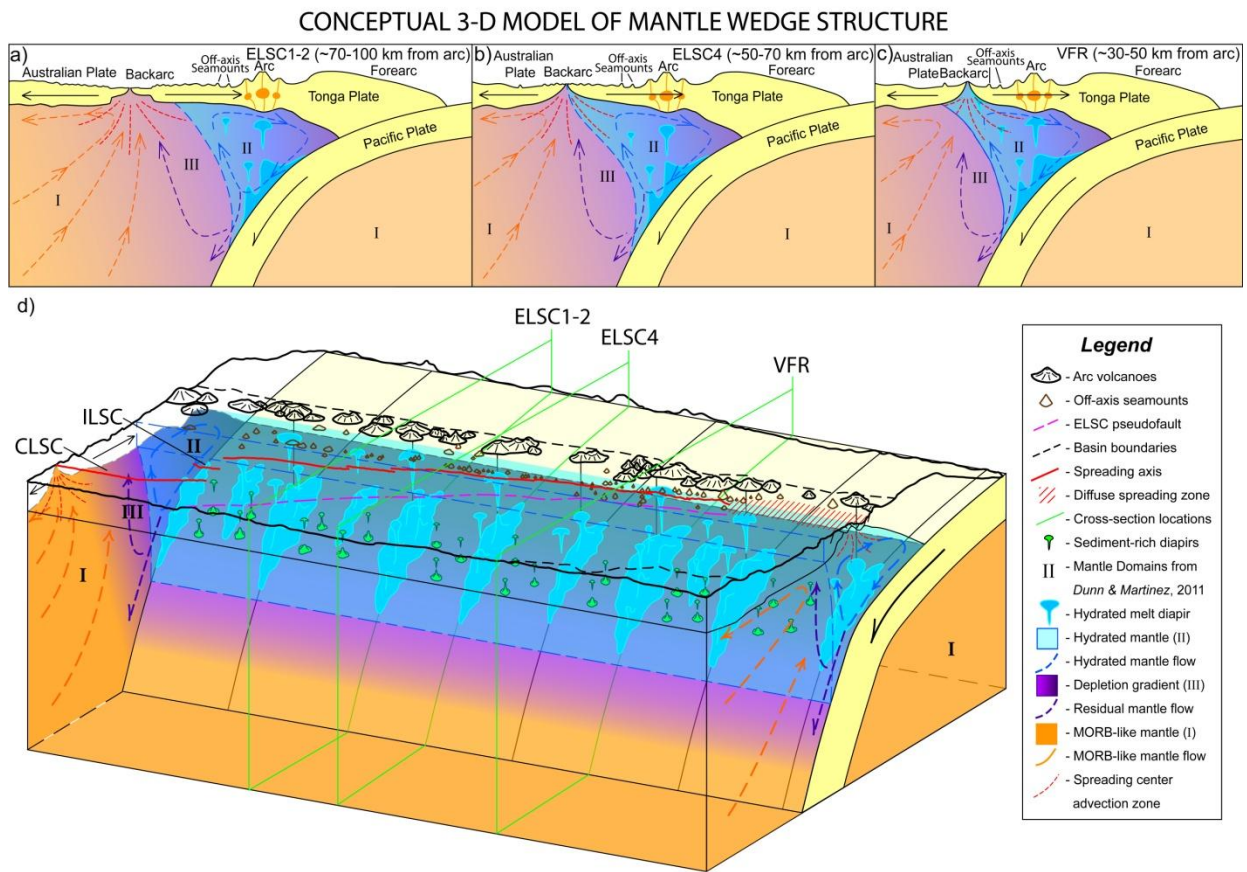


Figure 1.1: Conceptual 3-D model of mantle wedge structure. a), b), and c) are interpretive cross-sections through the northern ELSC, southern ELSC, and VFR, respectively, while d) is a conceptual 3D depiction of the entire ELSC and VFR, including part of the CLSC and Intermediate Lau Spreading Center (ILSC). Cross-sections are cut through hypothesized "hydrous fingers," represented by blue irregular bodies on the slab in all images. Key concepts: 1) Distinct concentrations ("fingers") of hydrous buoyant mantle extending from the arc to the backarc spreading center; 2) Mantle domains from *Dunn and Martinez* [2011]: I: Normal MORB-like mantle (orange), II: Hydrated mantle (light blue), III: Depleted, buoyant mantle (purple); 3) Sediment-rich diapirs feeding off-axis seamounts; 4) Schematic changes in crustal thickness and ridge morphology (in cross-sections).

distal segments more than ~70 km from the arc, the gradual trends with arc proximity are replaced by abrupt changes observed across a ~5 km offset between two segments along the central ELSC. Axial morphology changes from an axial high to a flat axis within a deep fault-bounded valley [Martinez *et al.*, 2006; Sleeper and Martinez, 2014], crustal thickness decreases abruptly by ~1.9 km [Dunn and Martinez, 2011], and geochemical indicators of subduction input in the axial lavas decrease sharply [Escrig *et al.*, 2009]. Martinez and Taylor [2006] attributed this abrupt decrease in magmatism to advection of buoyant mantle that has been depleted in melt-compatible elements by previous melting and then re-circulated through corner flow in the mantle wedge to arc-distal portions of the spreading center. Sleeper and Martinez [2014] interpreted this as representing a sharp boundary in the mantle between distinctly less hydrous depleted mantle and a depleted but more hydrous mantle wedge. At greater distances from the arc (~150-200 km in the case of the Lau Basin) the Central Lau Spreading Center (CLSC) is completely separated from the hydrous mantle wedge and plate-driven upwelling and decompression melting dominate, causing the CLSC to resemble MORs at similar spreading rates. Sleeper and Martinez [2014] combined all of these observations to develop a conceptual 3-D model of the structure of the mantle wedge under the southern Lau Basin (*Figure 1.1*).

1.3 Dissertation Structure and Chapter Summaries

Chapter 2 examines the Fonualei Rift and Spreading Center (FRSC) in the northeast Lau Basin, and its northern extension, the southern branch of the Mangatolu Triple Junction (MTJ-S) (*Fig. 1.2*). It displays similar trends in morphology and lava composition [Keller *et al.*, 2008; Escrig *et al.*, 2012] to those observed along the ELSC/VFR and other BASCs, including analogous changes at ~70+ km away from the arc, indicating that a similar mantle wedge structure underlies both systems. However, the southern and most arc-proximal segments of the FRSC abruptly change from a shallow volcanic ridge similar to VFR to isolated volcanic cones surrounded by anomalously deep seafloor, analogous to the change in morphology observed at ultraslow spreading MORs (~12 mm/yr) [Dick *et al.*, 2003]. The new kinematic model for the Lau Basin, which is the focus of Chapter 3, predicts spreading rates within the ultraslow range for these segments, varying from ~14 to 8 mm/yr southward [Sleeper and Martinez, 2016], terminating in a zone of active rifting south of which opening rates ultimately decrease to zero. Thus, the southern FRSC provides an opportunity to observe the effects on backarc crustal

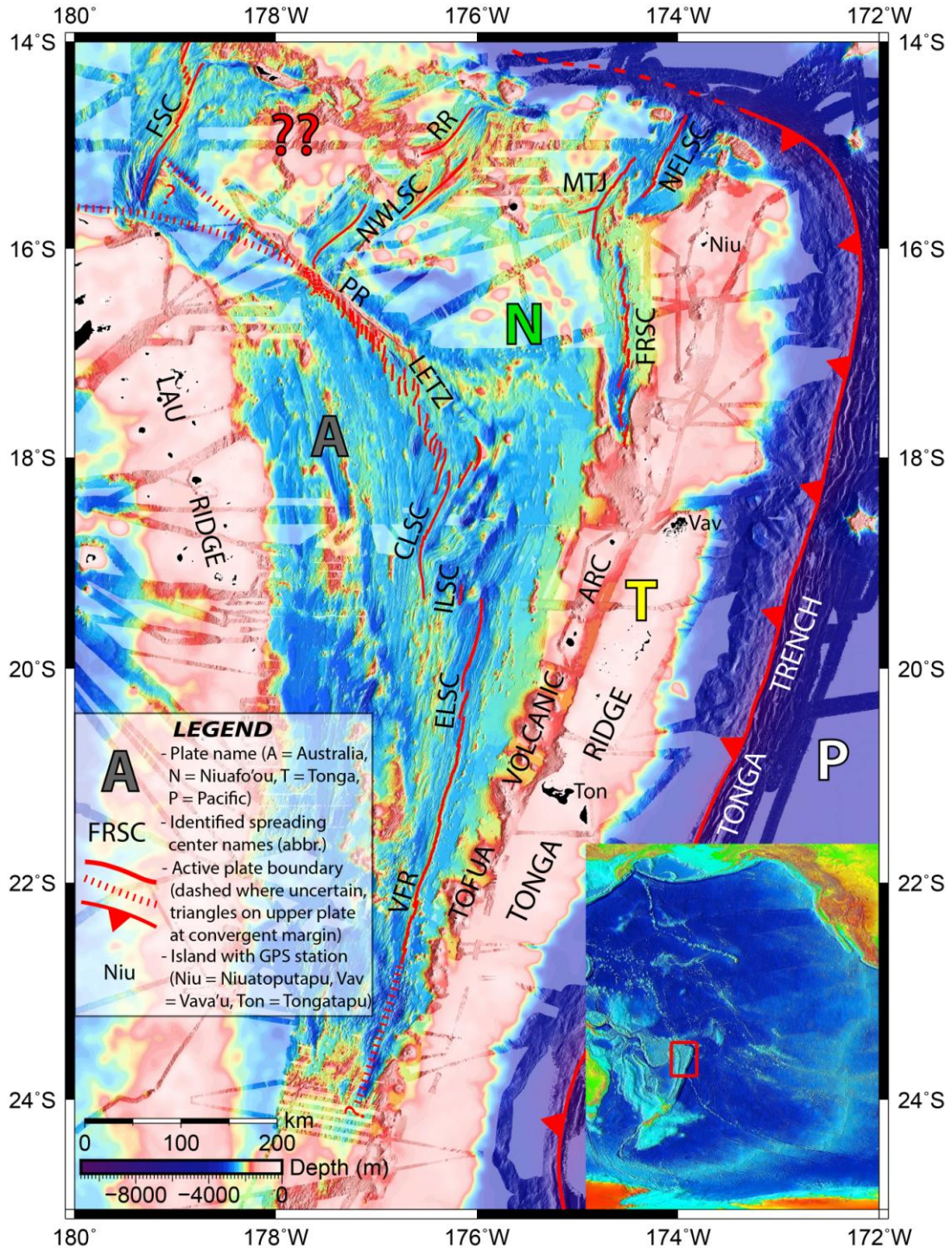


Figure 1.2: Lau Basin bathymetry and location map. Compiled multibeam bathymetry data (0.001° cell size) overlaid on predicted bathymetry from satellite altimeter measurements (reduced opacity) [Smith and Sandwell, 1997]. Bottom right inset shows location in SW Pacific, see legend for other symbols. Abbreviations: FSC = Futuna Spreading Center, NWLSC = Northwest Lau Spreading Center, RR = Rochambeau Rifts, NELSC = Northeast Lau Spreading Center, MTJ = Mangatolu Triple Junction, FRSC = Fonualei Rift and Spreading Center, PR = Peggy Ridge, LETZ = Lau Extensional Transform Zone, CLSC = Central Lau Spreading Center, ILSC = Intermediate Lau Spreading Center, ELSC = Eastern Lau Spreading Center, VFR = Valu Fa Ridge.

accretion as plate-driven upwelling and melting is minimized and mantle-driven buoyant upwelling and hydrous melting is maximized. The zero plate-driven component (i.e., no extension) end-member is the arc volcanic front, while the zero mantle-driven component end-member is a typical MOR or BASC greater than ~150 km from the arc.

The slow to ultraslow spreading rates (~32-8 mm/yr) predicted for the FRSC/MTJ-S are derived from a revised three-plate kinematic model of the Lau Basin (see map in *Fig. 1.2*), which is the focus of Chapter 3. The previous model by *Zellmer and Taylor* [2001] predicted much faster rates of ~94-47 mm/yr along the FRSC/MTJ-S, and thus a compensating increase in opening rates is required along the adjacent plate boundary to match total geodetically-determined opening rates between the Australian and Tonga plates [*Bevis et al.*, 1995; *Phillips*, 2003]. This necessitated a re-evaluation of the kinematics of the entire basin, and in the process we were able to resolve some additional discrepancies in the previous model. The study focuses on new interpretations of seafloor morphology, seismicity, and magnetization along the Niuafou'ou-Tonga plate boundary (the FRSC/MTJ-S) in the northeast basin and the Australian-Niuafou'ou plate boundary to the west. The results indicate a more complex and dynamic history of Lau Basin opening than previously described, including increasing basin opening rates over time, rapid evolution and re-organization of plate boundaries, and departures from standard rigid plate tectonics and Eulerian rotations used to describe global plate motions. These complexities and departures from rigid plate tectonics are driven by the inherently non-rigid nature of the plate-driven opening mechanism, trench rollback, along with the opening geometry, which is akin to a zipper opening from north to south as the subducting Louisville Seamount Chain on the Pacific plate sweeps southward along the Tonga trench [*Ruellan et al.*, 2003]. The dynamic, rapidly evolving nature of Lau Basin opening and non-rigid behavior suggest that kinematic models assuming rigid plate behavior may only be valid over time periods of hundreds of thousands of years or less.

Chapter 4 moves outside of the Lau Basin to the Mariana Trough (*Fig. 1.3*), another active backarc basin along the Izu-Bonin-Mariana convergent margin in the Western Pacific. Along the Mariana Trench, the Pacific plate is subducting in a NW direction under the Philippine Sea Plate. The trench is "pinned" at the northern and southern extremities of the Mariana Trough by the Cretaceous-age Ogasawara Plateau and the younger (<20 Ma) Caroline Ridge,

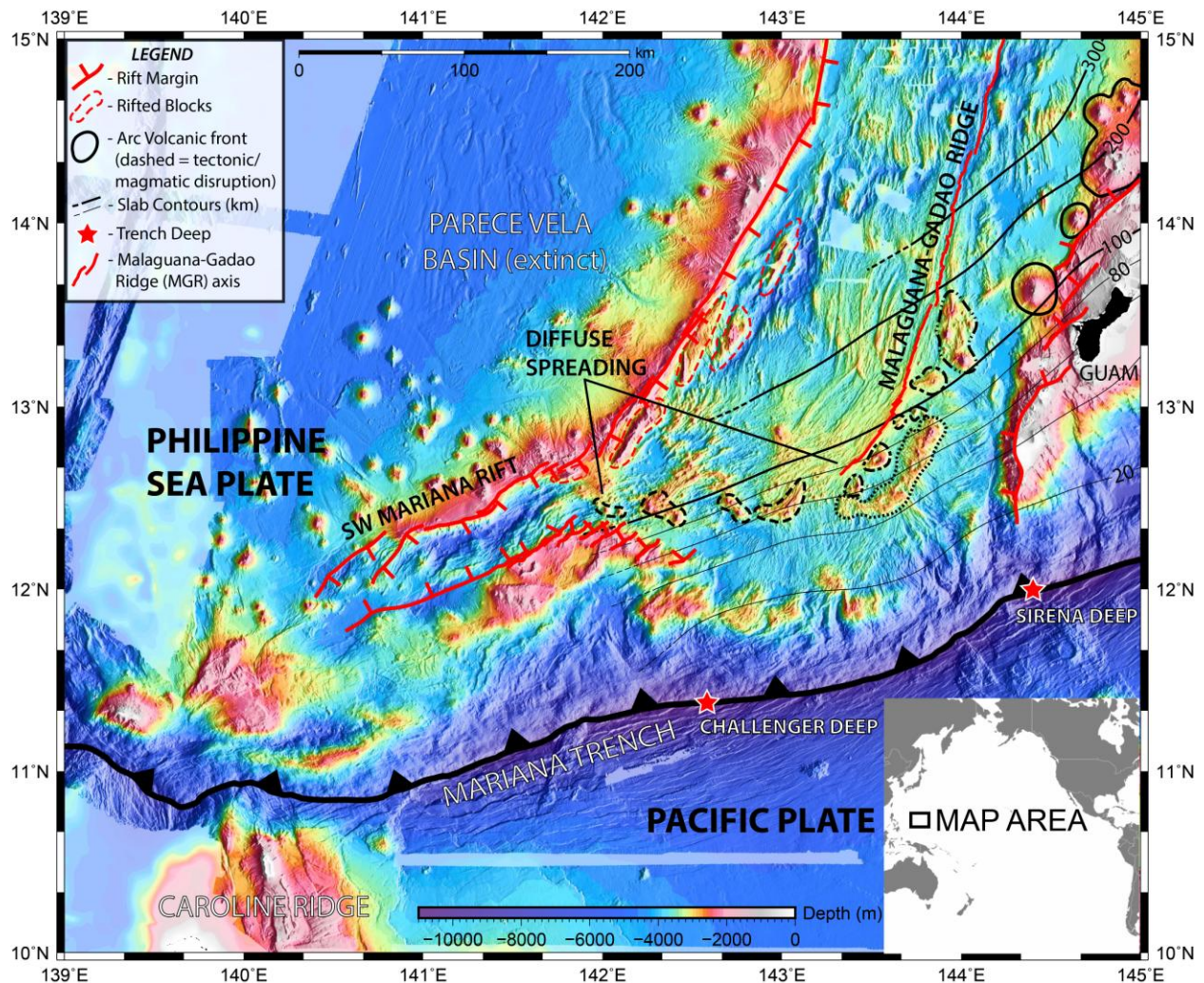


Figure 1.3: Compiled bathymetric map (0.001° cell size) of the southern Mariana Trough showing the relevant tectonic and volcanic features, see legend for symbols. Gaps in multibeam coverage are filled with predicted bathymetry from satellite altimeter measurements (reduced opacity) [Smith and Sandwell, 1997]. Slab contours are from the Slab 1.0 model [Hayes et al., 2012].

respectively, volcanic chains with relatively thick crust and buoyant lithosphere that resists subduction [Hsui and Yongquist, 1985]. This has given rise to a bow-shaped basin such that the Mariana Trench curves from ~N-S along the central portion of the basin to nearly E-W at the southern end. Chapter 4 describes a new mode of magmatic seafloor spreading observed in the southern Mariana Trough between the southern terminus of the Malaguana-Gadao Ridge (MGR) spreading center and the Southwest Mariana Rift (SWMR) to the west (Fig. 1.3). The MGR is an example of an arc-proximal BASC similar to VFR in the Lau Basin, where the axis captures some of the hydrous melt from the nearby arc volcanic front, causing abundant magmatism despite relatively slow spreading rates of ~40-50 mm/yr [Kato et al., 2003]. The shallow

volcanic ridge defining the MGR axis abruptly terminates and is replaced by a broad ~20-50 km wide zone of active volcanism and tectonism characterized by short volcanic ridges, volcanic cones, and deeps unlike the fabric on the MGR flanks or within the SWMR. This zone extends ~120 km west from the MGR tip to the deep graben associated with active arc rifting in the SWMR, and the entire zone overlies slab depths typically associated with the arc volcanic front. This fabric is interpreted to be the result of "diffuse spreading," where volcanism and crustal accretion occur over a broad area rather than along a narrow axis as is typical at both MORs and BASCs. At MORs, the small amount of water in the mantle is extracted into the melt, dehydrating the residual material and causing a sharp increase in strength and viscosity [Karato, 1986; Hirth and Kohlstedt, 1996]. This is thought to aid in focusing melt generated over a broad ~200 km wide zone in the mantle toward a narrow spreading axis [Phipps Morgan, 1997], that can vary from ~1-2 km at fast spreading MORs to ~15-20 km at slow spreading MORs. Diffuse spreading is facilitated by the constant flux of water into the mantle wedge from the subducting slab near the arc, which opposes lithospheric dehydration and strengthening, creating a broad zone of weak "hydrous lithosphere" where new crust is accreted in a disorganized manner over a broad area rather than focused along a narrow axis. This new form of crustal accretion is not simply a transitional stage between rifting and typical organized seafloor spreading, but rather if the balance between plate-driven upwelling, melting, and dehydration and water flux from the underlying slab remains within some threshold, it should continue indefinitely as diffuse spreading.

CHAPTER 2: THE FONUALEI RIFT AND SPREADING CENTER: EFFECTS OF ULTRASLOW SPREADING AND ARC PROXIMITY ON BACKARC CRUSTAL ACCRETION

Publication reference: Sleeper, J. D., F. Martinez, and R. Arculus (2016) The Fonualei Rift and Spreading Center: effects of ultraslow spreading and arc proximity on backarc crustal accretion, *J. Geophys. Res.*, 121, doi:10.1002/2016JB013050.

Abstract

Backarc spreading center characteristics reflect interactions between plate-driven mantle advection and melting and slab-driven hydrous melting and buoyant upwelling in the mantle wedge. At the Fonualei Rift and Spreading Center (FRSC) in the Lau Basin spreading rates decrease from slow to ultraslow, providing an opportunity to examine crustal accretion as the plate-driven component is minimized. A new Lau Basin kinematic analysis predicts FRSC spreading rates of ~32-8 mm/yr southward, much slower than previous estimates of ~95-47 mm/yr. Here we examine FRSC morphology and geophysical characteristics as it approaches the Tofua arc volcanic front southward and spreading rates decrease, minimizing the plate-driven component of mantle advection and maximizing buoyant hydrous flux melting. Axial morphology changes abruptly from a deep, flat, faulted axis ~100 km away from the arc to a volcanic ridge that shoals and increases in relief southward. Within ~50 km of the arc at the south end, the volcanic ridge is abruptly replaced by isolated volcanic cones bisected by volcanic rift zones and surrounded by anomalously deep seafloor. These morphologic changes likely reflect along-axis focusing of mantle upwelling and melting similar to that seen at ultraslow mid-ocean ridges, causing the change in morphology from a segmented ridge to spaced axial cones. We propose that as opening rates slow and the ridge approaches the arc, more of the inherently three-dimensional pattern of hydrous flux melting and buoyant upwelling in the mantle wedge is expressed volcanically. With faster opening, two-dimensional plate-driven mantle advection dominates melt production, favoring ridges over point-source features.

2.1. Introduction

Backarc spreading centers (BASCs) in close proximity to the arc volcanic front represent our best natural laboratories for studying the modes of melting of the underlying mantle wedge. For example, subduction-related sources of melting [Pearce *et al.*, 1994] can variably interact with partial melting driven by plate-driven mantle upwelling, as at mid-ocean ridges (MORs) [Langmuir *et al.*, 1992]. Melt erupted along the arc volcanic front is largely derived from hydrous flux melting of the underlying mantle wedge [Tatsumi and Eggins, 1995], due to the addition of slab-derived water. It is also recognized that subduction-related effects extend into the backarc basin [e.g. Fryer and Hussong, 1982; Jenner *et al.*, 1987, Sinton and Fryer, 1987], and that this influence varies with arc proximity [Pearce *et al.*, 1994; Martinez and Taylor, 2002; Taylor and Martinez, 2003]. Since water lowers the mantle solidus and proportionately increases melt production [Stolper and Newman, 1994], spreading axes become shallower and more magmatically robust with arc proximity than expected based on spreading rate alone [Martinez and Taylor, 2002; Taylor and Martinez, 2003]. Studies in the Lau Basin have shown strong evidence for a sharp boundary at the arc-distal edge of a hypothesized zone of hydrous mantle in the shallow part of the mantle wedge, associated with abrupt geochemical [Escrig *et al.*, 2009], geophysical [Dunn and Martinez, 2011], and morphologic [Sleeper and Martinez, 2014] changes expressed in BASC characteristics. Other studies have documented geochemical [Escrig *et al.*, 2009, 2012], geophysical [Tamura *et al.*, 2002; Hasegawa and Nakajima, 2004], and morphologic [Tamura *et al.*, 2002; Wysoczanski *et al.*, 2010; Sleeper and Martinez, 2014] evidence that within this hydrous mantle wedge corner are "fingers" of more hydrous (or hotter [Tamura *et al.*, 2002]) material extending from the arc volcanoes to the backarc. These observations suggest that many subduction zones share a similar mantle wedge structure in terms of how melt and various mantle components are distributed. One question that has not been examined in detail is how the plate-driven component (i.e., spreading rate) affects the surficial volcanic expression of these slab-derived components in the mantle wedge.

The Fonualei Rift and Spreading Center (FRSC), located in the northeast Lau Basin, is a favorable location to examine how spreading rate affects the volcanic and tectonic expression of mantle wedge structure. New two-dimensional (2-D) modeling of magnetic profiles and a revised Lau Basin kinematic model [Sleeper and Martinez, 2016] indicate that the FRSC may be

spreading much slower than estimated rates of ~94-47 mm/yr [Zellmer and Taylor, 2001]. Rates estimated on two aeromagnetic profiles near the northern end of the FRSC are 23.6 and 25.5 mm/yr, decreasing to zero southward as the rifted margins converge and seismic and morphologic evidence of rifting disappear by ~18°30'S [Sleeper and Martinez, 2016]. At MORs, slow spreading promotes the expression of buoyancy-driven three-dimensional (3-D) upwelling where volcanism is concentrated at segment centers [Kuo and Forsyth, 1988; Parmentier and Phipps Morgan, 1990]. With faster spreading a plate-driven 2-D mantle upwelling configuration increasingly dominates over buoyant upwelling, resulting in more continuous volcanic ridge segments [Reid and Jackson, 1981; Parmentier and Phipps Morgan, 1990]. Axial morphology variations southward along the FRSC are consistent with decreasing spreading rates, showing an abrupt transition from a volcanic ridge to spaced volcanic cones as predicted in numerical and analog models of the transition from plate-driven to buoyant mantle upwelling at MORs [Kincaid et al., 1986]. These morphologic variations mirror observed MOR spreading rate variations from fast to ultraslow [Dick et al., 2003; Michael et al., 2003], suggesting similar effects on crustal accretion and melt focusing processes in both the MOR and backarc environments. However, unlike at ultraslow MORs no mantle exposures are known from the FRSC, suggesting that even at ultraslow rates arc-proximal BASCs are more magmatic than MORs [Keller et al., 2008; Escrig et al., 2012]. Further, a more hydrous mantle beneath BASCs than at MORs implies lower mantle viscosity [Hirth and Kohlstedt, 2003] and a greater proportion of melting above the wet solidus, which may favor buoyant upwelling [Choblet and Parmentier, 2001].

Previous expeditions along the FRSC and in the northeast Lau Basin have focused primarily on lava geochemistry and hydrothermal activity [e.g. German et al., 2006; Keller et al., 2008; Escrig et al., 2012; Resing et al., 2012]. The kinematics and tectonics of the entire Lau Basin have been described by Zellmer and Taylor [2001] and a more recent seismicity study by Conder and Weins [2011]. Sleeper and Martinez [2016] presents an updated three-plate kinematic model that resolves some of the geologic discrepancies in previous models. This paper focuses on the morphology and tectonics of the FRSC and MTJ-S, which together comprise the Niufo'ou-Tonga plate boundary. Here we use compiled multibeam and other geophysical data to describe axial morphology, map tectonic and volcanic features, and define axial segmentation along the FRSC. These maps and descriptions, in light of geochemical studies, are used to

develop a general conceptual model of mantle wedge structure that can be compared to other BASCs, and gain insight into how spreading rate modulates volcanic and tectonic processes in the backarc environment.

2.2. Geologic Setting and Background

2.2.1 Northeast Lau Basin

The Lau backarc basin began opening ~6 Ma [Hawkins, 1994] due to eastward rollback along the Tonga subduction zone. Basin opening initiated in the forearc and propagated southward [Hawkins, 1994], separating the remnant arc of the Lau Ridge from the Tonga Ridge forearc, and giving the Lau Basin a distinct V-shape. *Figure 2.1* shows a schematic map of the major tectonic features of the Lau Basin. The northeastern Lau Basin, in which the study area is located, is characterized by particularly complex tectonics (*Fig. 2.2*). Phillips [2003] has revised Lau Basin geodetic rates originally published in Bevis *et al.* [1995] and we use the revised rates here. Near the northern end of the trench, the Pacific plate is subducting westward under the Tonga plate at ~247 mm/yr [Phillips, 2003], the fastest known convergence rate on Earth. At the northeast corner, there is a tear in the Pacific plate [Millen and Hamburger, 1998] and along the northern margin the boundary becomes a transform fault with a component of northward extension [Bevis *et al.*, 1995]. North of ~18°30'S, the broad forearc massif of the Tonga Ridge abruptly terminates, replaced by a more irregular and deeper forearc region. The Tofua arc volcanic front, which has a consistent linear orientation along most of its length, has an abrupt ~25 km left-stepping offset at ~16°20'S, and the arc toward the north is rotated ~5° counter-clockwise relative to the southern portion (*Fig. 2.2*).

2.2.2. The Fonualei Rift and Spreading Center

The FRSC and the southern branch of the MTJ (MTJ-S) are located within the complex northeast corner of the Lau Basin (black box in *Fig. 2.2*), extending ~257 km from ~174°33'W/15°37'S to 174°49'W/17°54'S in a roughly N-S orientation, accommodating ~E-W extension between the Niufo'ou microplate and the Tonga plate [Zellmer and Taylor, 2001; Sleeper and Martinez, 2016]. North of the triple junction, the northern branch of MTJ and the

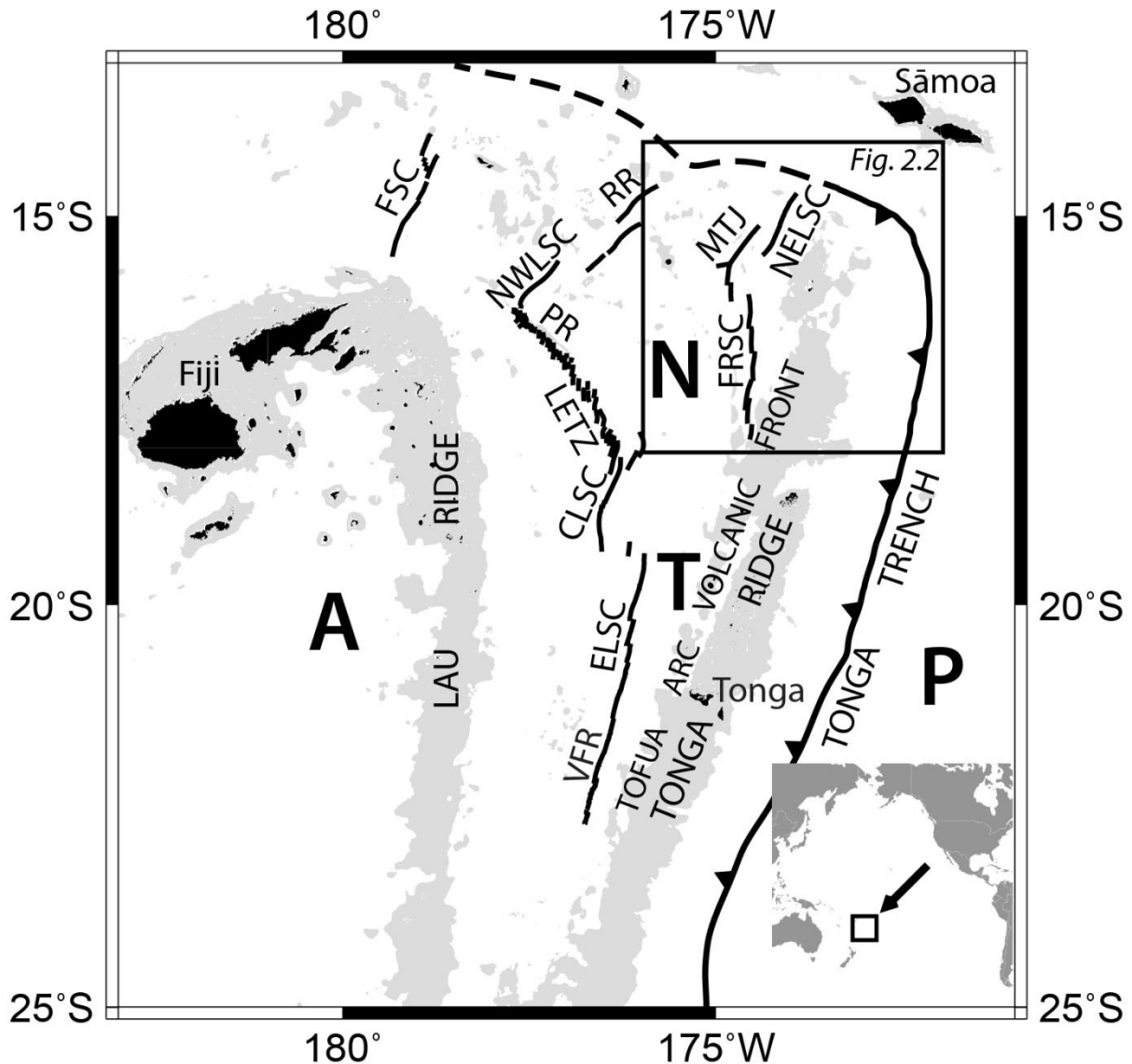


Figure 2.1: Lau Basin location map. Gray regions highlight topography above the 1800 m bathymetric contour. Bottom right inset shows location in SW Pacific, black box shows the limits of Fig. 2.2, and identified spreading centers are marked with thick black lines. Abbreviations: A = Australian plate, P = Pacific plate, N = Niufo'ou plate, T = Tonga plate, FSC = Futuna Spreading Center, NWLSC = Northwest Lau Spreading Center, RR = Rochambeau Rifts, NELSC = Northeast Lau Spreading Center, MTJ = Mangatolu Triple Junction, FRSC = Fonualei Rift and Spreading Center, PR = Peggy Ridge, LETZ = Lau Extensional Transform Zone, CLSC = Central Lau Spreading Center, ELSC = Eastern Lau Spreading Center, VFR = Valu Fa Ridge.

NELSC trend in a northeast direction (~N25E-N30E) whereas a short rift trends westward, implying that extension along these systems is responding to a different stress regime than the FRSC/MTJ-S, possibly due to the existence of a different microplate to the NW of the triple junction [Conder and Wiens, 2011]. The FRSC rift margins are incompletely mapped toward the north, but rifting appears to have begun immediately west of the volcanic front, propagating southward over time [Zellmer and Taylor, 2001] and migrating slightly eastward so that the

southern rift zone is within the volcanically thickened arc platform ~10-15 km west of the active arc. The southern end of the spreading axis terminates in a zone of active rifting based on prominent normal faulting teleseismicity and uplifted rift margins.

The spreading axis approaches the Tofua arc southward from over 100 km to the west along MTJ-S to ~25 km at the south end of the FRSC, as spreading rates decrease from ~32 mm/yr at the triple junction to ~8 mm/yr [Sleeper and Martinez, 2016]. The ridge shoals toward the south and morphology changes from an axial valley along MTJ to a volcanic ridge along the northern and central FRSC, and abruptly transitions to a series of spaced volcanic cones along the southern FRSC. The general trend of decreasing depth and increasingly magmatic axial morphologies matches observations from other BASCs, including the ELSC/VFR in the southern Lau Basin [Martinez *et al.*, 2006; Sleeper and Martinez, 2014], and southern Mariana trough [Martinez *et al.*, 2000]. The northern Mariana trough may be analogous to the southern FRSC, as it displays a similar morphologic transition in the region where the basin is transitioning from rifting to spreading and opening rates are <1 cm/yr [Martinez *et al.*, 1995; Yamazaki *et al.*, 2003]. The chemistry of lavas erupted along the FRSC have particularly strong affinities to the arc compared to those in other arc-proximal BASCs [Keller *et al.*, 2008; Escrig *et al.*, 2012], and Keller *et al.* [2008] suggested that the FRSC axis may be capturing the melt from adjacent arc volcanoes and causing them to become extinct. With the benefit of a larger sample set and new isotopic and trace element analyses Escrig *et al.* [2012] also identified systematic trends showing increasing subduction input with arc proximity, as well as spatial correlations with arc volcanoes suggesting a connection between arc and backarc melting regimes near the arc. Sparse sampling along the MTJ recovered backarc basin basalts with a significantly reduced subduction component compared to the FRSC [Keller *et al.*, 2008], indicating that backarc and arc melting regimes become disconnected with increasing separation.

2.3. Methodology

2.3.1. Geophysical Data Sets and Processing

We describe the geology, segmentation, and tectonics of the FRSC using compiled multibeam bathymetry and acoustic backscatter imagery, along with gravity data. Multibeam bathymetry data from multiple cruises in the area (*Fig. 2.3a*) (NoToVE (2004), KM0417 (2004),

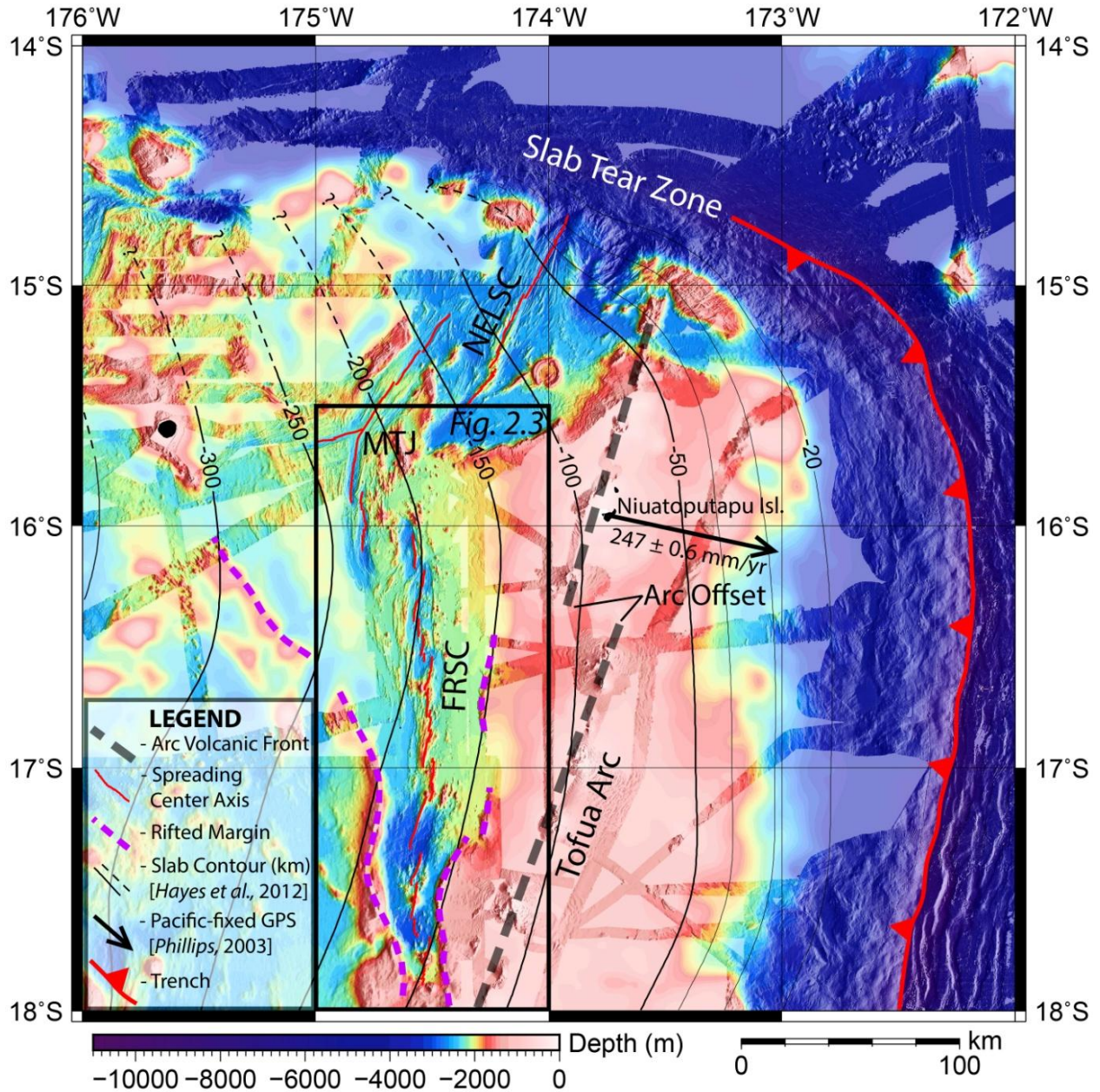


Figure 2.2: Compiled bathymetry map of the northeast Lau Basin showing the major tectonic features. Gaps in multibeam coverage filled with predicted bathymetry from satellite altimeter measurements (reduced opacity) [Smith and Sandwell, 1997]. Slab contours from Slab 1.0 model [Hayes et al., 2012]. Note offset in position of arc volcanic front and decreasing separation between the FRSC/MTJ-S axis (red lines) and the arc southward. Limits of Fig. 2.3 are outlined with a black box, other labeled features are shown in the legend. All bathymetry maps are shown as shaded relief images illuminated from the east (100° azimuth). Abbreviations are the same as Fig. 2.1.

KM0704 (2007), KM1007 (2010), KM1129A (2011), TN227 (2008), MW9603 (1996), RR0916 (2009)) were compiled, ping-edited, and gridded at .0003° (~30 m) cell size using MB-System [Caress and Chayes, 2006] and Generic Mapping Tools (GMT) [Wessel et al., 2013] software. Backscatter data were compiled from the KM1007, KM1129A, TN227, RR0916, and KM0417

cruises, and MB-System was used to correct for distortion due to grazing angle across the swaths. Due to the poor quality of some of the backscatter data, they were compiled by stacking the best quality data on top and correcting for systematic offsets between each data set. The systematic offsets were corrected by calculating the median of the difference in z-values between a pair of grids using GMT software and adding or subtracting that from one of the grids, then performing the same calculation with each new grid added to the compilation. Shipboard gravity data in the region is limited in coverage and quality, so Bouguer and mantle Bouguer gravity anomalies were calculated from satellite altimeter data [Sandwell *et al.*, 2014], also using GMT software (*Fig. 2.3b*).

2.3.2. FRSC Axial Segmentation

Our classification of axial segmentation generally follows the convention used at MORs [Macdonald *et al.*, 1991a], where first-order segments hundreds of km long are separated by transform faults, second-order segments are separated by non-transform overlapping spreading centers (OSCs) with widths of 2-30 km, third-order segments are separated by smaller OSC's with offsets of 0.5-2 km, and fourth-order segments are defined by small deviations in axial linearity (called "devals" [Langmuir *et al.*, 1986]) of ~ 1 km or less. Our classification system is also very similar to that from *Sleeper and Martinez* [2014] for the ELSC/VFR in the southern Lau Basin. Although the FRSC lacks transform faults that typically define the boundaries of first-order MOR segments [Macdonald *et al.*, 1991a], we define the combined length of the FRSC/MTJ-S here as a first-order segment, bounded to the north by the triple junction and to the south by the end of magmatic spreading within a zone of active rifting. The ~257 km long first-order segment can be divided into eight second-order segments ranging from ~16.4-51.5 km in length. Second-order discontinuities are defined by left-stepping non-transform offsets on the order of ~1-5 km, with the exception of the ~25 km offset between the north end of FRSC and the south end of MTJ-S. Third-order segments (~2.2-18.2 km in length) are bounded by smaller offsets (typically <2 km). Devals defining fourth-order segment boundaries are <1 km and can be right- or left-stepping. The segmentation pattern is complex, and in some cases the distinction between second- and third-order or third- and fourth-order discontinuities is ambiguous.

Here we define six second-order segments along FRSC and another two along MTJ-S (*Fig. 2.3a*), based on a combination of along-axis and off-axis morphology, segment length, and

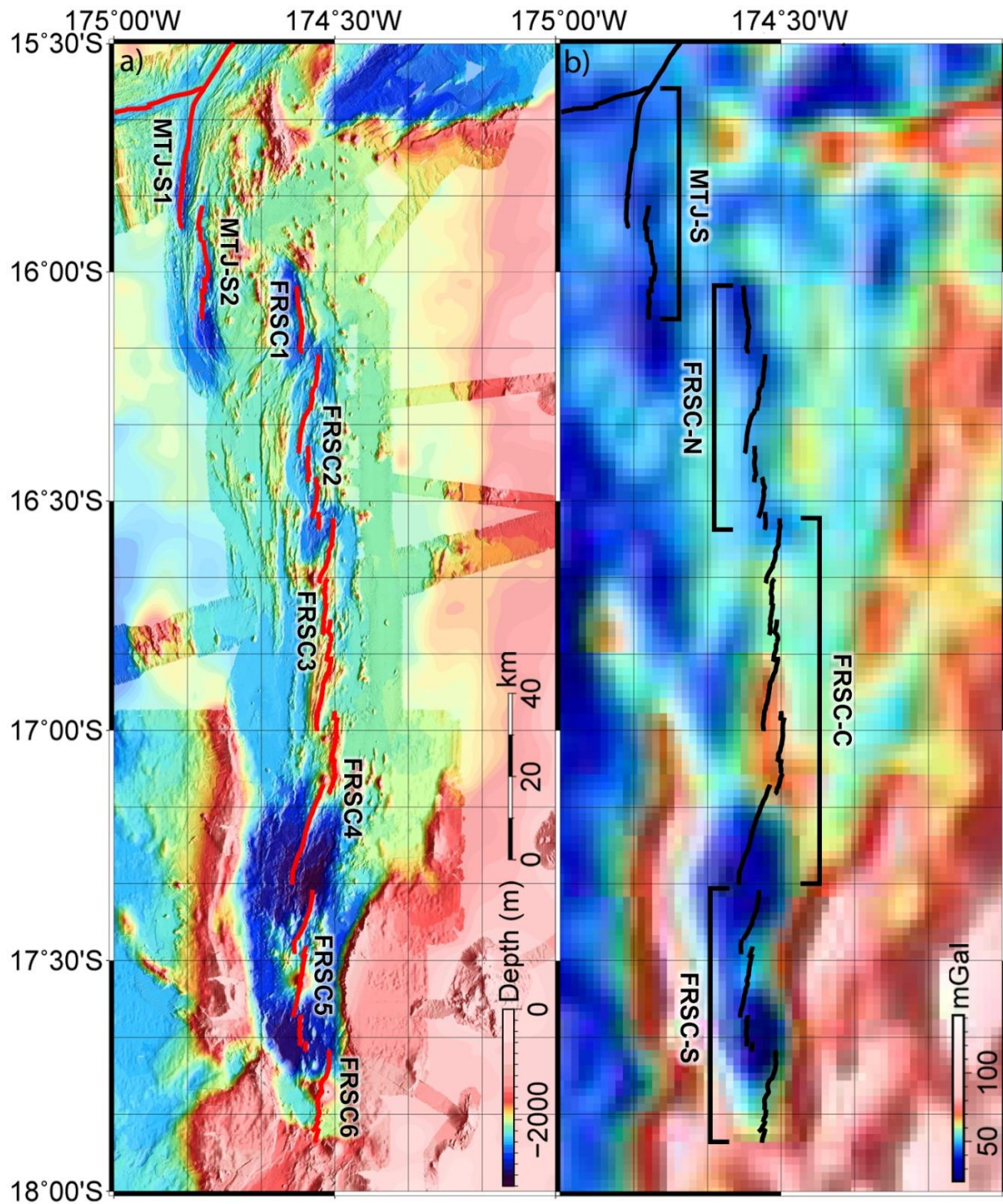


Figure 2.3: Geophysical data along the FRSC/MTJ-S. a) Compiled bathymetry map used for geologic maps and detail plots, gaps in multibeam coverage are filled with predicted bathymetry from satellite altimeter measurements (reduced opacity) [Smith and Sandwell, 1997]. Second-order segments are labeled. b) Free-air gravity anomaly based on satellite altimeter measurements [Sandwell et al., 2014], gridded at 1 arc-minute. Second-order segments are lumped into four groups based on similar morphology.

offset width between segment ends. To streamline the geologic descriptions and discussion, these eight segments are placed into four groups based on similar axial morphology: MTJ-S (MTJ-S1/S2), FRSC-N (FRSC1/2), FRSC-C (FRSC3/4), and FRSC-S (FRSC5/6) (*Fig. 2.3b*). Third-order segments were also defined, largely based on small offsets of <2 km along the ridge crest, but for the sake of clarity are not labeled on any of the figures. Fourth-order segments are not specifically defined because we cannot reliably distinguish the subtle bends that define segment boundaries in the bathymetry data. For statistics and more detailed information on segmentation see *Table 2.1*.

2.3.3. Gravity Data

Due to the sparse coverage of ship-based geophysical surveys, gravity anomalies derived from satellite altimetry measurements were used [*Sandwell et al., 2014*]. *Fig. 2.3b* shows the one arc-minute gridded free-air anomaly, which is dominated by topographic effects. In order to remove the effects of seafloor relief, satellite predicted bathymetry was used to fill the gaps in the compiled multibeam bathymetry grid, largely in ridge flank areas (*Fig. 2.2*). The combined data were re-sampled onto larger and coarser square grids with 1024x1024 cells (~300 m cell size) and used to calculate a Bouguer anomaly based on standard densities for water (1035 kg/m³) and basaltic crust (2700 kg/m³). A mantle Bouguer anomaly was also calculated assuming a uniform 7 km thick basaltic crust and a standard mantle density of 3300 kg/m³. All gravity anomalies were calculated using standard fast Fourier transform methods in GMT software [*Wessel et al., 2013*], with five terms in the Parker expansion [*Parker, 1973*]. Results are presented in 2.4.2.

2.4. Observations and Results

2.4.1. FRSC morphology: Segment-by-Segment Descriptions

We show below detailed bathymetry and acoustic backscatter maps that describe general characteristics of each of the main morphologic segments identified in *Fig. 2.3b*. The bathymetry maps are used to identify and describe volcanic and tectonic features at the second- and third-order segment scale in order to characterize morphologic variations that reflect and provide

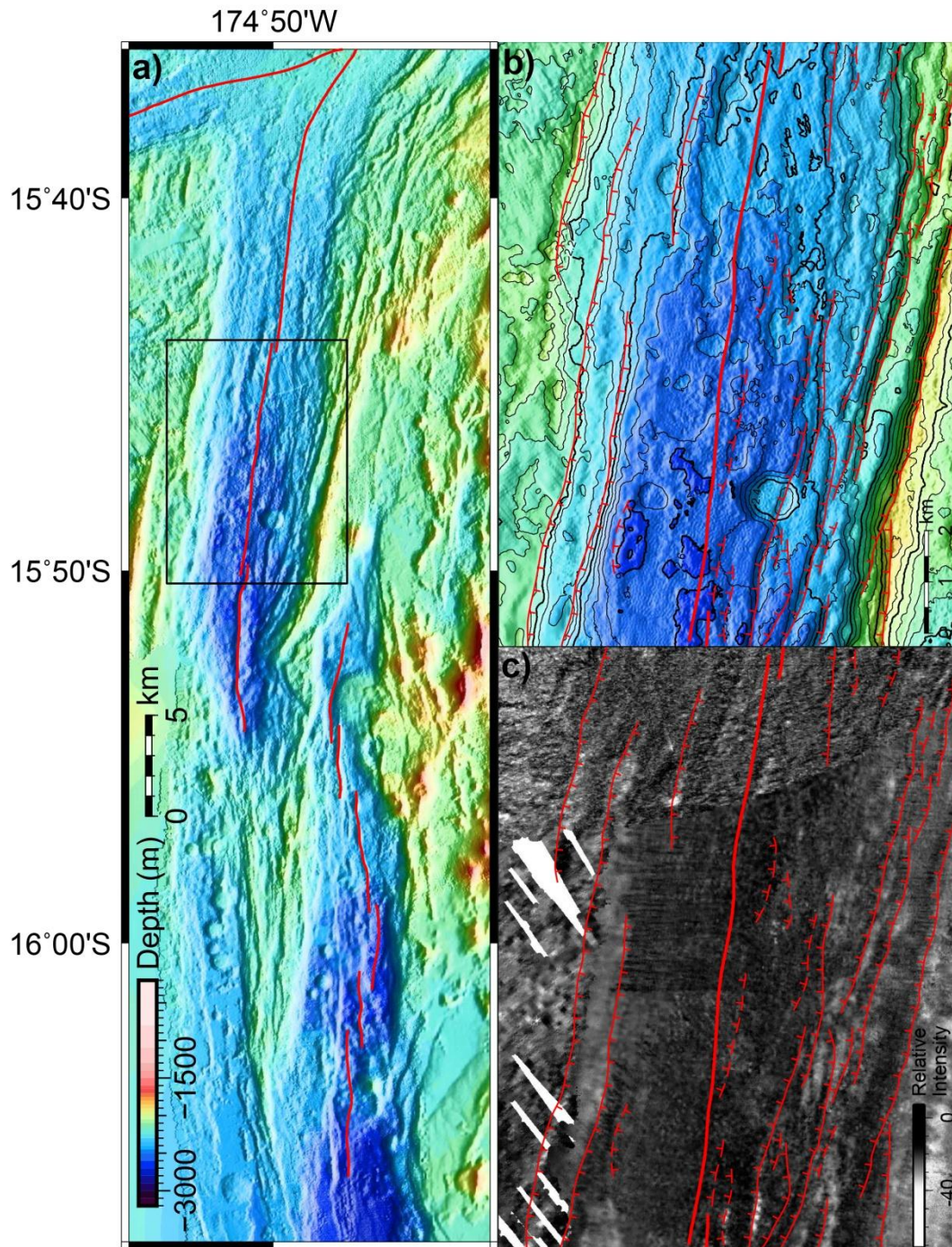


Figure 2.4: MTJ-S morphology. a) Compiled bathymetry (0.0003° cell size) map showing both MTJ-S1 and MTJ-S2. The axis has very little relief and lies within a deep valley bounded by large (100+ m throws) faults separating the deep axis from shallower seafloor on the flanks. Black box shows b) and c) location. b) Compiled bathymetry (0.0001° cell size, 50 m contour interval, labels in km) map of the MTJ-S1-2 third-order segment. The axis is poorly defined by a narrow, discontinuous graben within a deep fault-bounded axial valley. c) Compiled backscatter (0.0001° cell size) image. Noisy data and incomplete coverage show high backscatter within the axial valley and some fault scarps, but poor detail. Symbols for Figs. 2.4-2.7: Spreading axis: solid red lines; Faults: red lines, dashed where uncertain, ticks point down-dip; Mappable lava flow margins (most flow margins are not resolvable in the sonar data): solid purple line (Figs. 2.5,2.7); Volcanic cones: dashed magenta lines (Fig. 2.7).

insight into underlying mantle wedge processes and relationships with the nearby arc volcanic front. The backscatter data are of variable quality and are only adequate to differentiate between effusive (any type of surface lava flow or volcanic structure with high acoustic backscatter) and explosive volcanism (volcaniclastics characterized by relatively low backscatter intensity and a streaky texture from unconsolidated materials draping the ridge flanks), the latter of which is only observed along the southern half of the FRSC. Away from the axial flanks, we interpret regions of low backscatter intensity as pelagic sediment and volcaniclastic material from nearby arc volcanoes.

2.4.1.1. Arc-distal Segments: MTJ-S1 and MTJ-S2

The southern branch of Mangatolu Triple Junction (MTJ-S) is the northernmost portion of the spreading system (*Fig. 2.3*), located ~90-110 km west of the adjacent part of the arc, and spreading rates decrease southward from ~32-27 mm/yr [*Sleeper and Martinez, 2015*]. Axial morphology along both segments is characterized by a deep, flat axis within a fault-bounded valley (*Fig. 2.4a*). Individual third-order segments are defined by either very low-relief hummocky volcanic ridges or narrow grabens bounded by faults with throws on the order of a few tens of m at most (*Fig. 2.4b*). Larger faults with throws of ~100-250+ m lie 1 to 3 km away from the axis on either side, separating the deep seafloor near the axis from shallower seafloor with numerous prominent volcanic ridges, suggesting that this part of the spreading system may have been more magmatic in the past. The high acoustic backscatter within the neovolcanic zone (*Fig. 2.4c*) and morphology of the small volcanic structures (*Fig. 2.4b*) are consistent with effusive eruptions, and dredge samples from this segment recovered pillow basalts [*Falloon et al., 1992; Keller et al., 2008*].

2.4.1.2. Transitional Segments: FRSC1 and FRSC2

The FRSC1 segment lies across a ~25 km left-stepping non-transform offset with MTJ-S (*Fig. 2.3*). Axial morphology of both FRSC1 and FRSC2 is characterized by a rounded volcanic ridge with ~300-600 m of relief (*Fig. 2.5a,b*), compared to at most 100 m of relief along MTJ-S. These segments are located ~75-100 km from the main extension of the Tofua arc toward the south, but only ~50-75 km from the adjacent northern offset portion, and spreading rates decrease southward from ~27-23 mm/yr [*Sleeper and Martinez, 2015*]. The axial volcanic ridge

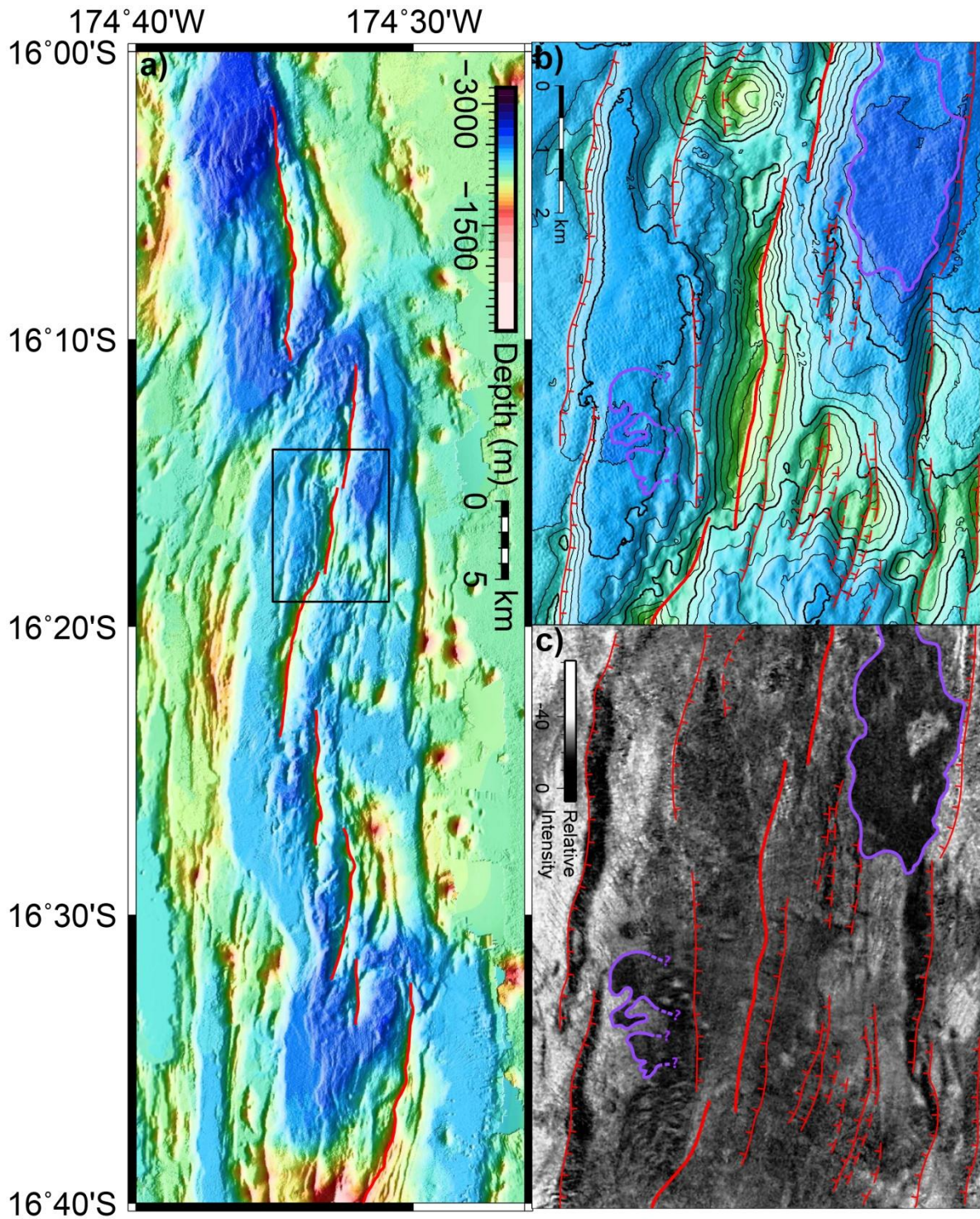


Figure 2.5: FRSC-N morphology. a) Compiled bathymetry (0.0003° cell size) map showing both FRSC1 and FRSC2. The axis lies within an axial valley similar to MTJ-S, but the axis itself is defined by a volcanic ridge. Black box shows b) and c) location. b) Compiled bathymetry (0.0001° cell size, 50 m contour interval, labels in km) map centered on the FRSC2-2 third-order segment. The axis forms a rounded volcanic ridge with up to ~400 m of relief. c) Compiled backscatter (0.0001° cell size) image showing acoustic textures along FRSC2-2. While the data are of variable quality, lobate margins and high backscatter intensity associated with relatively recent lava flows can be distinguished in some locations.

is situated within a ~10-12 km wide basin similar in depth to the MTJ-S axis, bounded by faults with throws of ~100-200+ m, similar to those bounding the MTJ-S axial valley (*Fig. 2.5a*). The seafloor outside of the bounding faults is shallower, less faulted, and has a more volcanic morphology compared to the valley floor, again similar to the MTJ-S, implying that a similar transition in crustal accretion processes occurred here. However, the much shallower and higher relief volcanic ridge along the axis itself indicates that it is currently in a more magmatic mode of crustal accretion. Volcanism along this segment appears to be dominated by effusive activity, based on the relatively high backscatter and lobate margins of some of the flows (*Fig. 2.5c*).

2.4.1.3. Arc-proximal Segments: FRSC3 and FRSC4

The FRSC3 and FRSC4 segments are located ~50-70 km west of the Tofua arc (*Fig. 2.3*), ~30-40 km south of the offset in the northern portion, and spreading rates decrease southward from ~23-14 mm/yr [*Sleeper and Martinez, 2015*]. Axial morphology is characterized by shallow steep-sided volcanic ridges with relief of ~500-800 m, reaching depths above 1500 m in some locations (*Fig. 2.6a,b*). Off-axis volcanic cones are more abundant here compared to FRSC-N. The two most prominent examples, with relief of over 1000 m, are located a few km west of the axis at ~16°40'S and 17°07'S (*Fig. 2.6a*). The basin that surrounded the northern segments disappears along FRSC3, and the large off-axis bounding faults taper out and are no longer visible south of ~16°40'S. Based on dredged pillow basalts [*Keller et al., 2008*] and high acoustic reflectivity along most of the segment, effusive volcanism appears to be dominant. However, the lower backscatter and streaky acoustic texture of the material draping the ridge flanks along some segments (e.g., FRSC3-7, *Fig. 2.6c*), interpreted here as volcanoclastic sediments, indicate that explosive volcanism occurs along portions of the axis. These volcanoclastics may be sourced from small (~100-200 m diameter) volcanic cones scattered along the ridge-crest (*Fig. 2.6b*). This acoustic texture is analogous to that observed at VFR in the southern Lau Basin [*Sleeper and Martinez, 2014*], which is comparable to FRSC3 and FRSC4 in terms of axial morphology and arc proximity. At VFR, bottom photographs confirmed the presence of volcanoclastics (hyaloclastite sands) [*Von Stackelberg and Weidicke, 1990*] associated with the “streaky” low backscatter acoustic texture we describe here. Some of this texture may be due to mass wasting, but the existence of mass wasting along the ridge flanks is consistent with the presence of abundant loose volcanoclastic material, so the two interpretations

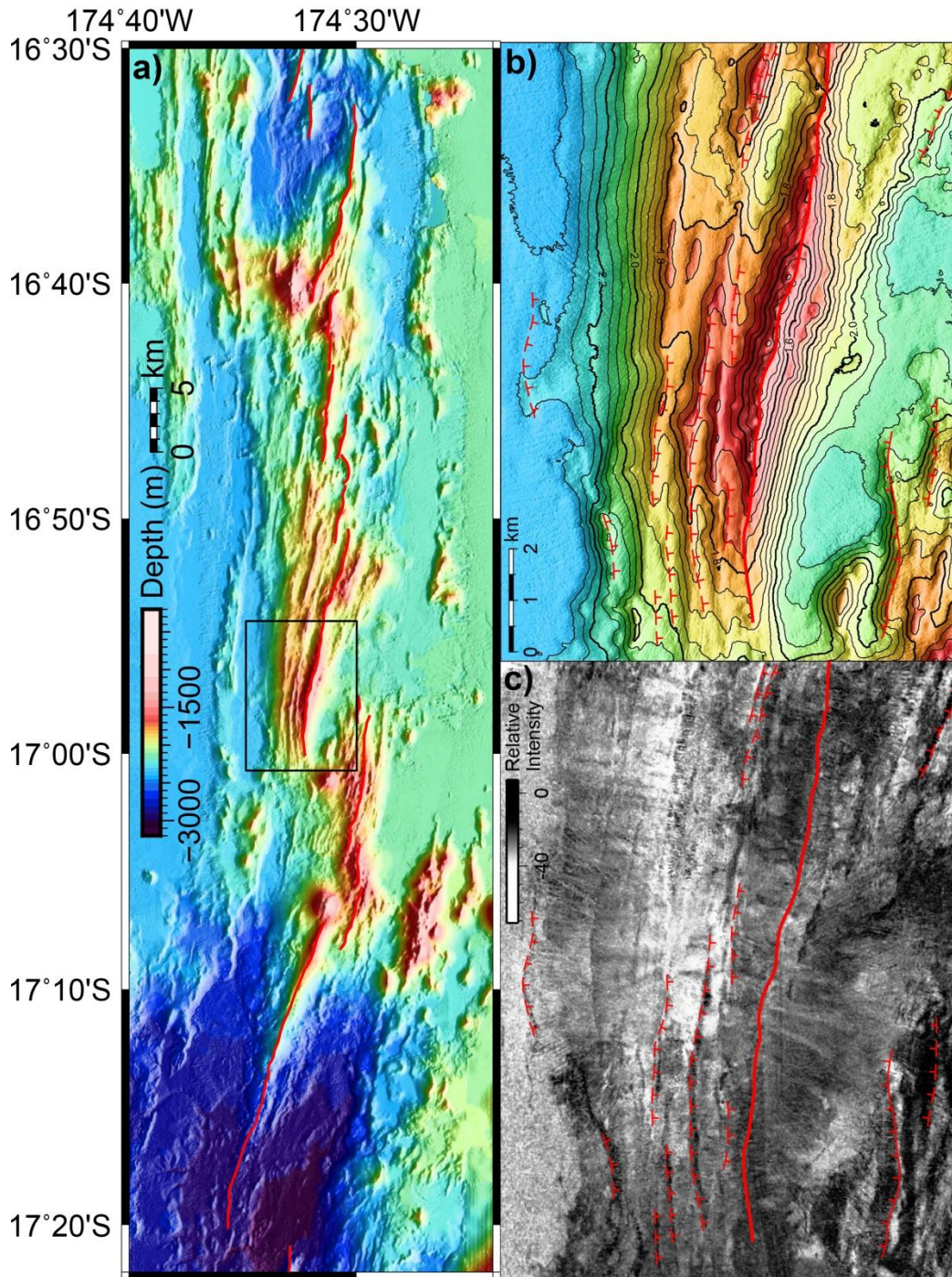


Figure 2.6: FRSC-C morphology. a) Compiled bathymetry (0.0003° cell size) map showing FRSC3 and FRSC4. The axis is well defined by a steep-flanked volcanic ridge, and the faults bounding the valley surrounding FRSC-N taper out by ~16°40'S. Also note the increasing size and abundance of off-axis volcanic cones compared to FRSC-N (e.g., 16°40'S, 17°01'S, 17°07'S). b) Compiled bathymetry (0.0001° cell size, 50 m contour interval, labels in km) map centered on the FRSC3-7 third-order segment. The axis here is defined by a steep volcanic ridge with over 800 m of maximum relief, numerous small volcanic cones dot the ridge crest. c) Compiled backscatter (0.0001° cell size) map showing the relatively low backscatter intensity and streaky acoustic texture interpreted as volcaniclastic material draping the ridge flanks. Darker patches toward the north end of the image indicate some effusive activity as well, although the flow margins are indistinct.

are not mutually exclusive. At the south end of FRSC4, the axial ridge dives steeply down and terminates within the deep basin surrounding FRSC-S.

2.4.1.4. Arc-like Segments: FRSC5 and FRSC6

The southern end of the FRSC approaches the arc from ~50 km to 25 km southward, terminating in a zone of active rifting by $\sim 17^{\circ}54'S$, while spreading rates decrease from $\sim 14\text{-}8$ mm/yr by the southern tip of the mapped axis [Sleeper and Martinez, 2015]. Axial morphology is dominated by prominent volcanic cones near the center of each segment that closely resemble arc volcanoes (Fig. 2.7a) in both morphology and lava chemistry [Keller et al., 2008; Escrig et al., 2012]. Volcanic rift zones aligned with the segments to the north here define the spreading axis, indicating that these are active extensional features. The cone within FRSC5 has relief of over 1500 m and summit depths of under 1000 m, while the cone within FRSC6 has similar relief relative to the surrounding seafloor but shoals to depths of under 600 m (Fig. 2.7b). Based on the low intensity and streaky texture in the sonar backscatter data (Fig. 2.7c), the upper flanks of the cones are draped with volcanoclastic debris, but the lower flanks and nearby seamounts show evidence of effusive volcanic activity as well. The southernmost cone is hydrothermally active [Resing et al., 2012]. Surrounding these cones, the axis is poorly defined by elliptical seamounts that in some cases coalesce into volcanic ridges. It is difficult to determine which structure is most recently active and extension may be accommodated across more than one adjacent structure. All of these volcanic features lie within a flat, sediment-covered basin reaching depths greater than 3000 m, deeper than the basin surrounding MTJ-S and FRSC-N. The east and west margins of this deep basin are defined by sharp uplifted faults scarps with over 1500 m of relief associated with the initial rifting event.

2.4.2. Gravity Anomalies

The mantle Bouguer anomaly plotted in Fig. 2.8 was calculated by removing the gravitational effects of the seafloor and 7 km thick crust from the satellite-derived free-air anomaly (Fig. 2.3b) in order to highlight variations from typical oceanic crust. Relative differences in gravity anomaly values largely reflect changes in crustal thickness and mantle density. Long-wavelength density variations primarily due to thermal variations in the mantle wedge and to the presence of the subducting slab are reflected in the data as well, but the

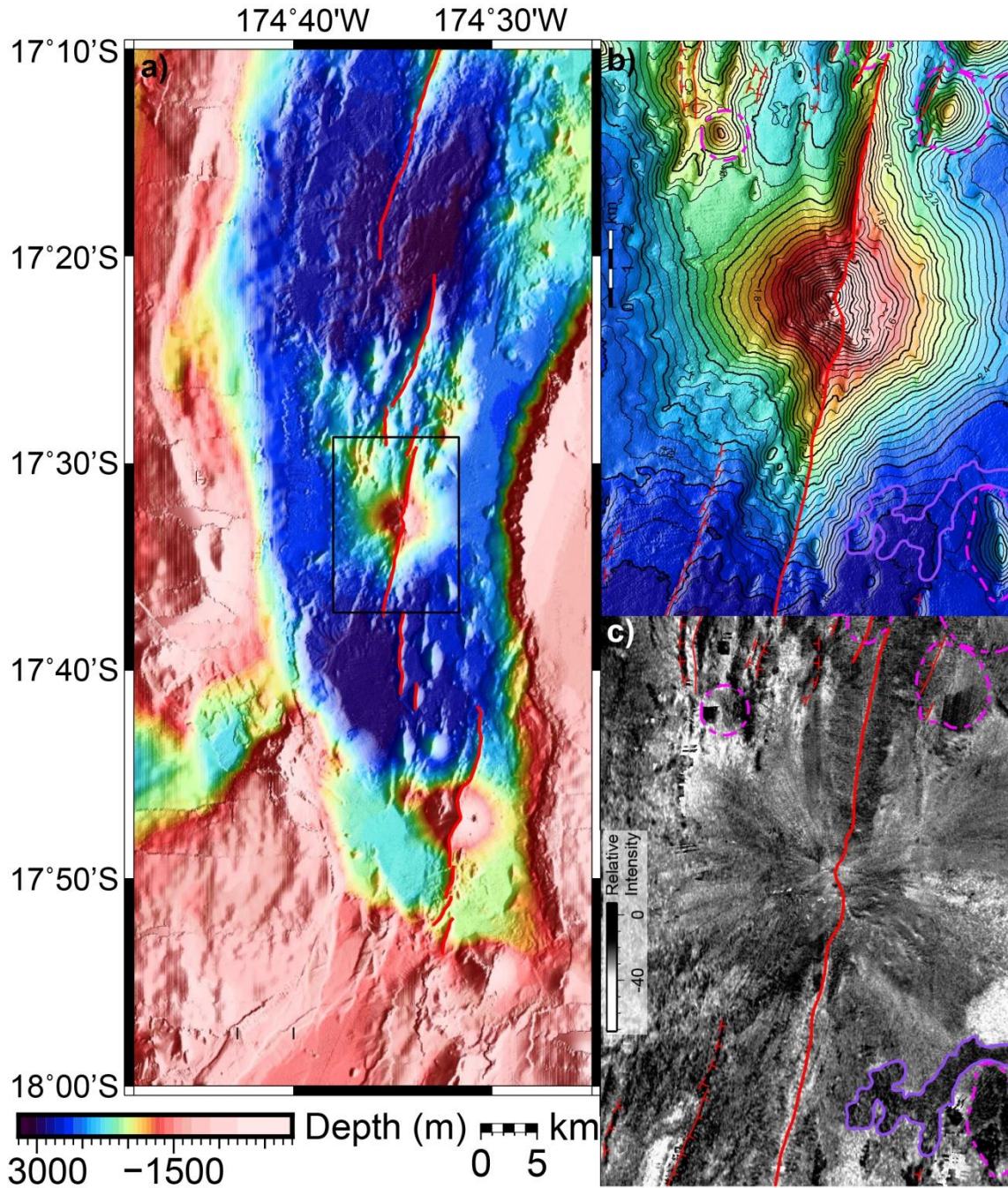


Figure 2.7: FRSC-S morphology. a) Compiled bathymetry (0.0003° cell size) map showing FRSC5 and FRSC6. The center of each segment is dominated by large volcanic cones with over 1500 m of relief, within anomalously deep seafloor. Volcanic rift zones cutting through the cones define the axis, and away from these cones the axis is less well-defined by the crests of coalescing elliptical seamounts. b) Compiled bathymetry (0.0001° cell size, 50 m contour interval, labels in km) map showing the large axial volcanic cone along the FRSC5-4 third-order segment. The summit rises over 1600 m above the surrounding seafloor, reaching depths above 1000 m, much shallower than any part of the axis to the north. Volcanic rift zones extending north and south from the peak of the cone are evidence of active extension. c) Compiled backscatter (0.0001° cell size) image showing relatively low backscatter intensity and a streaky texture similar to FRSC3-7, associated with volcaniclastic material draping the cone flanks. Evidence of some effusive activity can be observed as well, but again the flow margins are difficult to map accurately.

important smaller-scale features related to arc volcanism and backarc spreading are still distinguishable. Two major features to note are the broad gravity lows corresponding to the pre-existing thick, low-density arc crust outside of the FRSC rifted margins, and the roughly triangular relative gravity high under the thinner backarc crust formed along the FRSC and MTJ-S. Particularly notable are the highest anomalies corresponding to the deep, flat crust surrounding the FRSC-S axial cones, suggesting that the crust is anomalously thin around these volcanoes. Bulls-eye lows associated with the thick crust under the axial cones become more elongate and lower in amplitude as the axial cones transition to axial ridges along the segments toward the north. These relative gravity lows that directly underlie the axis disappear toward the north end of the FRSC.

2.5. Discussion

2.5.1. General Trends with Arc Proximity, Comparison with ELSC/VFR

With the exception of the large volcanic cones along FRSC-S, general trends in axial morphology with arc proximity along the FRSC/MTJ-S are similar to the ELSC/VFR in the southern Lau Basin [Martinez and Taylor, 2002; Sleeper and Martinez, 2014]. At distances greater than ~70 km from the arc, along the MTJ-S1/2 (Fig. 2.9a) and ELSC1/2 (Fig. 2.9b) segments, axial morphology is characterized by a deep, faulted axial valley with only minor irregular, low-relief volcanic ridges. The transitional segments (FRSC1/2 (Fig. 2.9c) and ELSC3/4 (Fig. 2.9d)) are characterized by a rounded volcanic ridge that shoals and increases in relief toward the south. Arc-proximal segments (FRSC3/4 (Fig. 2.9e) and VFR1/2 (Fig. 2.9f)) are characterized by shallower, steep-sided volcanic ridges often draped with volcanoclastic material, indicative of high magmatic water contents. This gradual shoaling and increased ridge relief are an expression of the increasing contribution of slab-derived hydrous melts as the axis approaches the arc. At the FRSC, geochemical data suggest that this contribution may be even greater than at the ELSC/VFR. The lavas along the FRSC have more arc-like compositions [Keller et al., 2008; Escrig et al., 2012] and the segments have more magmatically robust axial morphologies compared to the ELSC at similar distances from the arc. Based on dredged samples from volcanoes K, J North, J South, and I (Fig. 2.10), Keller et al. [2008] suggest that

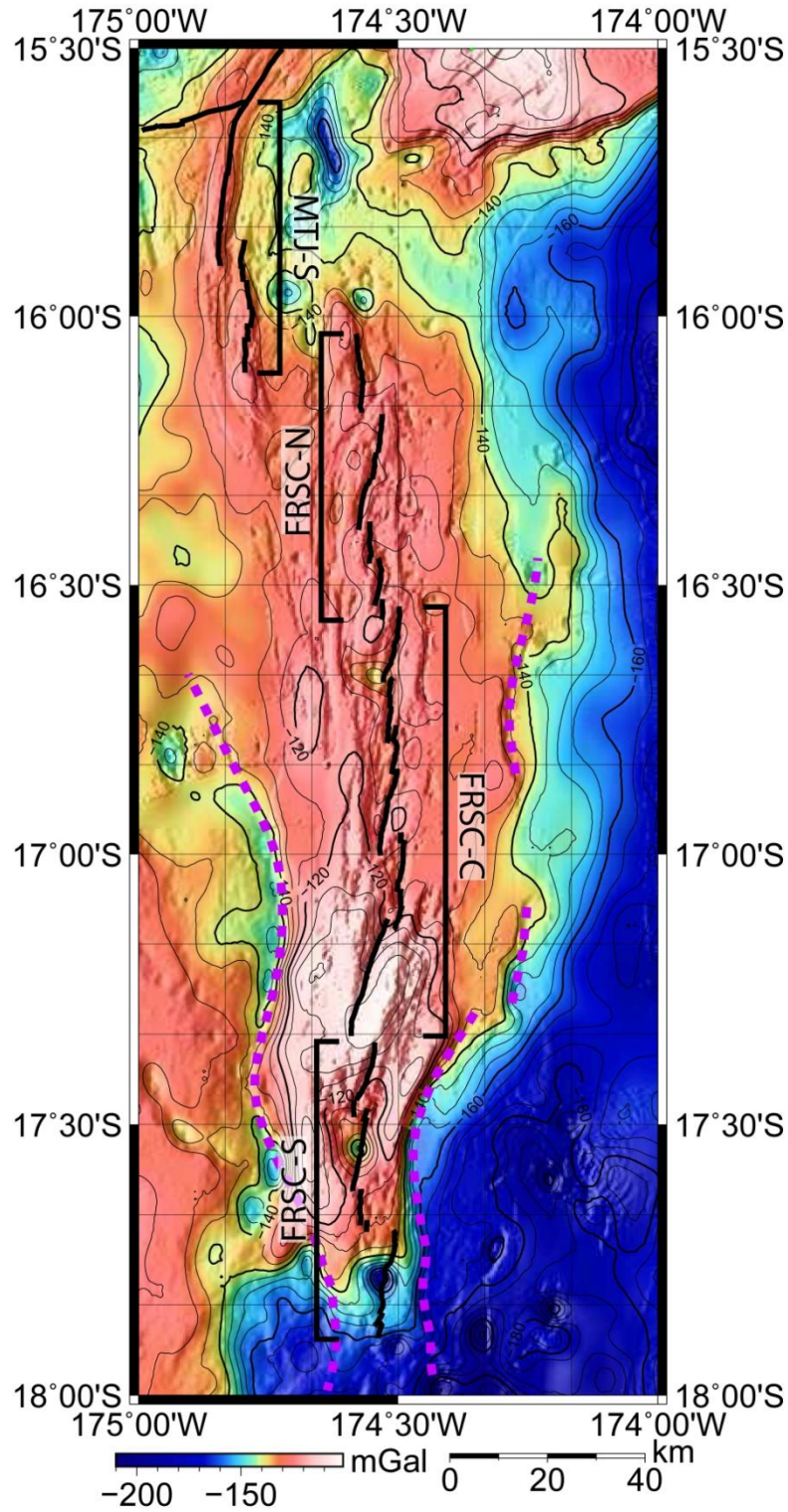


Figure 2.8: Mantle Bouguer anomaly, calculated by removing the gravitational effects of 7 km thick basaltic crust from the Bouguer anomaly using the satellite-derived grid of Sandwell *et al.* [2014] and swath bathymetry (multibeam and H-MR1) with off-axis gaps filled by predicted bathymetry (see Fig. 2.3 for data distribution). The spreading axis is mapped in black and prominent rifted margins are shown as dashed magenta lines. Refer to section 2.4.2 for discussion.

they are extinct, and propose that the arc-like lava compositions and increased magmatism could be explained by the FRSC capturing the arc melt. It is unclear whether this actually reflects a higher magma supply along the FRSC, or simply higher magma supply relative to slower spreading rates.

2.5.1.1. FRSC-S Morphology: Along-axis Melt Focusing due to Ultraslow Spreading Rates?

The large volcanic cones along FRSC-S represent a departure from the general trends discussed above with no analogue in the ELSC/VFR system, and thus must reflect different conditions. The cause of this abrupt morphologic change is an important question regarding the nature and evolution of the FRSC. Along the volcanic ridge segments north of FRSC5, volcanism is distributed along the length of the segment, although local peaks in axial topography and large off-axis volcanic cones along some segments indicate that melt distribution is more complex than a simple linear trend with arc proximity. Along FRSC-S, the volcanic cones are surrounded by a few small elliptical seamounts, and exceptionally high gravity anomalies (*Fig. 2.8*) indicate that the deep seafloor has thin crust and possibly even no crust as at Gakkel Ridge [*Michael et al., 2003*], although it has not been sampled directly due to sedimentation. These observations indicate that melt is being more efficiently focused toward the individual edifices rather than distributed along the entire segment. One factor that could account for this apparent along-axis focusing of melt are the ultraslow spreading rates along FRSC-S, which decrease from ~14-8 mm/yr southward [*Sleeper and Martinez, 2015*].

Ultraslow (<12 mm/yr) MORs provide an analogous environment where this melt focusing process is observed. At ultraslow rates, the plate-driven component of advection is minimized compared to the buoyancy-driven upwelling of the melt, preserving the 3-D diapiric upwelling pattern of melt in the mantle. This results in a series of spaced point-source volcanic features with intervening deep amagmatic segments [*Dick et al., 2003*], such as the volcanic seamounts along the Southwest Indian Ridge [*Dick et al., 2003; Standish et al., 2008*], and Gakkel Ridge [*Dick et al., 2003*]. An analogous backarc example may be the Kinan Seamount Chain along the Shikoku basin spreading center [*Ishizuka et al., 2009*], a now-extinct BASC south of Japan where similar spaced point-source volcanic features formed as spreading waned and rates decreased to zero. *Taylor and Martinez [2003]* also suggested that slow backarc opening in parts of the Mariana Trough may help preserve 3-D patterns of mantle flow and melt

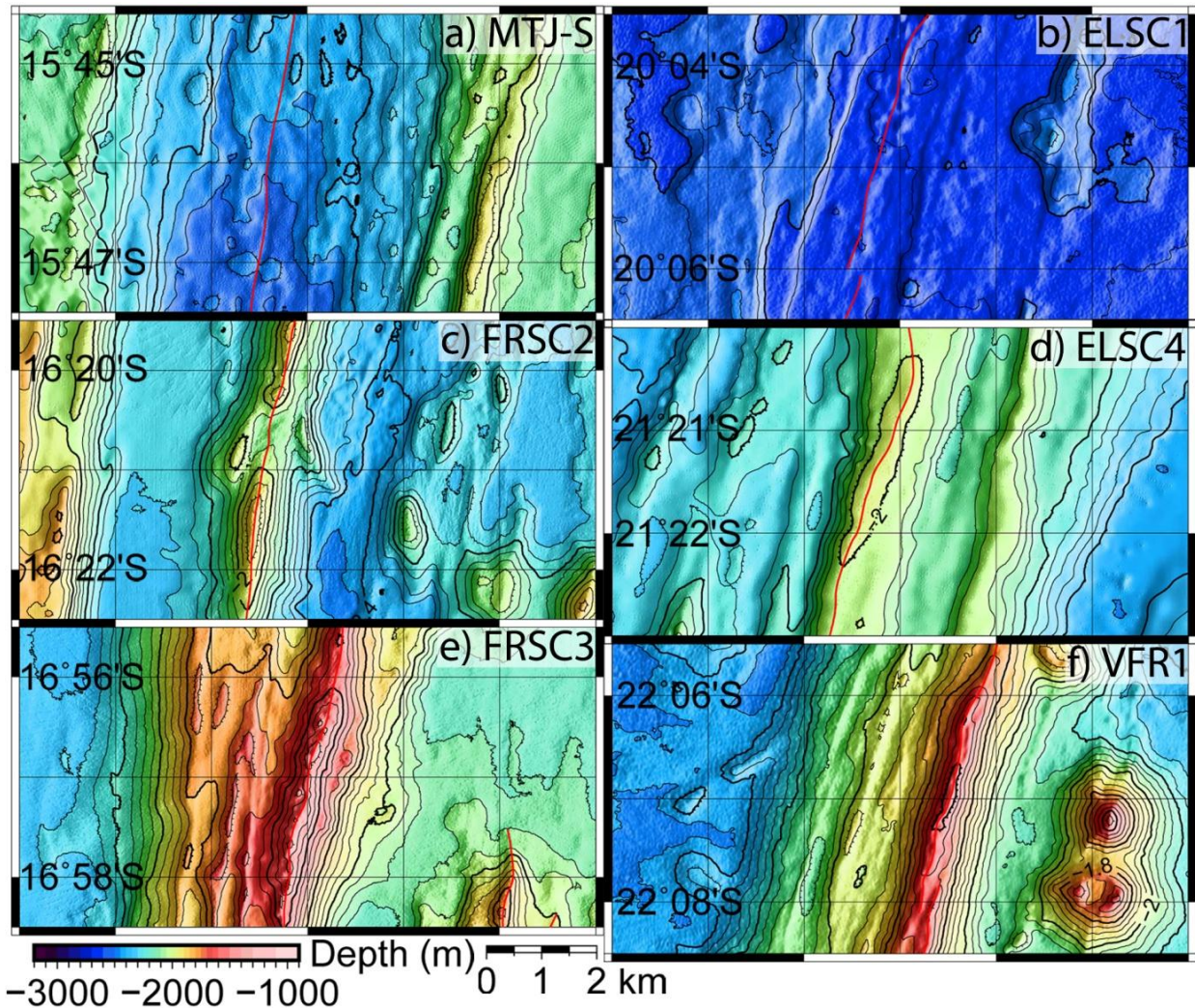


Figure 2.9: Bathymetry maps (0.0001° cell size, 50 m contour interval) comparing type examples of FRSC/MTJ-S morphology (left side) and ELSC/VFR morphology (right side). Both spreading systems show similar trends in morphology with arc proximity (with the exception of the FRSC-S segments). Arc-distal segments (MTJ-S and ELSC1/2): ~flat seafloor within an axial valley; Transitional segments (FRSC-N and ELSC4): rounded volcanic ridge with a few 100 m of relief; Arc-proximal segments (FRSC3/4 and VFR1/2): shallow, steep-sided volcanic ridge with ~500-800+ m of relief. Refer to section 2.5.1. for further discussion.

generation. At faster spreading rates (>50 mm/yr), the plate-driven component dominates, promoting a more elongate two-dimensional upwelling pattern that favors long volcanic ridge segments like those along the East Pacific Rise [Macdonald *et al.*, 1992], or the ELSC/VFR in the southern Lau Basin, where spreading rates vary from ~103-47 mm/yr southward [Sleeper and Martinez, 2016].

Another notable aspect of the morphologic transition along the FRSC is its abrupt nature. Rather than a gradual decrease in segment length and a gradual transition to the volcanic cone morphology, the ridge abruptly ends at the south end of FRSC4 and axial morphology becomes

dominated by the central volcanic cones along FRSC-S. This suggests that there may be a spreading rate threshold (~10-15 mm/yr?) below which the nature of crustal accretion and along-axis melt transport fundamentally changes. The threshold below which ultraslow behavior is documented at MORs is ~12 mm/yr as well (although "ultraslow" characteristics are seen at up to 20 mm/yr) [Dick *et al.*, 2003], but a key difference at the FRSC is enhanced magmatism due to a generally more hydrous mantle in the arc-proximal mantle wedge compared to MORs. This could explain the presence of the small elliptical seamounts scattered on the deep seafloor between the cones, which are distinct from the amagmatic segments with common mantle exposures at ultraslow MORs [e.g. Dick *et al.*, 2003; Michael *et al.*, 2003]

2.5.1.2. FRSC-S Morphology: Rifting vs. Spreading?

The FRSC-S was previously interpreted to be in a stage of active rifting rather than spreading [Zellmer and Taylor, 2001]. Spaced volcanic edifices often form within active rift valleys and the anomalously thin crust surrounding them could potentially be explained by tectonic thinning of pre-existing lithosphere, however the following observations support an ultraslow spreading interpretation. Teleseismic earthquake activity is limited to the uplifted rift margins adjacent to and south of the FRSC6 segment and is absent in the valley, consistent with the spreading interpretation. However, micro-seismicity within the rift valley [Conder and Weins, 2011] could be interpreted as consistent with either rifting or ultraslow spreading. Large faults (>100 m throw) are limited to the main rift margins and down-dropped fault blocks are only visible along the western margin (*Fig 2.7a*). There are neither large faults nor down-dropped or rotated blocks within the valley floor, supporting the interpretation of an abrupt phase of rifting followed by spreading. The available data are limited and thus it is difficult to rule out rifting definitively, but the evidence favors ultraslow crustal accretion and melt focusing.

2.5.1.3. Morphologic Correlations with the Arc

Along with the progressive changes in the morphology and magmatic character of the axis, axial topography along both the FRSC/MTJ-S and ELSC/VFR spreading systems is punctuated by local high points correlated with the projected locations of arc volcanoes [Escrig *et al.*, 2009; Sleeper and Martinez, 2014]. In both systems, these correlations become more apparent toward the south, but are more clearly expressed overall along the FRSC. *Fig. 2.10a*

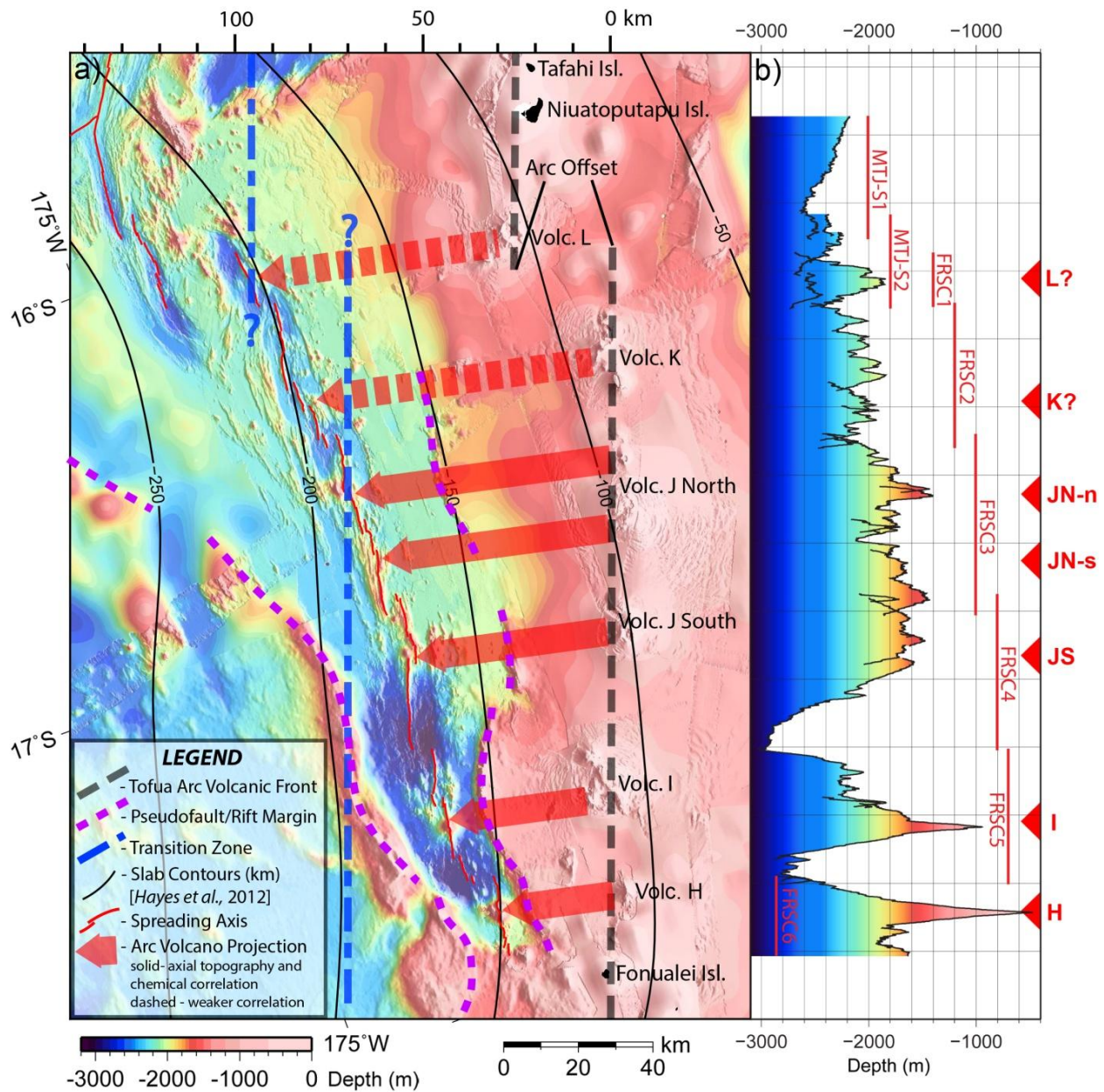


Figure 2.10: a) Oblique mercator bathymetry map (0.001° cell size) of the FRSC/MTJ-S with the arc volcanic front vertically aligned to highlight variations with arc proximity. Red arrows are drawn parallel to the GPS-derived motion of the Pacific plate [Phillips, 2003] (an approximation of the slab flow line) from the arc volcanoes toward the spreading axis. The blue dashed line is drawn ~70 km west of the arc, and represents the surface projection of a hypothesized boundary in the mantle wedge between less and more hydrous domains, reflected on the surface as abrupt changes in axial morphology. Other symbols are defined in the legend. b) Axial topographic profile along the FRSC/MTJ-S. Shows general trend of decreasing depth toward the south with arc proximity, as well as local peaks in axial topography associated with the projected locations of arc volcanoes (red triangles). Second-order segments are shown schematically with red lines. Refer to section 2.5.1 for further discussion.

shows the FRSC/MTJ-S and the adjacent portion of the Tofua arc, and the projection is aligned with the arc to highlight variation in arc proximity. The red arrows in Fig. 2.10a (which correspond to the red triangles in Fig. 2.10b) show the slab flow lines from arc volcanoes based

on the GPS-derived motion of the Pacific plate relative to the station on Niuatoputapu Island [Phillips, 2003]. Along FRSC1, Volcano L projects toward the center of the volcanic ridge, which forms a subtle local topographic high point. Volcano K projects toward the south end of FRSC2, and while there is not a clear local high point in axial topography, there is a shallow elongate volcanic cone just a few km east of the axis. Along FRSC3 and FRSC4, the large off-axis volcanic cones at $\sim 16^{\circ}40'S$ and $17^{\circ}07'S$ correlate with local topographic high points along the adjacent axis and coincide with the projected locations of two arc volcanoes (Fig. 2.10), a similar but more apparent correlation than that seen along FRSC-N. The large volcanic cones that define the centers of FRSC5 and FRSC6 also correlate well with the projected locations of Volcano I and Volcano H north of Fonualei Island (Fig. 2.10). Along the ELSC, the arc correlation is more subtly expressed as undulations in axial topography that reach their minimum depth near second-order segment ends [Sleeper and Martinez, 2014].

2.5.1.4. Geochemical Correlations with the Arc

In both the FRSC/MTJ-S and ELSC/VFR systems, the geochemical data express similar correlations to the topographic correlations between the arc and axis. Keller *et al.* [2008] analyzed samples along the FRSC and MTJ axis and concluded that most of the FRSC samples had strong affinities to arc volcanism in terms of trace element and isotopic indicators, with little to no latitudinal variation. Escrig *et al.* [2012] used a more complete sample suite and new analyses to demonstrate that there are systematic geochemical variations with latitude. They also identified spikes in multiple trace element indicators of subduction input along the FRSC axis where the arc volcanoes project along slab trajectories. In their study, the projections were drawn orthogonal to the arc and thus deviate slightly from our projections based on the Pacific-Tonga GPS vector at Niuatoputapu [Phillips, 2003], but the general correlation holds true in either case. Escrig *et al.* [2009] performed a study of axial lava samples along the ELSC/VFR, and found a similar correlation along the VFR1 segment. With additional data included, this correlation was expanded to the adjacent VFR2 and ELSC4 segments in Sleeper and Martinez [2014].

2.5.1.5. Arc-Distal Segments

Beyond ~ 70 km from the arc along both the FRSC/MTJ-S and ELSC/VFR, these systematic morphologic and geochemical changes and arc-to-axis correlations disappear and the

volcanic ridges are abruptly replaced by deep, flat, faulted seafloor. Along the ELSC/VFR, where geophysical and geochemical data are more abundant, this change in morphology is accompanied by abrupt changes in crustal thickness (~1.9 km of thinning over a ~5 km lateral distance) and lava composition, from thicker, lower density and lower seismic velocity basaltic andesites south of the transition zone, to denser higher seismic velocity basaltic crust along ELSC2 and ELSC1 in the north [Escrig *et al.*, 2009; Dunn and Martinez, 2011]. It has been suggested that this abrupt change in crustal properties reflects an abrupt change in mantle properties from a hydrous mantle wedge corner with strong slab geochemical signatures to a less hydrous mantle at greater separation from the arc [Dunn and Martinez, 2011].

The nature of this transition (blue dashed line in *Fig. 2.10*) along the FRSC is not as clear due to less abundant geochemical and geophysical data. There is a change from basaltic lavas (~49-52% SiO₂) along MTJ [e.g. Falloon *et al.*, 1992; Keller *et al.*, 2008; Tian *et al.*, 2011] to basaltic andesites (~52-54% SiO₂) along FRSC-N [Keller *et al.*, 2008; Escrig *et al.*, 2012], although sampling is not as dense as along the ELSC. The lack of seismic data in this region limits the ability to quantify the change in crustal thickness. However, the similarities in the observed changes in axial morphology and depth between the ELSC and FRSC/MTJ-S isostatically imply a comparable change in crustal thickness and suggest that they result from a similar underlying process. Furthermore, the transition appears to begin at a similar depth above the slab in both systems. The well-defined transition along the ELSC occurs above the ~190 km slab contour [Sleeper and Martinez, 2014], and the bounding faults that separate the deeper near-axis seafloor from the shallower off-axis seafloor along the FRSC also begin to develop over the ~180-190 km slab contour (*Fig. 2.10*).

Determining the location of this transition zone relative to the arc is complicated by the offset in the northern portion, and the evidence suggests that it may change location over time. MTJ-S is beyond 70 km regardless of which portion of the arc it is measured from, but it is less clear for FRSC-N. If measured from the southern portion of the arc, FRSC1 and FRSC2 are both on the arc-distal side of the transition zone and should therefore display axial valley morphology similar to MTJ-S. If measured from the northern offset portion, FRSC1 and FRSC2 are both within 70 km and should therefore display a more magmatic volcanic ridge morphology. The rounded volcanic ridge defining the FRSC-N axis suggests that the axis is currently in a more

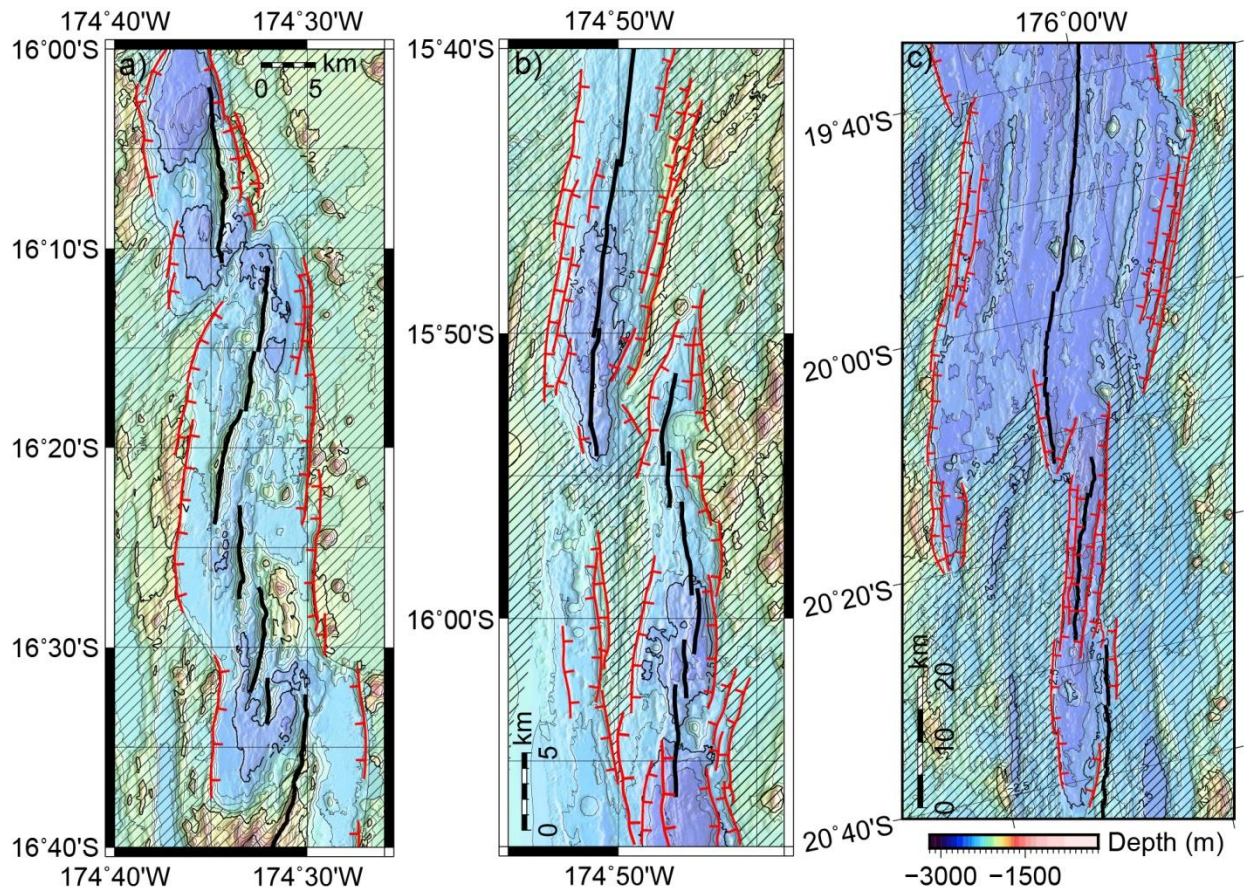


Figure 2.11: Side-by-side comparison of on- and off-axis morphology showing a similar abrupt change in depth and morphology in each location: a) FRSC-N, b) MTJ-S, and c) ELSC1/2. Shallower seafloor (striped pattern) with more volcanic constructional features than tectonic features (and thicker crust along the ELSC flanks [Dunn and Martinez, 2011]) can be seen away from the ridge axis, in contrast to the deeper, flatter seafloor near the axis. Major faults associated with the boundary between these crustal domains are mapped in red with ticks pointing down-dip, the spreading axes (third-order segments) are mapped with black lines. Refer to section 2.5.1. for further discussion.

magmatic mode of crustal accretion, while the deep basin and large bounding faults away from the axis suggest that these segments were at least temporarily similar to MTJ-S and ELSC1/2.

Fig. 2.11 compares the three regions side by side, and highlights the locations of the bounding faults separating the deeper near-axis seafloor and shallower off-axis seafloor (striped pattern in Fig. 2.11). In the simplest interpretation, it appears that the axis has gone from accreting shallower, more magmatic crust similar to that along FRSC3 or ELSC4, to a phase of accreting deeper, flatter crust like MTJ-S, and is now back in a more magmatic mode of accretion. More geophysical and geochemical data are required to understand the details behind how this evolution unfolded, and the mechanism for creating the apparent offset in the arc remains an intriguing unresolved question.

2.5.1.6. Morphologic Correlations with Hot Spot-Proximal Ridges

The morphologic changes with arc proximity along the FRSC and other backarc spreading centers are in many ways analogous to those observed at hot spot-proximal ridges, such as the Galápagos Spreading Center (GSC) [Canales *et al.*, 1997] and Reykjanes Ridge (RR) [Laughton *et al.*, 1979]. In both environments, magma supply to the ridge axis increases primarily with proximity to either the arc or the hot spot. The GSC and RR axes shoal toward the hot spot, and there is a transition from an axial valley to an axial high, despite minimal along-axis variation in spreading rate. It is interesting to note that similar morphologic changes result from a chemical anomaly (slab-derived water) in the mantle and what is typically interpreted as a thermal anomaly (the hot spot). This supports the interpretation of Canales *et al.* [2002] that the density anomaly associated with the Galápagos swell required a compositionally buoyant mantle source in addition to the predicted thermal anomaly.

Observations at the GSC also indicate that high magma supply can have a melt focusing effect independent of spreading rate. White *et al.* [2008] discussed the existence of large volcanic cones (~1-3 km in diameter, >100 m high) along the crest of the axial high in the most hot spot-proximal portion of the GSC. These cones were interpreted to reflect focusing of magma toward the center of the volcanic segments. However, this portion of the GSC is not entirely analogous to the FRSC-S in that the volcanic cones are constructed along the crest of an inflated axial ridge rather than isolated cones within an axial valley. Furthermore, the scale of the central cones along the FRSC-S is an order of magnitude greater than the GSC cones, although the elliptical seamounts surrounding the central cones are comparable in size. Thus, while we believe that the ultraslow spreading rates along the FRSC-S are still the primary cause of the observed morphologic change, the high magma supply could act to reinforce this effect and increase magma focusing toward the central edifices.

2.5.2. Model of Mantle Wedge Structure

The observations discussed above support a model of mantle wedge structure similar to the one presented in Sleeper and Martinez [2014] to explain the morphologic and geochemical changes along the ELSC/VFR. This model is characterized by a mantle wedge with 3 distinct chemical/rheological domains [Martinez and Taylor, 2002; Dunn and Martinez, 2011]. Domain I

corresponds to normal MORB-source mantle, which underlies BASC's >150-200 km away from the arc beyond the direct influence of the subducting slab. Domain II represents a hypothesized strongly hydrous mantle wedge corner with an abrupt edge at ~70 km from the arc. The exact distance from the arc likely varies with slab dip and convergence rate, but appears to be similar between the FRSC and ELSC. This abrupt edge corresponds with the abrupt changes observed in morphology and lava chemistry along both the ELSC and FRSC/MTJ-S. While we favor an abrupt chemical and rheological boundary in the mantle, it may be possible to explain the abrupt changes through a change in melt transport mechanism [Escrigo *et al.*, 2009]. More data are needed to definitively resolve the underlying cause of the abrupt changes. Within Domain II, there is a gradient of increasing water content toward the arc, which is supported in chemical data [Kelley *et al.*, 2006] and explains the shoaling and increasing magmatic character of the spreading axis with arc proximity. Another important feature of Domain II is the "fingers" of even more hydrous (or hotter [Tamura *et al.*, 2002]) material, extending from under the arc volcanoes to the backarc. Elongated spaced zones of hydrous buoyant upwelling and increased melt production can explain the chemical and topographic correlations between the arc volcanoes and the axis observed in both the ELSC/VFR and FRSC/MTJ-S systems and shown schematically with the red arrows in Fig. 2.10. Previous studies in subduction zones have shown that the mantle wedge becomes progressively depleted closer to the arc [Woodhead *et al.*, 1993; Hochstaedter *et al.*, 1996; Hochstaedter *et al.*, 2000] due to previous melting, and perhaps some recirculation of depleted material [Martinez and Taylor, 2006], effectively creating a gradient of increasing depletion toward the arc. Domain III is where this material extends beyond ~70 km from the arc outside of Domain II, creating a zone of depleted mantle with distinctly lower water content than Domain II. The axes of arc-distal segments (>70 km away) advect this depleted and less hydrous Domain III mantle, causing an abrupt drop in melt production and giving rise to the deep, flat seafloor characteristic of ELSC1/2 and MTJ-S1/2. The axes of arc-proximal segments (<70 km away) advect more hydrous Domain II material, producing thicker crust and a volcanic axial high.

2.5.3. Opening Rate Effects on the Volcanic Expression of Backarc Crustal Accretion

To put the FRSC observations in a larger context, it is useful to compare the patterns seen here with other backarc environments. An increasing number of studies have identified patterns

in seafloor volcanic and tectonic features that are consistent with the model described here for the FRSC/MTJ-S and ELSC/VFR [e.g. Tamura *et al.*, 2002; Wysoczanski *et al.*, 2010]. These features indicate that the underlying mantle wedge in each subduction zone shares a similar structure, but the seafloor expression of this structure varies with opening rate, as well as extent of opening. *Fig. 2.12* summarizes the observed patterns and arranges the backarc environments in order of increasing opening rate, from the Northeast Japan Arc (*Fig. 2.12a*) where there is no backarc extension to the ELSC/VFR (*Fig. 2.12d*) where opening rates vary from intermediates to fast. At the slow end of the spectrum (*Fig. 2.12a,b*), the underlying "fingers" of hydrous melt extending from the arc volcanoes to the backarc are directly expressed on the seafloor as chains of active volcanoes and elevated topography with intervening regions characterized by decreased volcanism, increased tectonism, and more subdued topography. In the southern Havre Trough, where opening rates are ~15 mm/yr or less, Wysoczanski *et al.* [2010] described zones of shallow, magmatic seafloor (called "arc regime") dotted with active volcanoes extending across the backarc, separated by "rift regime" tectonically faulted deeps. The FRSC-S, opening at <14 mm/yr, shows a similar pattern of alternating zones of increased and decreased magmatism, but the basin is only ~20-40 km wide, versus ~110-140 km wide for the southern Havre Trough. Perhaps given more time and a greater extent of basin opening, the volcanic cones along the ultraslow-opening FRSC-S would mature into something similar to the "arc regimes" of the southern Havre Trough, separated by deep seafloor and thin crust similar to the "rift regimes." Along the FRSC/MTJ-S (*Fig. 2.12c*), we have documented a transition from ultraslow behavior at the southern end where volcanism is focused toward the large axial volcanic cones to a different type of volcanic expression along the northern segments. As discussed in detail in this study, the axis changes abruptly to a volcanic ridge at the FRSC4 segment, suggesting that as spreading rates increase above ultraslow, the more two-dimensional pattern of plate-driven upwelling exerts greater control on melt production and axial morphology. At the ELSC/VFR (*Fig. 2.12d*), which represents the slow to fast-spreading end-member, the axial topographic highs associated with the projected arc volcanoes are more subdued and second-order segments are longer, implying that melt is distributed along the axis even more efficiently than the northern FRSC.

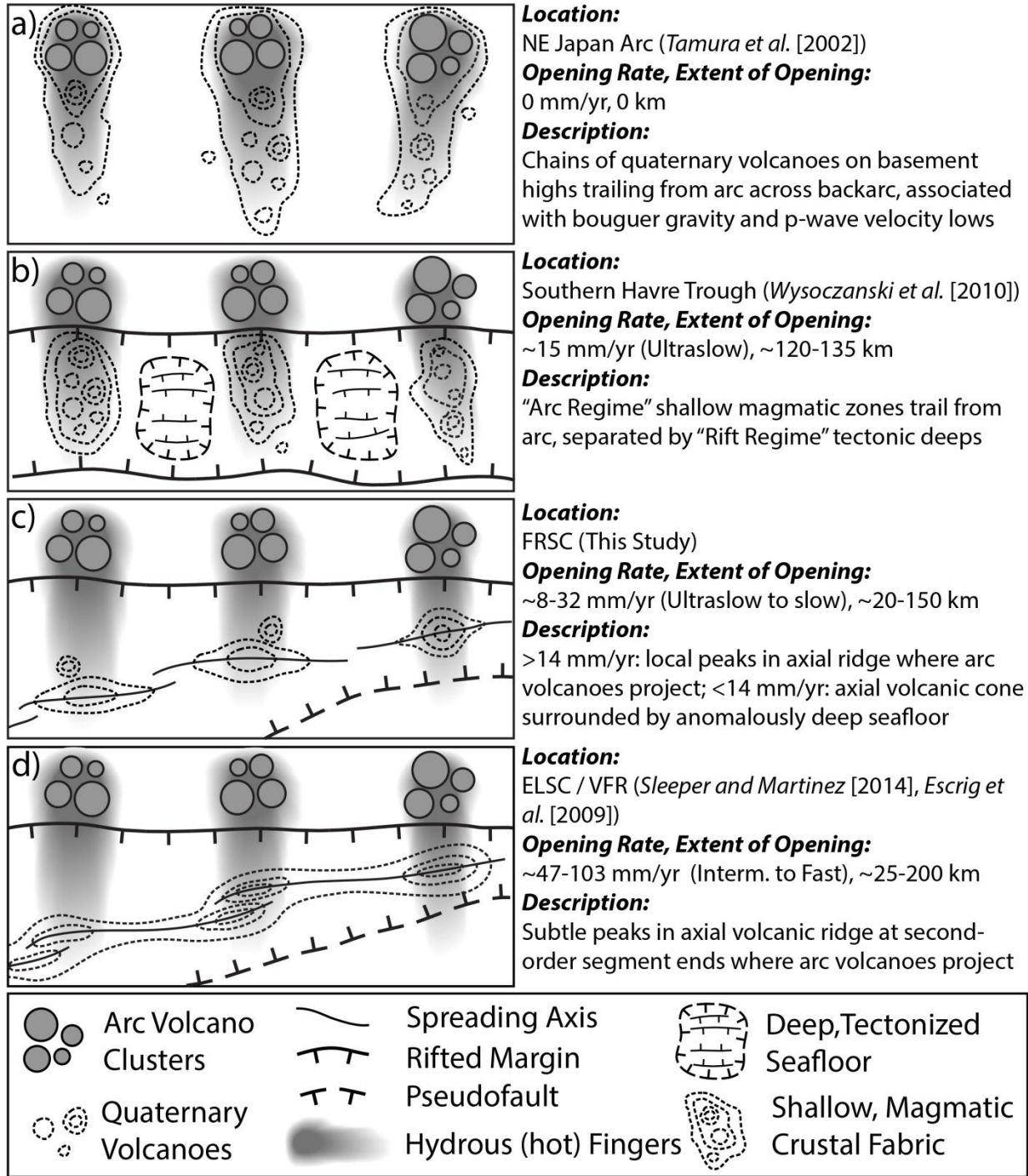


Figure 2.12: Schematic maps comparing the simplified morphology of the arc volcanic front and backarc in four different regions, showing how the volcanic expression of the underlying mantle wedge structure (i.e., the hot [*Tamura et al., 2002*] or hydrus [*Sleeper and Martinez, 2014*] fingers extending across the backarc, shown schematically with gray shading) varies with opening rate and extent of opening. Symbols are defined in the legend below the illustrations. Refer to section 2.5.3 for discussion.

2.6. Conclusions

The characteristics of backarc crustal accretion result from the interplay between two distinct mechanisms of melt production: hydrous flux melting and buoyancy-driven mantle advection due to the addition of slab-derived water to the mantle wedge, and extensional decompression melting and plate-driven advection due to viscous coupling of mantle with the separating lithospheric plates. Hydrous flux melting becomes increasingly important with arc proximity, as evidenced by trends in morphology and axial depth along the FRSC/MTJ-S, ELSC/VFR, and other BASCs [Taylor and Martinez, 2003]. Topographic and geochemical correlations with the arc volcanoes [Escrig *et al.*, 2009, 2012; Sleeper and Martinez, 2014], as well as evidence for abrupt changes ~70 km away from the arc [Escrig *et al.*, 2009; Dunn and Martinez, 2011; Sleeper and Martinez, 2014] show that subduction-related effects are not a simple linear variation with arc proximity. These observations provide insight into the structure and distribution of slab-derived materials in the underlying mantle wedge, and analogous patterns in other backarc environments such as NE Japan and the southern Havre Trough (Fig. 2.12) suggest that the conceptual model (described in section 2.5.2) developed for the ELSC/VFR [Sleeper and Martinez, 2014] and FRSC/MTJ-S may be applicable to other subduction zones. Based on observations along the ELSC/VFR, where opening rates vary from slow to fast, morphologic changes related to arc proximity and across-strike correlations between the arc and axis appeared to be relatively insensitive to variations in opening rate. However, the abrupt morphologic changes along the FRSC-S show that when the plate-driven component is further diminished there is a strong morphologic response. At ultraslow rates (<12 mm/yr) the slab-driven component of hydrous flux melting and 3-D buoyant upwelling is directly expressed on the seafloor as large, spaced volcanic cones like those at the centers of the FRSC5 and FRSC6 segments. These are analogous to point-source volcanic features observed at ultraslow spreading MORs, indicating a similar process of along-axis melt focusing in both environments, although in backarc settings the focusing appears to be conditioned by the locus of hydrous melting along "hot (or hydrous) fingers" that imparts an arc-like geochemical signature to these melts extending basinward from arc volcanoes.

Table 2.1: FRSC/MTJ-S segment measurements and statistics

Order	Name	Length (km)	Offset Width (km) (N end / S end)	Morphology	Axial Depth (m)			
					Mean	Min	Max	Std Dev
1st	FRSC/MTJ-S	256.60	N/A	Variable	2117.5	3033.0	472.3	396.0
2nd	MTJ-S1	34.42	0 (Triple Jxn)/ 5.3L	Graben	2422.9	2634.0	2171.6	128.7
	MTJ-S2	27.55	5.3L / 23L	Graben	2475.0	2740.7	2238.8	128.0
	FRSC1	16.40	23L / 4.2L	Ridge	2190.4	2687.0	1840.6	243.4
	FRSC2	42.49	4.2L / 3.5L	Ridge	2130.7	2535.2	1841.0	139.4
	FRSC3	51.54	3.5L / 4.0L	Ridge	1796.0	2388.9	1406.3	190.3
	FRSC4	43.16	4.0L / 5.8L	Ridge	2080.4	2971.4	1470.6	489.2
3rd	FRSC5	38.93	5.8L / 5.7L	Cone/Ridge	2230.2	3033.0	946.2	454.1
	FRSC6	22.38	5.7L / N/A	Cone/Ridge	1765.1	2696.9	472.3	475.7
	MTJ-S1-1	15.65	0 (Triple Jxn)/ 0.2R	Ridge	2289.3	2394.4	2171.6	52.7
	MTJ-S1-2	11.72	0.2R / 0.3L	Graben	2522.0	2634.0	2396.8	70.3
	MTJ-S1-3	8.32	0.3L / 5.3L	Ridge	2527.6	2620.1	2465.0	36.5
	MTJ-S2-1	6.06	5.3L / 0.4L	Graben	2382.3	2425.6	2321.8	22.1
	MTJ-S2-2	3.65	0.4L / 0.8L	Ridge	2271.7	2297.2	2238.8	13.5
	MTJ-S2-3	6.12	0.8L / 0.4L	Ridge	2418.5	2555.9	2276.2	70.4
	MTJ-S2-4	4.28	0.4L / 0.7R	Graben	2628.6	2690.0	2552.1	32.3
	MTJ-S2-5	3.82	0.7R / 0.7R	Ridge	2545.1	2590.8	2488.4	30.4
	MTJ-S2-6	7.31	0.7R / 23L	Ridge	2573.4	2740.7	2429.1	87.6
	FRSC1-1	16.40	23L / 4.2L	Ridge	2190.4	2687.0	1840.6	243.4
	FRSC2-1	8.03	4.2L / 0.3R	Ridge	2252.6	2535.2	2007.1	128.9
	FRSC2-2	5.64	0.3R / 0.4R	Ridge	2081.8	2301.2	2000.4	70.9
	FRSC2-3	10.95	0.4R / 2.2L	Ridge	2026.5	2300.3	1841.0	118.4
	FRSC2-4	8.71	2.2L / 2.1L	Ridge	2126.1	2373.6	1933.0	120.6
	FRSC2-5	9.79	2.1L / 1.4L	Ridge	2124.8	2452.6	1912.9	115.0
	FRSC2-6	4.24	1.4L / 3.5L	Ridge	2250.9	2472.2	2093.8	93.9
	FRSC3-1	16.02	3.5L / 1.6L	Ridge	1894.4	2388.9	1428.2	222.5
	FRSC3-2	6.40	1.6L / 0.3L	Ridge	1678.1	1926.4	1406.3	171.9
FRSC3-3	7.71	0.3L/ 1.4L	Ridge	1804.9	1966.4	1707.9	60.7	
FRSC3-4	3.61	1.4L / 0.3L	Small Cone	1957.3	2164.6	1708.1	114.5	
FRSC3-5	2.32	0.3L / 0.2L	Ridge	1964.9	2119.5	1895.5	55.0	
FRSC3-6	4.64	0.2L / 1.0L	Ridge	1879.6	2122.1	1712.2	132.2	
FRSC3-7	18.22	1.0L / 4.0L	Ridge	1672.8	1983.8	1433.8	123.7	
FRSC4-1	2.25	4.0L / 0.9L	Ridge	1877.9	2091.1	1719.5	117.4	
FRSC4-2	10.85	0.9L / 0.8L	Ridge	1732.2	1997.0	1583.6	107.1	
FRSC4-3	3.48	0.8L / 0.4L	Ridge	1554.1	1705.6	1470.6	58.8	
FRSC4-4	5.22	0.4L / 2.1R	Ridge	1760.3	2045.9	1652.6	105.0	
FRSC4-5	25.25	2.1R / 5.8L	Ridge	2394.7	2971.4	1573.9	474.2	
FRSC5-1	12.51	5.8L / 0.6R	Ridge	2346.4	3033.0	2049.5	249.2	
FRSC5-2	3.53	0.6R / 2.5	Small Cone	2057.0	2286.8	1837.4	136.8	
FRSC5-3	2.90	2.5L / 0.5L	Small Cone	2105.3	2434.8	1889.6	169.7	
FRSC5-4	15.49	0.5L / 1.8L	Large Cone	1891.2	2882.8	946.2	490.9	
FRSC5-5	7.48	1.8L / 1.4L	Ridge	2721.4	2829.4	2550.6	67.0	
FRSC5-6	2.36	1.4L / 5.7L	Small Cone	2666.2	2868.0	2529.6	103.3	
FRSC6-1	14.60	5.7L / 0.4L	Large Cone	1758.4	2696.9	472.3	599.1	
FRSC6-2	3.03	0.4L / 0.5L	Ridge	1755.4	1875.1	1625.3	75.9	
FRSC6-3	3.06	0.5L / 1.1L	Ridge	1870.2	1924.8	1777.9	42.6	
FRSC6-4	3.39	1.1L / N/A	Ridge	1718.4	1935.8	1623.3	92.6	
4th	Unnamed	~1 to 5 (?)	~≤0.2L/R (devals)	Ridge/Graben	?	?	?	?

CHAPTER 3: GEOLOGY AND KINEMATICS OF THE NIUAFO'OU MICROPLATE IN THE NORTHERN LAU BASIN

Published as: Sleeper, J. D., and F. Martinez (2016) Geology and kinematics of the Niuafu'ou microplate in the northern Lau Basin, *J. Geophys. Res. Solid Earth*, 121, doi:10.1002/2016JB013051.

Abstract

We present a revised three-plate kinematic model for the Lau Basin, focusing on new interpretations of the geologic characteristics of the Niuafu'ou microplate boundaries. It builds upon the three-plate model by *Zellmer and Taylor* [2001], while resolving some geologic discrepancies in that model. Along the southern branch of the Mangatolu Triple Junction and the Fonualei Rift and Spreading Center, which together form the Niuafu'ou-Tonga plate boundary, our model predicts slow to ultraslow opening rates (~2-8 mm/yr southward), consistent with axial morphology and magnetic profile modeling. Our interpretation of the seafloor magnetization pattern and flank morphology along the Central Lau Spreading Center (CLSC) indicates that opening rates along the Australia-Niuafu'ou boundary are higher than predicted in the previous model, thus compensating for slower rates along the Niuafu'ou-Tonga boundary. Lastly, we show geologic evidence that Peggy Ridge (PR), interpreted previously as an active transform fault and therefore a strong azimuthal constraint on Niuafu'ou plate motion, is inactive and that the active plate boundary is the adjacent Lau Extensional Transform Zone, extending from the CLSC to its intersection with the Northwest Lau Spreading Center. The removal of the PR azimuthal constraint allows us to determine an Euler pole for Australia-Niuafu'ou opening that satisfies three-plate closure criterion and develop a geologically consistent model of Lau Basin kinematics. While the final model focuses on constraining current plate velocities assuming rigid plate Eulerian rotations, the geologic analyses presented herein also provide insight into long term basin evolution, which appears to involve significant non-rigid plate kinematics.

3.1. Introduction

The Lau Basin is where extensional tectonic development of backarc basins was first proposed [Karig, 1970] and it has remained a focus site for geophysical, geochemical, and geodynamic studies. These studies have attempted to unravel Lau Basin tectonic evolution and constrain models of plate kinematics within the basin. The first quantitative Lau Basin kinematic model was developed by Zellmer and Taylor [2001] (hereafter referred to as “ZT01”). ZT01 compiled all available geophysical and geodetic [Bevis *et al.*, 1995; Bevis, 1997] constraints and associated uncertainties in a self-consistent three-plate kinematic solution, which described the motion of the Tonga, Australia, and intervening Niufo‘ou microplate relative to each other. However, this model predicts high deformation rates (>40 mm/yr) at a southern “diffuse” boundary between the Niufo‘ou and Tonga plates where there is no morphologic or teleseismic earthquake evidence of an active plate boundary. Conder and Wiens [2011], using a local ocean bottom seismometer array, also found little microseismic earthquake evidence for a plate boundary in this area. The lack of even microseismicity in an area with proposed deformation rates in excess of 40 mm/yr was strong motivation to re-examine previous solutions. Conder and Wiens [2011] proposed that the Niufo‘ou-Tonga (N-T) Euler pole actually lies nearly 200 km northeast of the ZT01 location, on the arc platform south of the active Fonualei rift. Although moving the Euler pole northward decreases predicted N-T relative velocities in the diffuse deformation zone, this does not address broader implications for the three-plate kinematic solution. Here we present geologic and geophysical observations and analyses that inform new interpretations regarding the nature of the N-T and Australia-Niufo‘ou (A-N) plate boundaries and the kinematics of the Niufo‘ou microplate, allowing us to develop an improved Lau Basin kinematic model. The final model describes current plate motions consistent with geodetic measurements, but our analysis also provides insight into basin evolution over the Brunhes chron (0.78 My) and beyond. Furthermore, our results illustrate some of the issues and limitations in applying rigid plate kinematics to the evolution of backarc basins, which are often driven by non-rigid deformation and rollback of subducting slabs. We use a combination of available geophysical data sets in the region, including multibeam bathymetry and backscatter, shallow-towed sidescan sonar, seismicity, and magnetics to both describe the morphology and geologic

characteristics of the plate boundaries and calculate spreading rates along the N-T boundary. Further interpretations of these new velocities with respect to the morphology, tectonics, and nature of crustal accretion along the N-T boundary are described in *Sleeper et al.* [2016].

3.2. Tectonic setting and kinematics

3.2.1. Present day tectonics in the Lau Basin

In the Lau Basin, there is a general trend of increasing tectonic complexity from south to north, following overall opening amounts and rates. In the southern basin, the tectonic configuration is a relatively simple two-plate system, where extension between the Australia and Tonga plates is focused along a single segmented axis, consisting of the Eastern Lau Spreading Center (ELSC), and its southern extension, Valu Fa Ridge (VFR) (*Fig. 3.1*). North of the ELSC a third plate had long been proposed [*Weissel, 1977; Pelletier and Louat, 1989; Parson and Tiffin, 1993*], with total extension between Australia and Tonga partitioned between two boundaries. The Central Lau Spreading Center (CLSC), along with the Lau Extensional Transform Zone (LETZ) and Peggy Ridge (PR), were proposed to form the western boundary of the Niufo'ou microplate [*Zellmer and Taylor, 2001*], while the Fonualei Rift and Spreading Center (FRSC), combined with the southern branch of the Mangatolu Triple Junction (MTJ-S), define the boundary along the eastern margin (*Fig. 3.1*). Thus, the intersection of the Australia-Niufo'ou-Tonga plate boundaries nominally comprise a ridge-ridge-ridge triple junction; however, the plate boundary zones do not actually meet at a point. Instead, the A-N boundary is a southward-propagating ridge, the CLSC, offset from and replacing the northern end of the ELSC, the A-T boundary. The CLSC-ELSC offset comprises a tectonized zone of transferred lithosphere with prominent failed and failing segments of the ELSC and active teleseismic deformation [*Wetzel et al., 1993; Conder and Wiens, 2011*]. In contrast, the FRSC, the N-T boundary, is offset from both the CLSC and ELSC, yet the offset area displays no apparent morphologic or seismic evidence of deformation.

North of the MTJ, tectonic complexity increases as multiple poorly-defined microplates [*Conder and Wiens, 2011*] may lie in this ultra-fast opening (>160 mm/yr [*Bevis et al., 1995; Phillips, 2003*]) and seismically active area, and thus neither our model nor the ZT01 model include the northernmost Lau Basin. Along the northern margin subduction transitions to strike-

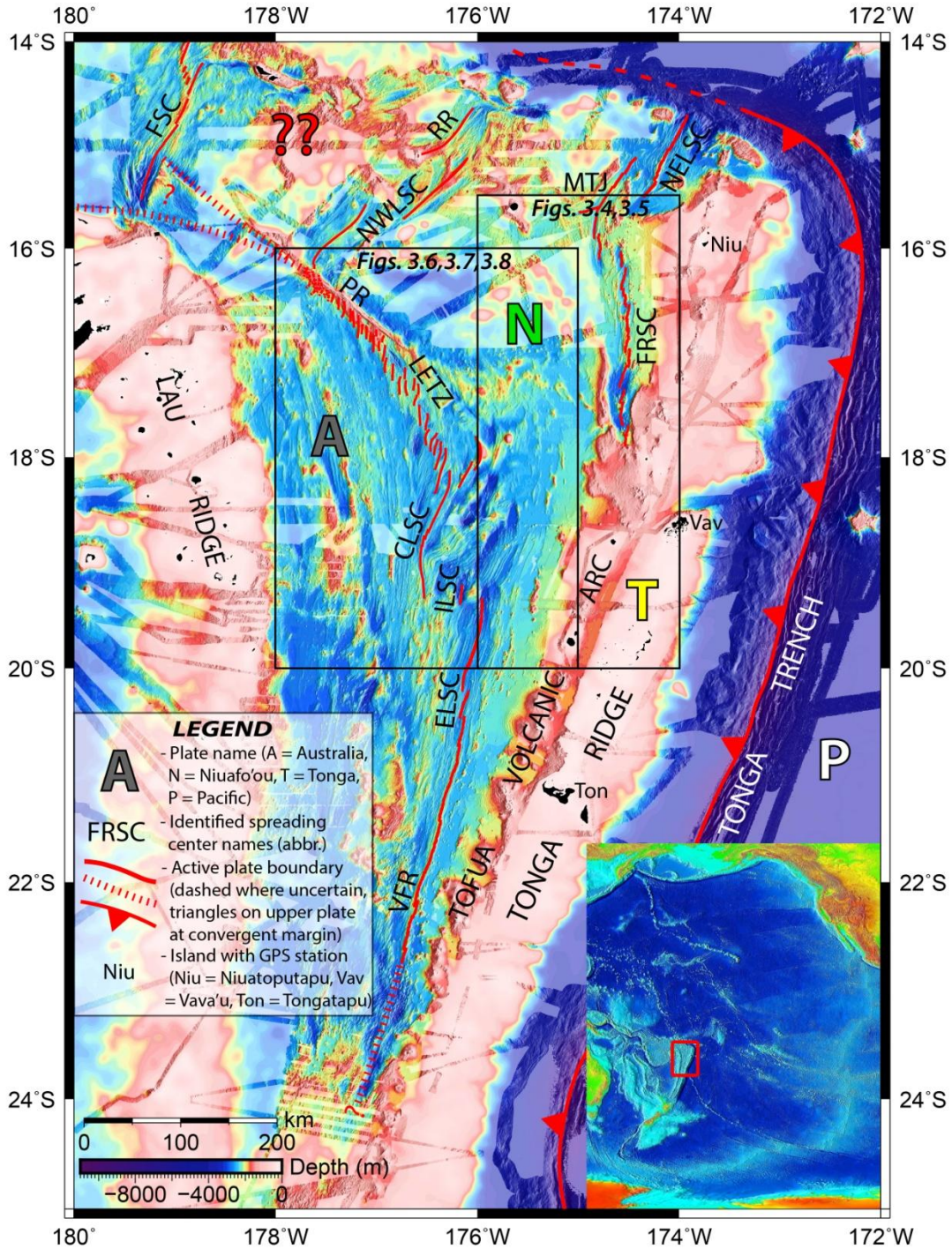


Figure 3.1: Lau Basin bathymetry and location map. Compiled multibeam bathymetry data (0.001° cell size) overlaid on predicted bathymetry from satellite altimeter measurements (reduced opacity) [Smith and Sandwell, 1997]. Bottom right inset shows location in SW Pacific, black boxes show the limits of Figs. 3.4-3.8, see legend for other symbols. Abbreviations: FSC = Futuna Spreading Center, NWLSC = Northwest Lau Spreading Center, RR = Rochambeau Rifts, NELSC = Northeast Lau Spreading Center, MTJ = Mangatolu Triple Junction, FRSC = Fonualei Rift and Spreading Center, PR = Peggy Ridge, LETZ = Lau Extensional Transform Zone, CLSC = Central Lau Spreading Center, ILSC = Intermediate Lau Spreading Center, ELSC = Eastern Lau Spreading Center, VFR = Valu Fa Ridge.

slip motion, accommodated by a tear in the slab near the northeast corner [Millen and Hamburger, 1998; Govers and Wortel, 2005]. The northern basin is incompletely mapped, but a pattern of small microplates is suggested by seismicity [Conder and Wiens, 2011] that are possibly edge-driven [Schouten et al., 1993] by left-lateral shear along the northern margin, in addition to a component of northward extension [Phillips, 2003].

3.2.2. Lau Basin kinematics

The ZT01 three-plate kinematic model for the Lau Basin incorporated geodetic, geologic, and geophysical constraints and developed several self-consistent solutions with associated uncertainties. Here we will primarily refer to “Case 2b” in ZT01, which was the preferred model iteration that satisfied both geodetic and geophysical constraints along with the three-plate closure criterion [McKenzie and Parker, 1967]. The ZT01 three-plate model includes the Australia plate west of the VFR, ELSC, and CLSC, the Tonga plate, lying between the trench and the ELSC/VFR, and the proposed Niufo‘ou microplate, located between the CLSC/LETZ/PR and FRSC/MTJ (Fig. 3.2). Fig. 3.2 shows the ZT01 Case 2b kinematic model, including plate boundaries, predicted velocity small circles, GPS vectors from Bevis [1997] (relative to Australia), and the Australia-Tonga (A-T, yellow star) and N-T (blue star) Euler pole locations (the A-N pole is located north of the map). Constraints on opening rates include picks of the Brunhes-Matuyama magnetic field reversal along the flanks of the ELSC, VFR, CLSC, FRSC, and MTJ-S and geodetic rates from GPS stations on islands within both Tonga and Fiji [Bevis et al., 1995; Bevis, 1997]. Additional azimuthal constraints were derived from the orientation of ridge segments, earthquake slip vectors, and PR (based on the interpretation that it is an active transform fault). Spreading rates and the Euler pole location for the ELSC and VFR in the southern Lau Basin are well constrained due to the abundant data and relatively simple tectonic configuration, where extension is focused along a single linear axis. Predicted full spreading rates along the ELSC/VFR increase from ~39-97 mm/yr northward, and the Euler pole is located south of the axis at 177.7°W/25°S (yellow star in Fig. 3.2). North of the ELSC, extension between Australia and Tonga is partitioned between the CLSC/LETZ/PR to the west and the FRSC/MTJ-S to the east, marking the lateral boundaries of the Niufo‘ou microplate. A spreading rate of ~82 mm/yr was interpreted from a magnetization inversion near the northern end of the CLSC, decreasing northward toward the Euler pole at 170.2°W/8.2°S as predicted

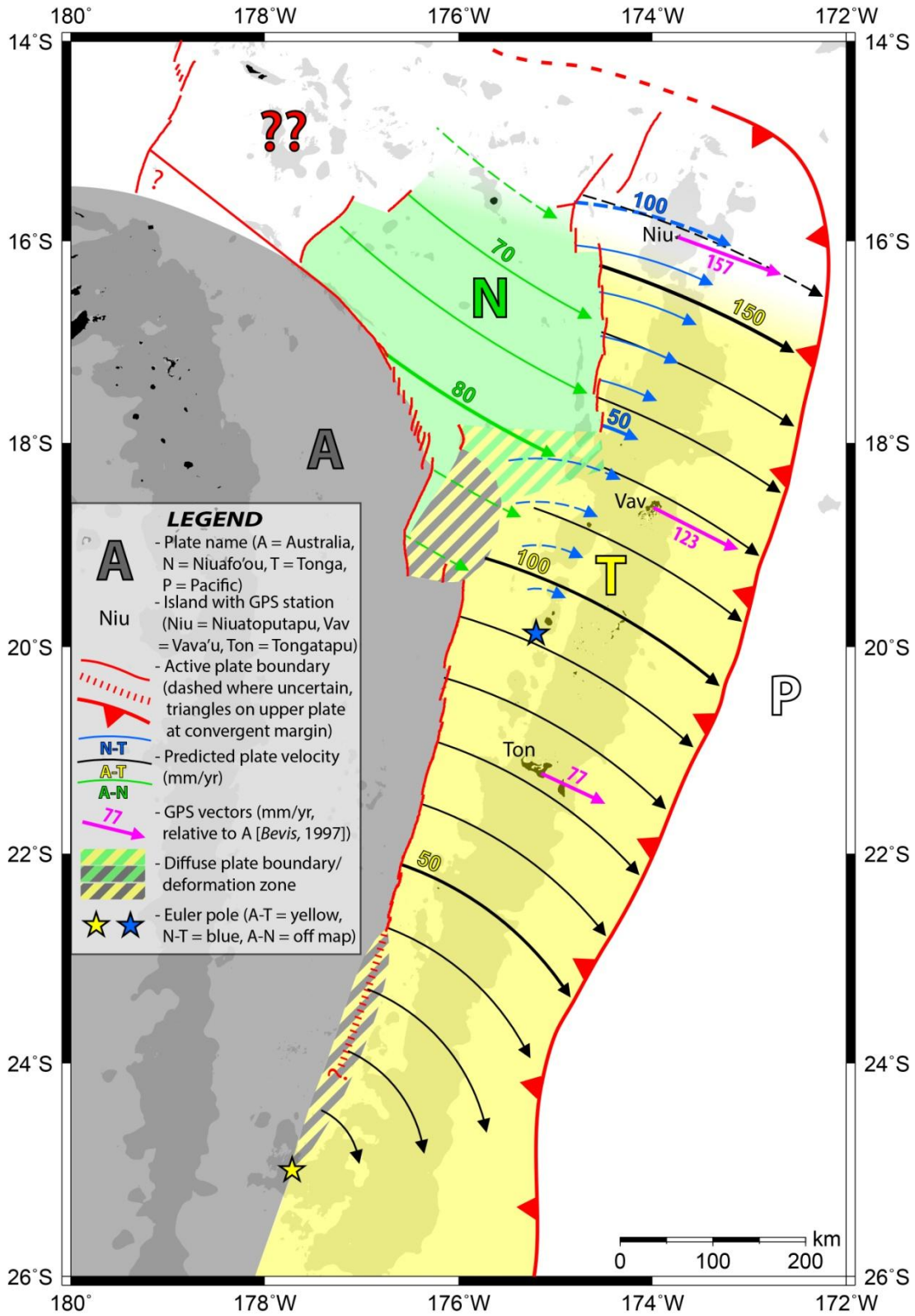


Figure 3.2: Zellmer and Taylor [2001] (abbr. ZT01) three-plate kinematic model, showing the plate configuration, boundaries, and predicted velocities. Gray shading indicates regions shallower than 1500 m. See legend for symbols. Refer to section 3.2.2 for discussion.

rates along the FRSC increase from ~47 mm/yr at the southern tip of the axis to ~94 mm/yr near MTJ. The southern boundary of the Niufo‘ou microplate was interpreted as a diffuse boundary since the mapped spreading centers do not meet as at a formal triple junction. However, based on the ZT01 N-T Euler pole (blue star in *Fig. 3.2*, located at 175.2°W/19.8°S, ~200 km southwest of the spreading axis tip) and the predicted rate of 47 mm/yr at the southern end of the FRSC, opening rates along this proposed diffuse boundary should be ~40 mm/yr, and thus the lack of deformation and seismicity represents a discrepancy that needs to be resolved. Further, the morphology of the FRSC is inconsistent with spreading rates greater than 47 mm/yr [*Sleeper et al.*, 2016], which is comparable to that of VFR, forming a continuous axial high at a similar distance from the arc volcanic front. These and other issues are addressed by our revised three-plate kinematic model that also incorporates new FRSC spreading rates, discussed in section 3.5.1.

3.3. Geophysical data sets and processing

Most of the bathymetry maps presented here were plotted from a basin-wide compiled grid (0.001° cell size), using data available from the National Geophysical Data Center (ngdc.noaa.gov), data obtained from the South Pacific Applied Geoscience Commission [*Goodliffe*, 1995], and additional data from the NoToVe [*Arculus*, 2004] expedition on *R/V Southern Surveyor* and the ALAUF1 cruise on *R/V L’Atalante* [*Pelletier et al.*, 2001]. For the FRSC/MTJ region, multibeam bathymetry data from multiple expeditions (*Fig. 3.3a*) (NoToVE (2004), KM0417 (2004), KM0704 (2007), KM1007 (2010), KM1129A (2011), TN227 (2008), and RR0916 (2009)), along with shallow-towed HMR-1 bathymetry from the MW9603 expedition (1996) [*Taylor et al.*, 1996a], were compiled, ping-edited, and gridded with a cell size of 0.0003° using MB-System [*Caress and Chayes*, 2006] and Generic Mapping Tools (GMT) [*Wessel et al.*, 2013] software. Ship-based magnetic data from multiple cruises between 1968 and 1996, along with data from the 1979 US Naval Research Laboratory South Pacific aeromagnetic survey (*Fig. 3.3b*) [*Cherkis*, 1980] from the National Geophysical Data Center (ngdc.noaa.gov) were compiled to use in the seafloor magnetization inversion. Two aeromagnetic survey lines were selected for two-dimensional (2-D) forward modeling using MODMAG software [*Mendel*, 2005] to constrain FRSC spreading rates (black profiles in *Fig. 3.3b*). A magnetization inversion

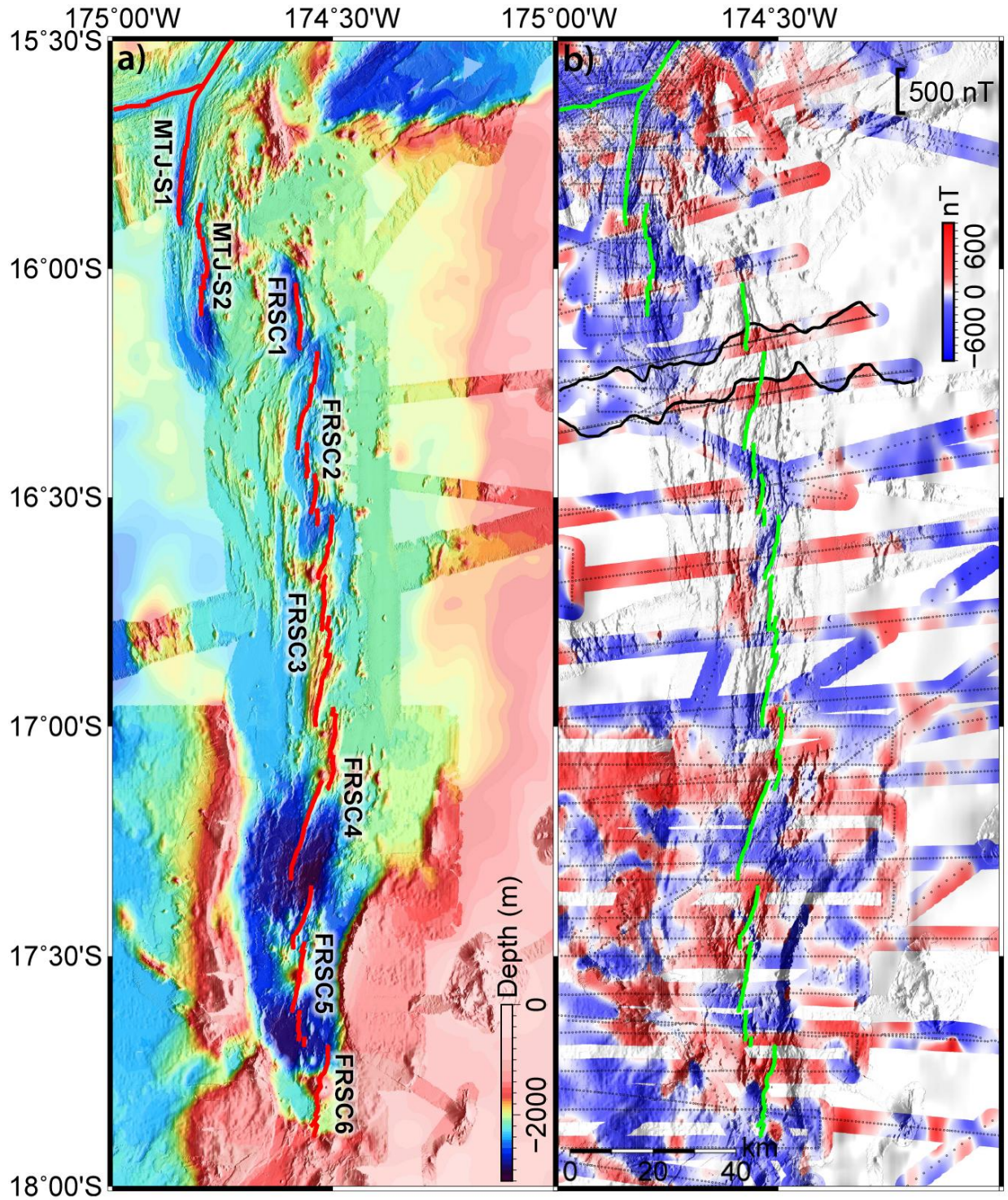


Figure 3.3: Geophysical data along the FRSC/MTJ-S. a) Compiled bathymetry map (0.0003° cell size), gaps in multibeam coverage filled with predicted bathymetry from satellite altimeter measurements (reduced opacity) [Smith and Sandwell, 1997]. The spreading axis is shown in red, and second-order segments are labeled (taken from Sleeper et al., 2016). b) Magnetic anomaly grid from combined aeromagnetic and ship data (up-sampled from 0.5 arc-minute to 0.0003° cell size). Spreading axis shown in green. Profiles used for magnetic modeling are shown as black wiggles. Data points are shown with black dots, regions >3 km from a data point are masked white.

was performed for the FRSC/MTJ region with Mirone software [Luis, 2007], using the bathymetric and magnetic anomaly data in Fig. 3.3, both gridded with a cell size of 0.5 arc-minutes. For the plots in Fig. 3.3 (and the magnetization plot in Fig. 3.5), the magnetic grids were up-sampled to 0.0003° cell size to match the finely gridded bathymetry data also utilized in Sleeper *et al.* [2016] for morphologic descriptions. Backscatter data from hull-mounted multibeam systems, the shallow-towed GLORIA sidescan sonar system [Parson and Tiffin, 1993], and the HMR-1 shallow-towed sidescan sonar [Taylor *et al.*, 1996a] were compiled and gridded at 0.001° cell size. Seismicity data come from two sources: teleseismic events obtained from the Harvard global CMT catalog [Dziewonski *et al.*, 1981; Ekström *et al.*, 2012], restricted to depths above 50 km to isolate upper plate earthquakes, and microseismicity recorded on a local ocean bottom seismometer array in late 1984 [Eguchi *et al.*, 1989]. It should be noted that the Eguchi *et al.* [1989] OBS array only extended to ~17°S, so the lack of events north of that is only due to the OBS coverage and not due to a lack of seismicity, as evidenced by the continued teleseismicity to the north, and microseismicity recorded by Conder and Wiens [2011].

3.4. Plate boundary observations and interpretations

The geologic and geophysical characteristics of the ELSC and VFR (the A-T plate boundary) have been described in detail in previous studies [e.g. Wiedicke and Collier, 1993; Wiedicke and Habler, 1993; Taylor *et al.*, 1996; Peirce *et al.*, 2001; Martinez *et al.*, 2006; Jacobs *et al.*, 2007; Sleeper and Martinez, 2014], and its kinematics are well constrained by geodetic and geophysical data as modeled in ZT01. The primary differences in our model are based on new geologic interpretations of both the N-T and A-N boundaries, which will be described in 3.4.1 and 3.4.2, respectively. For the N-T boundary, we present evidence for slow to ultraslow spreading rates, based on axial and flank morphology along with 2-D modeling along two magnetic profiles across the FRSC axis. For the A-N boundary, we present interpretations of seafloor morphology and magnetization that indicate higher spreading rates along the CLSC, and show that the morphologic PR is no longer active and that the active plate boundary lies to the south along a set of en echelon axial volcanic ridges and Riedel shears linking the NWLSC and CLSC. For the A-T boundary, our new model only requires a minor adjustment in the Euler pole

location and opening rate to account for the most recently updated geodetic data [Phillips, 2003], discussed in detail in 3.4.3.

3.4.1. Niuafu 'ou-Tonga plate boundary: morphologic evidence for slower spreading rates

New geologic and geophysical observations and interpretations of the FRSC and MTJ-S (the N-T boundary) are described separately in *Sleeper et al.* [2016], and we summarize the relevant observations here. Along the FRSC segments, there is an abrupt southward morphologic transition from linear volcanic axes to spaced volcanic cones bisected by rift zones and surrounded by anomalously deep seafloor with relatively thin crust [*Sleeper et al.*, 2016]. This abrupt change is morphologically analogous to that seen at MORs as they transition from slow to ultraslow (<12 mm/yr) spreading rates [*Dick et al.*, 2003]. This suggests similar variations in spreading rate southward along the N-T boundary, although spreading appears to remain magmatic along the FRSC [*Keller et al.*, 2008]. Furthermore, based on the ZT01 model, the southern FRSC segments have similar predicted spreading rates to VFR in the southern Lau basin (~47-60 mm/yr vs. 39-61 mm/yr), and both are at similar distances from the arc volcanic front, yet VFR is a shallow, steep-sided volcanic ridge unlike the southern FRSC. Near the southern end of the Malaguana-Gadao Ridge (MGR) in the southern Mariana Trough, spreading rates are ~45 mm/yr [*Kato et al.*, 2003] and the arc volcanic front is again at a similar distance as the southern FRSC, but axial morphology is characterized by a broad shallow volcanic ridge [*Becker et al.*, 2010] rather than spaced axial volcanic cones surrounded by deep seafloor. The contrasting morphologic and geologic observations indicate that spreading rates along the southern FRSC are significantly slower than VFR or the southern MGR. We use magnetic anomaly profile modeling and a new estimated N-T Euler pole location to further quantify this assessment in the following sub-sections.

3.4.1.1. Niuafu 'ou-Tonga plate boundary: magnetic anomaly modeling and a new Euler pole

A key constraint in the new kinematic model is the opening rate along the N-T boundary, which includes the FRSC and MTJ-S. Here we use 2-D forward modeling of magnetic anomaly profiles along the northern FRSC combined with a revised Euler pole location to constrain and predict opening rates along the N-T boundary. Due to the limited magnetic data and the young age and propagating development of the FRSC, the best-defined magnetic time marker is the

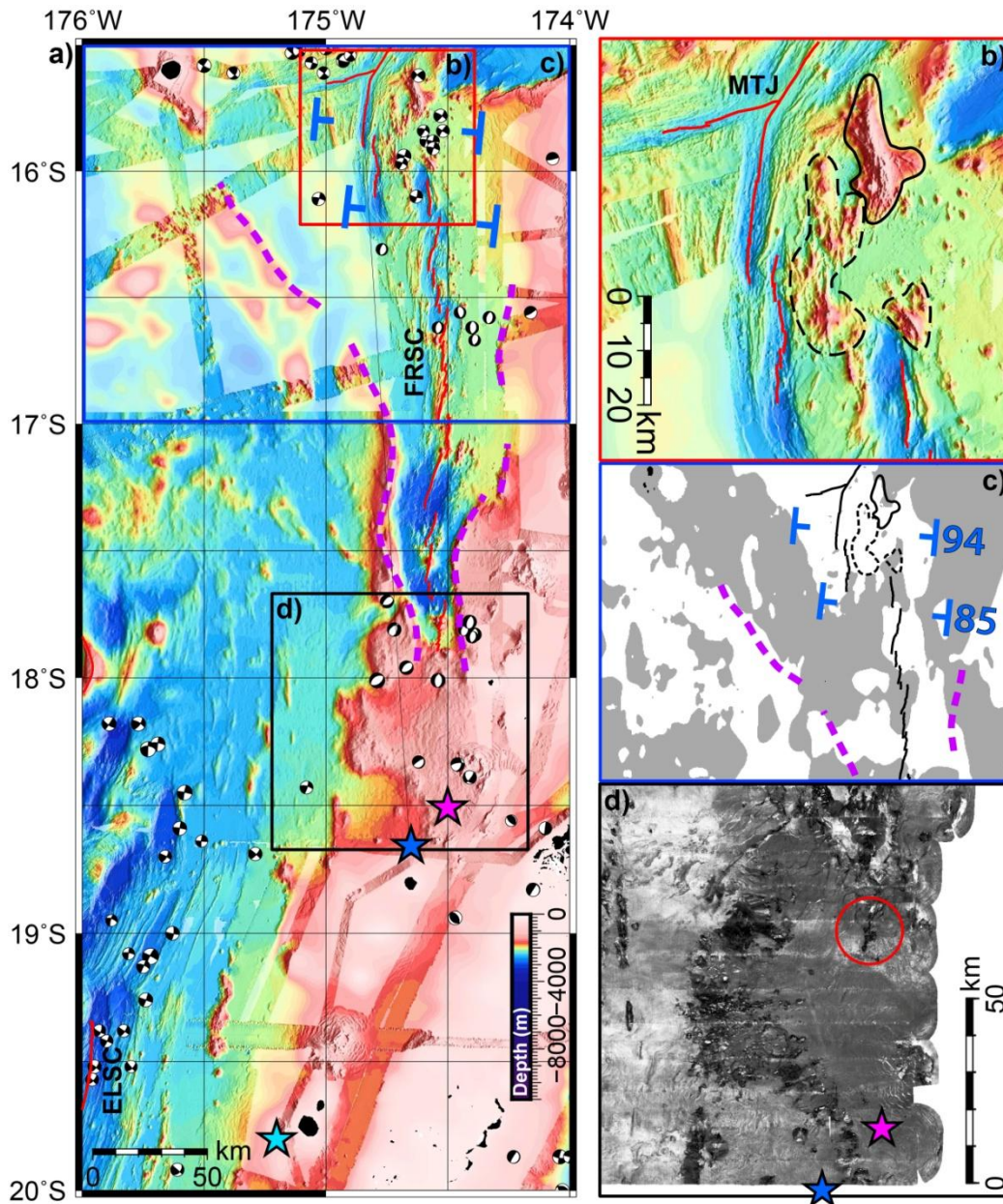


Figure 3.4: Niufo'ou-Tonga (N-T) boundary geology and tectonics. a) Compiled bathymetry map (0.001° cell size), showing the FRSC, MTJ, and the region to the southwest. The three proposed Euler pole locations are marked with stars (light blue = ZT01, magenta = *Conder and Wiens* [2011], dark blue = this study). Rifted margins are marked with dashed magenta lines, the spreading axis is marked with solid red lines, and the locations of magnetic reversal picks in ZT01 are marked in blue. Boxes for Fig. 3.4b,c,d are color coded and labeled. Earthquake focal mechanisms (<50 km depth) from the Harvard CMT catalog [*Dziewonski et al.*, 1981; *Ekström et al.*, 2012] are plotted as "beachballs" with the compressional quadrants colored black. b) Zoomed in bathymetry map of the FRSC/MTJ overlap region to highlight morphology. Volcanic morphology similar to that along the southern FRSC is outlined with dashed black lines, while the ridge outlined in solid black appears to be a block of pre-existing crust. c) Magnetization map from ZT01 with positive shown in white and negative in gray. The picks of the apparent Brunhes boundary are marked in blue, and the measured rates of 94 and 85 mm/yr are shown. d) HMR-1 sidescan sonar image showing the region south of the rift valley. The red circle marks a lava flow that represents the southernmost evidence of volcanic or tectonic activity, and our pole (blue star) is placed well south of this. Refer to section 3.4.1 for discussion.

Brunhes-Matuyama reversal at 0.78 Ma. The magnetic anomalies shown in *Fig. 3.3b* were calculated from the total field data by removing the International Geomagnetic Reference Field using GMT software [Wessel *et al.*, 2013]. Aeromagnetic data were downward-continued from the flight altitude of 330 m [Cherkis, 1980] to the sea surface prior to compiling with the ship data. ZT01 used limited ship bathymetry together with satellite-predicted bathymetry and uneven magnetic profile coverage in this area to calculate a magnetization inversion. Based on the pick of the Brunhes boundary in the magnetization grid, ZT01 determined a spreading rate of 94 mm/yr along the MTJ-S and 85 mm/yr across the northern FRSC segment (blue “T” symbols in *Fig. 3.4c*). Both picks were made across the ~25 km wide overlap zone between the MTJ-S and FRSC (*Fig. 3.4a*). This complicates interpretation of the magnetization pattern because the crust was not necessarily accreted along a single axis, it may be rotated and deformed, and pre-existing and new crust may be trapped in the overlap zone and may be rotated and deformed. Indeed, newer bathymetry data show asymmetric crustal fabric on the eastern flank unlikely to have formed along MTJ-S, indicating that the zone of positive magnetization was not likely continuously accreted within the Brunhes chron. First, there is an abrupt change in morphology a few km east of the axis from ~axis-parallel spreading fabric to a volcanic terrain characterized by elliptical seamounts and volcanic cones similar to those found along the southern FRSC [Sleeper *et al.*, 2016] (dashed black outlines on *Fig. 3.4b,c*). These volcanic features have no counterpart on the western flank, suggesting that this is pre-existing crust formed under different magmatic and tectonic conditions, and thus cannot be explained simply by an axis jump to the west within the Brunhes chron. Also, the anomalously shallow ridge to the northeast (solid black outline in *Fig. 3.4b,c*) does not match MTJ flank morphology, and may be a rotated block of pre-existing crust trapped within the overlap zone. The distribution of teleseismic [Dziewonski *et al.*, 1981; Ekström *et al.*, 2012] strike-slip events east of the MTJ-S and west and north of the FRSC (*Fig. 3.4a*) also suggests a zone of tectonized and possibly transferred lithosphere in the area near the overlapping spreading centers. Thus, even with additional data we do not feel confident in an accurate magnetization inversion in this area and therefore chose to use a 2-D forward modeling approach on carefully selected individual aeromagnetic survey lines rather than picking the Brunhes boundary from a magnetization grid.

3.4.1.2. Model set-up and Euler pole location

We selected two aeromagnetic survey lines that show the clearest presumed Brunhes anomaly roughly centered on the axis (black profiles in *Fig. 3.3b,3.5a*), while avoiding the young southern end of the FRSC and the overlap zone at the northern end. MODMAG software [Mendel, 2005] was used to adjust model parameters, particularly spreading rate, spreading asymmetry, and magnetization intensity, until a reasonable fit was achieved (see 3.4.1.3.). To then calculate overall opening rates on the FRSC, we assume that the opening pole is located south of the Fonualei Rift tip at 174.65°W/18.65°S (dark blue star in *Fig. 3.4a,d*), where tectonic, volcanic, and teleseismic [Dziewonski *et al.*, 1981; Ekström *et al.*, 2012] earthquake evidence of active rifting disappears (*Fig. 3.4a,d*) and the opening rate presumably drops to zero. Conder and Wiens [2011] also suggest that the FRSC pole could be in a similar location (174.5°W/18.5°S, magenta star in *Fig. 3.4a*) based on the distribution of microseismicity and the lack of evidence for continued rifting south of the FRSC morphologic tip. Following Conder and Wiens [2011] we place the N-T pole ~25 km to the southwest to move it well beyond morphologic evidence of deformation and the southernmost teleseismic events (*Fig. 3.4a*). The westward offset relative to the Conder and Wiens [2011] pole location is intended to account for the slightly N-NE trend of the FRSC segments, so that oblique spreading is not required. It is difficult to further constrain this pole location without more magnetic data along the FRSC, but any pole located between ~174.5°-174.75°W and 18.5°-19°S could potentially fit the geologic, geophysical, and geodetic constraints.

3.4.1.3. Magnetic modeling results: slow to ultraslow spreading along the FRSC/MTJ-S

Magnetic modeling results are presented in *Fig. 3.5*, with the seafloor magnetization inversion shown in *3.5a*, and the modeling results in *3.5b* and *3.5c*. The magnetic anomaly profiles shown in black on *Fig. 3.5a* are parts of two aeromagnetic survey lines, while the rest of the combined aeromagnetic and ship data are marked with black dots to show data coverage. The projected profiles (shown in magenta in *Fig. 3.5a*) are the assumed flow lines, drawn orthogonal to a great circle projected from the Euler pole. Regions more than 3 km from a data point are masked white to show data gaps. The gridded magnetization pattern shown in *Fig. 3.5a* is difficult to interpret due to the complex evolution of the FRSC, the variable quality and imperfect agreement between data sets, and interpolation uncertainties created when trying to grid areas with sparse coverage. The interpolation uncertainties, which cannot be resolved

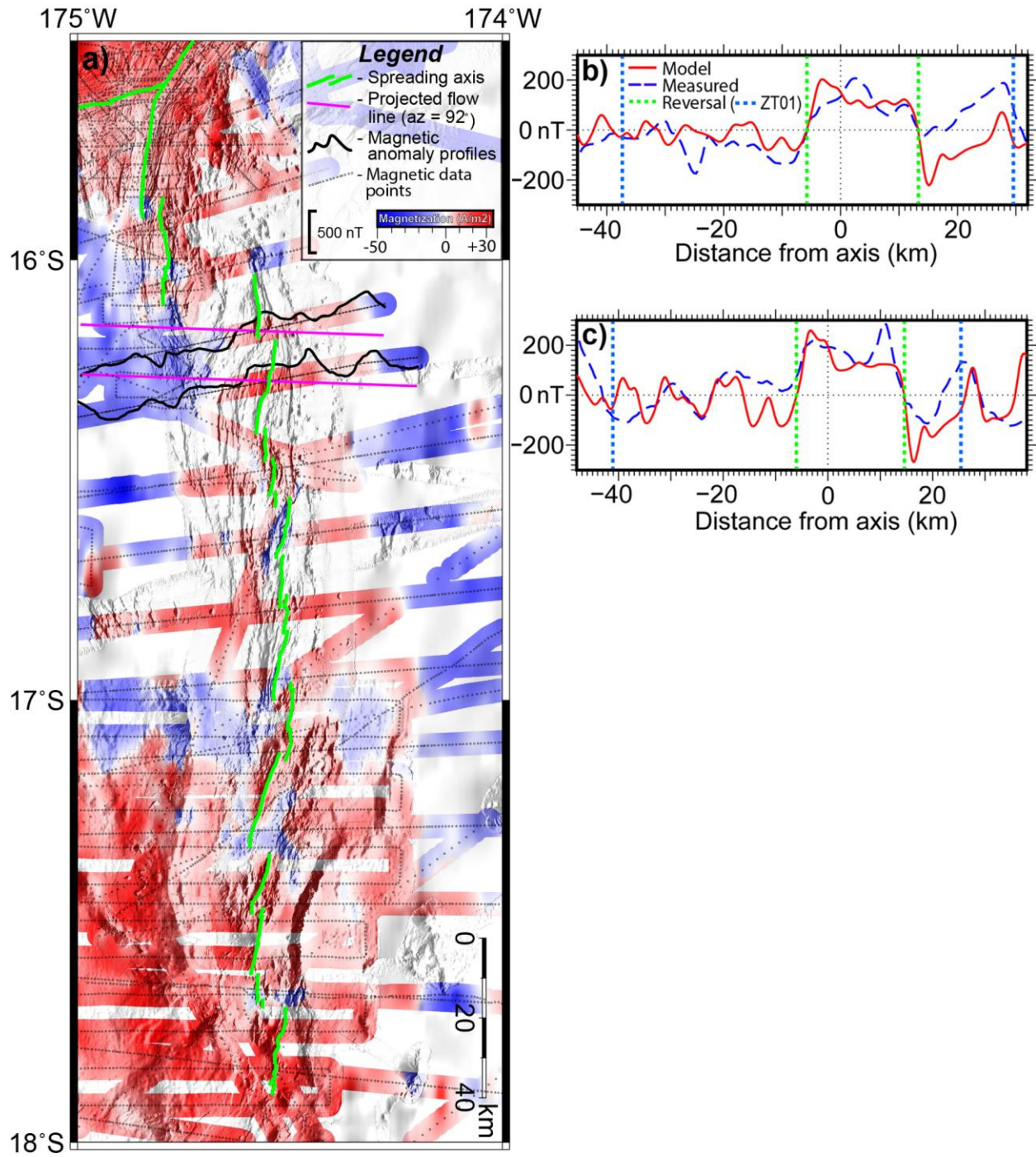


Figure 3.5: Magnetic profile modeling results. a) Seafloor magnetization inversion (grid was up-sampled from 0.5 arc minute to 0.0003° cell size for the above image) using Mirone software [Luis, 2007] shows the complicated pattern and variable apparent width of the Brunhes chron on the axial flanks. Regions >3 km from a data point are masked white. See legend for symbols. b) Results for the northern profile and c) the southern profile, where Brunhes chron spreading rates of 23.6 and 25.5 mm/yr, respectively, were calculated. Refer to section 3.4.1.2 for further discussion.

without additional data, were a primary motivation for choosing the two-dimensional magnetic profile forward modeling approach over a gridded three-dimensional magnetization inversion to determine the width of the Brunhes chron here. Also, there is an inherent ambiguity in the magnetization inversion itself, defined by the magnetic “annihilator”, a magnetization distribution that produces no field at the sea surface [Parker & Huestis, 1974]. Typically a quantity of magnetic annihilator is added to the solution to balance polarities across reversals [Macdonald *et al.*, 1980a]. However, in the case of the FRSC it is not clear that the magnetization pattern results from a continuous spreading history on a single axis as there are large unsystematic variations in the width of the apparent Brunhes anomaly along the axis. Under these conditions the shape of individual total field anomaly profiles, selected to avoid tectonically complex areas, is probably a more reliable indicator of the reversal boundaries than the three-dimensional magnetization inversion.

The primary constraint on the magnetic profile modeling was to match the steep gradients on either side of the axis that we assume represent the Brunhes-Matuyama polarity reversal at 0.78 Ma. For the northern profile, the spreading rate that best fit the anomaly was 23.6 mm/yr (*Fig. 3.5b*), while a slightly faster rate of 25.5 mm/yr fit the southern profile (*Fig. 3.5c*). Given that the aeromagnetic survey was conducted in 1979 using inertial navigation methods with a drift rate of <1 km/hr and an average flight time of 9.5 hrs [Cherkis, 1980], significant navigational errors are likely, and a difference of ~1-2 mm/yr between the two profiles is within the accuracy of the navigation. Based on the average between these two rates and our Euler pole location, predicted rates vary from ~8 mm/yr at the south end of the FRSC to ~30 mm/yr at the MTJ. In *Fig. 3.5b,c* our interpretation of the reversal locations is shown with green dotted vertical lines, while blue dotted lines show approximately where the picks from ZT01 would project along these profiles. Our picks coincide with steep gradients in the magnetic anomaly that we interpret as the edges of the Brunhes. The ZT01 picks require ignoring the steep gradients flanking the axis and include a number of fluctuations and apparent reversals that would have to have occurred within the Brunhes, which are not observed in the magnetic record elsewhere. Some of these fluctuations could be exaggerated by topographic effects, but there are no similarly steep magnetic gradients in the off-axis crust away from our picks. Both profiles were also modeled with spreading asymmetry in order to account for the eastward offset of the Brunhes anomaly relative to the axis. Spreading asymmetry was consistent for both profiles,

varying from 54% to 56% higher half-spreading rates on the east side of the axis for the northern and southern profiles, respectively. The data do not have the resolution to model the mechanism of asymmetry, but it could be accomplished through either westward migration of the axis through asymmetric accretion, discrete westward jumps, or a combination of the two mechanisms. Magnetized layer thickness in the final models was 0.5 km, although 1 km was tested as well. On-axis block magnetization was 15 A/m for the northern profile and 17 A/m for the southern profile, while off-axis block magnetization was 3 A/m for both profiles. While predicted spreading rates may vary slightly from our model given the uncertainty in the Euler pole location, any model that satisfies both the geologic and magnetic constraints will predict ultraslow rates along the southernmost segments of the FRSC.

3.4.2. Central Lau Spreading Center, Lau Extensional Transform Zone, Peggy Ridge, and the nature of the Australia-Niuafu'ou plate boundary

The nature of the A-N plate boundary also has important implications for Lau Basin kinematics. In the ZT01 model, the CLSC constitutes the southern end of the A-N boundary, transitioning northward into the Lau extensional transform zone (LETZ), consisting of left-stepping en echelon axial volcanic ridges (AVRs), and ultimately into an active transform boundary along PR that extends to the NWLSC (*Fig. 3.2*). Opening rates along this boundary decrease from ~92 mm/yr at the southern end of the CLSC to ~78 mm/yr near the NWLSC at the north end of the boundary (*Fig. 3.2*). These rates are based on a pick of an apparent Brunhes-Matuyama reversal on the CLSC flanks near the LETZ, decreasing northward toward the Euler pole at 170.2°W/8.2°S.

Slower N-T opening rates based on our analysis require a commensurate increase along the A-N boundary in order to maintain total A-T opening rates. From an analysis of the morphology and seafloor magnetization on the CLSC flanks, there are two sources of additional opening that are not accounted for in the ZT01 model. The first is magmatic and tectonic extension along dying segments of the adjacent ELSC as the CLSC propagated southward during the Brunhes. The second source of additional opening is tectonic extension within the zone of transferred lithosphere between the dying segments of the ELSC and CLSC, exhibited as teleseismic bookshelf faulting [*Wetzel et al., 1993*], and mapped rotation of crustal blocks [*Martinez and Taylor, 2006*].

For the oblique northwestern portion of the A-N boundary along the LETZ and PR, opening rates cannot be precisely constrained due to the complex continual evolution of this boundary and the combination of both active extension and strike-slip motion. However, we present evidence from seafloor morphology and seismicity showing that PR is not an active transform fault and that the active plate boundary lies to the south where extension is accommodated magmatically along the LETZ AVR. There is also a component of right-lateral transform motion along this boundary, accommodated along short-lived strike-slip structures that we interpret as Riedel shears [Riedel, 1929; Hills, 1963; Taylor *et al.*, 1994]. The evidence for our interpretation of the A-N boundary is detailed in the following sub-sections.

3.4.2.1. Central Lau Spreading Center morphology

The southern end of the CLSC lies across a ~50 km left-lateral non-transform offset with the northern end of the ELSC, and the intervening Intermediate Lau Spreading Center (ILSC) acts as a short relay segment (*Fig. 3.6a*). High backscatter within the ILSC indicates active volcanism and suggests it remains an active plate boundary. CLSC axial morphology is characterized by a broad rounded volcanic axial high with up to ~600 m of relief, similar to a typical fast-spreading mid-ocean ridge. The CLSC is >150 km from the Tofua arc, and therefore the axial high morphology is largely the result of plate-driven upwelling and melting and not enhanced by high water contents [Pearce *et al.*, 1995] as at the arc-proximal ELSC and VFR. Third-order axial segmentation is defined by subtle left-stepping offsets of a narrow volcanic ridge at the crest of the axial high, primarily associated with the bend in the axis between ~18°40'-50'S (*Fig. 3.6a*). Abyssal hill-type seafloor fabric can be observed on the western flank of the CLSC (*Fig. 3.6a*), consistent with the interpretation of this feature as an oceanic spreading center similar to a mid-ocean ridge [Parson *et al.*, 1990], albeit with strongly asymmetric crustal accretion.

The CLSC is propagating southward, shutting down the adjacent ELSC as it progresses [Parson *et al.*, 1990]. This interpretation is supported morphologically by the southward-narrowing zone of abyssal hill fabric on the western flank and the southward-converging pseudofaults (dashed magenta lines in *Fig. 3.6a*). The overlap region off the eastern flank of the CLSC is a zone of crustal block rotation and complex deformation that has been interpreted as an example of active bookshelf faulting based on the teleseismic strike-slip events there [Wetzel *et*

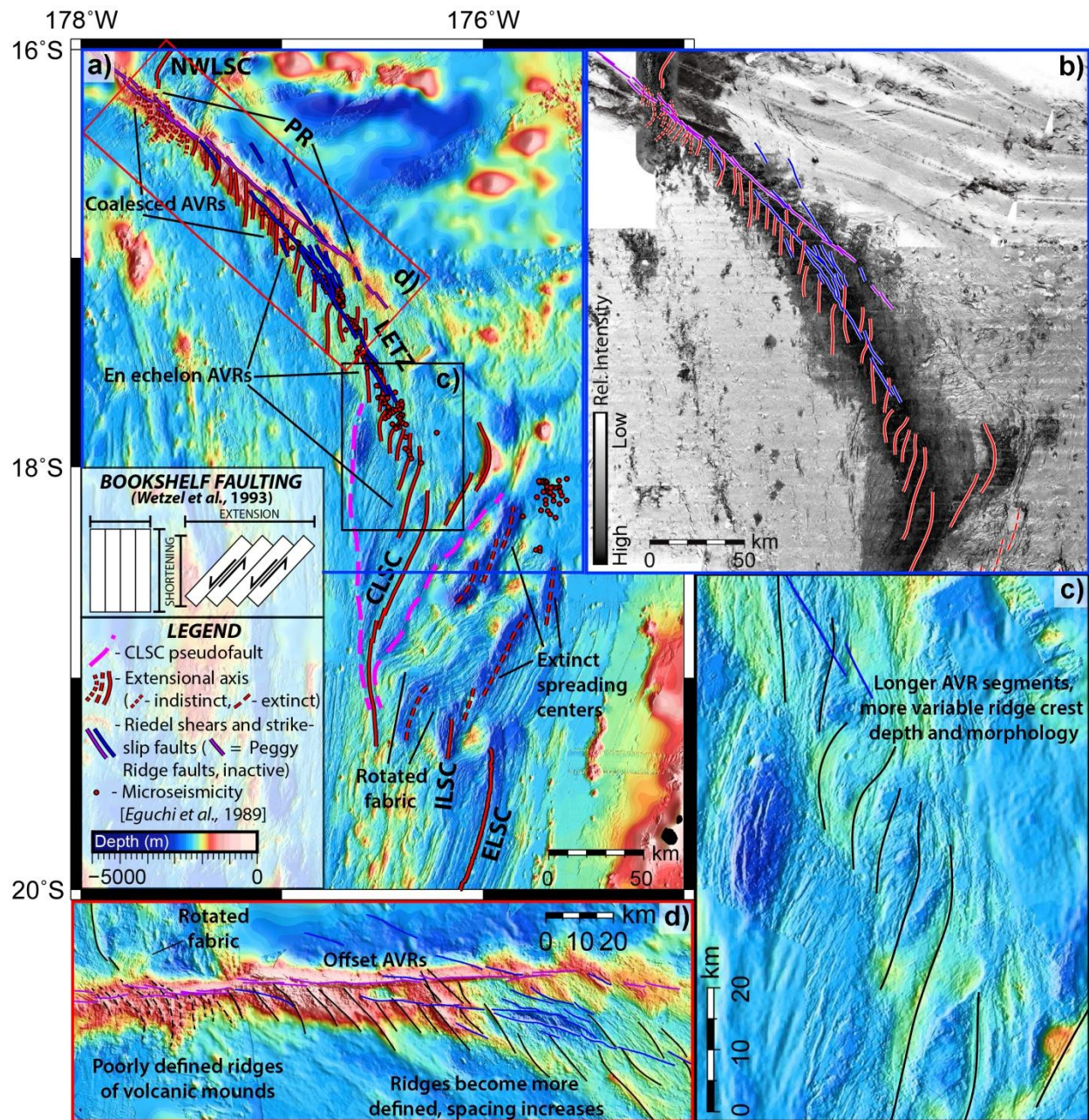


Figure 3.6: Geology of the A-N boundary. a) Compiled bathymetry (0.001° cell size) map showing the central Lau Basin. Abbreviations are the same as Fig. 3.1. Color-coded boxes show detail regions b), c), and d). b) HMR-1 shallow-towed sidescan sonar image (0.001° cell size) from the MW9603 cruise [Taylor et al., 1996a] overlaid on GLORIA sidescan data [Parson and Tiffin, 1993] to fill in the northern portion. Imagery shows zone of high backscatter concentrated along the axial volcanic ridges (AVRs) and volcanic mounds, narrowing toward the NW. c) Typical en echelon AVR morphology along the SE part of the LETZ. d) Morphology of the NE part of the LETZ and PR, showing transition from well-defined AVRs to poorly-defined ridges of coalesced volcanic mounds. Refer to section 3.4.2 for discussion.

al., 1993]. This zone is a complex mixture of newly-formed CLSC crust, older deformed and rotated pre-Brunhes crust formed along the ELSC, and some more recent crust formed during the Brunhes along now-extinct northern segments of the ELSC [Taylor *et al.*, 1996].

3.4.2.2. Central Lau Spreading Center opening rates

ZT01 measured a spreading rate of 82 mm/yr near the overlap with the CLSC and LETZ (blue "T" symbols in *Fig. 3.7*), based on the width of the zone of positively magnetized crust on the CLSC flanks. The change in polarity on either flank of the CLSC was interpreted as the Brunhes-Matuyama reversal recorded in crust accreted along the CLSC. The fact that the pick was again made across overlapping segments introduces some uncertainty in the measurement, but there is also evidence suggesting that this may not represent a full Brunhes chron, and thus the spreading rate may be faster. *Fig. 3.7* presents our interpretation of the magnetization pattern, largely following that of Taylor *et al.* [1996], but refined with additional bathymetric coverage. There is a triangular zone of positively magnetized crust on the CLSC flanks (green zones in *Fig. 3.7*), with slivers of negatively magnetized crust (colored gray in *Fig. 3.7*) on either side that appear to mark the magnetic reversal associated with the beginning of the Brunhes chron (labeled "B" in *Fig. 3.7*). However, the negative slivers coincide with bathymetric deeps, suggesting that they were formed by crustal stretching and tectonization at what was then near the tip of the propagating CLSC, and may not be new crust accreted along the CLSC. This observation raises the possibility that the apparent reversal may simply be a boundary between tectonized older crust and new CLSC crust formed within the Brunhes chron. If this is the case, it implies that CLSC propagation occurred entirely within the Brunhes and thus spreading rates along the CLSC are faster than 82 mm/yr.

Even if the polarity change on the CLSC flanks is indeed the Brunhes-Matuyama reversal, an additional source of A-N opening not accounted for in the ZT01 model is extension and crustal accretion along dying segments of the northern ELSC as it propagated southward. These segments lie within bathymetric deeps (black dashed lines in *Figs. 3.6, 3.7*), and may represent a migrating extensional relay zone [Kleinrock *et al.*, 1989] between the dying northern ELSC segments and the CLSC as it propagated southward. Patches of positively magnetized crust (colored green in *Fig. 3.7*) surrounding the northernmost segments adjacent to the ZT01 magnetic reversal pick could account for an additional ~20-30 mm/yr or more of opening during

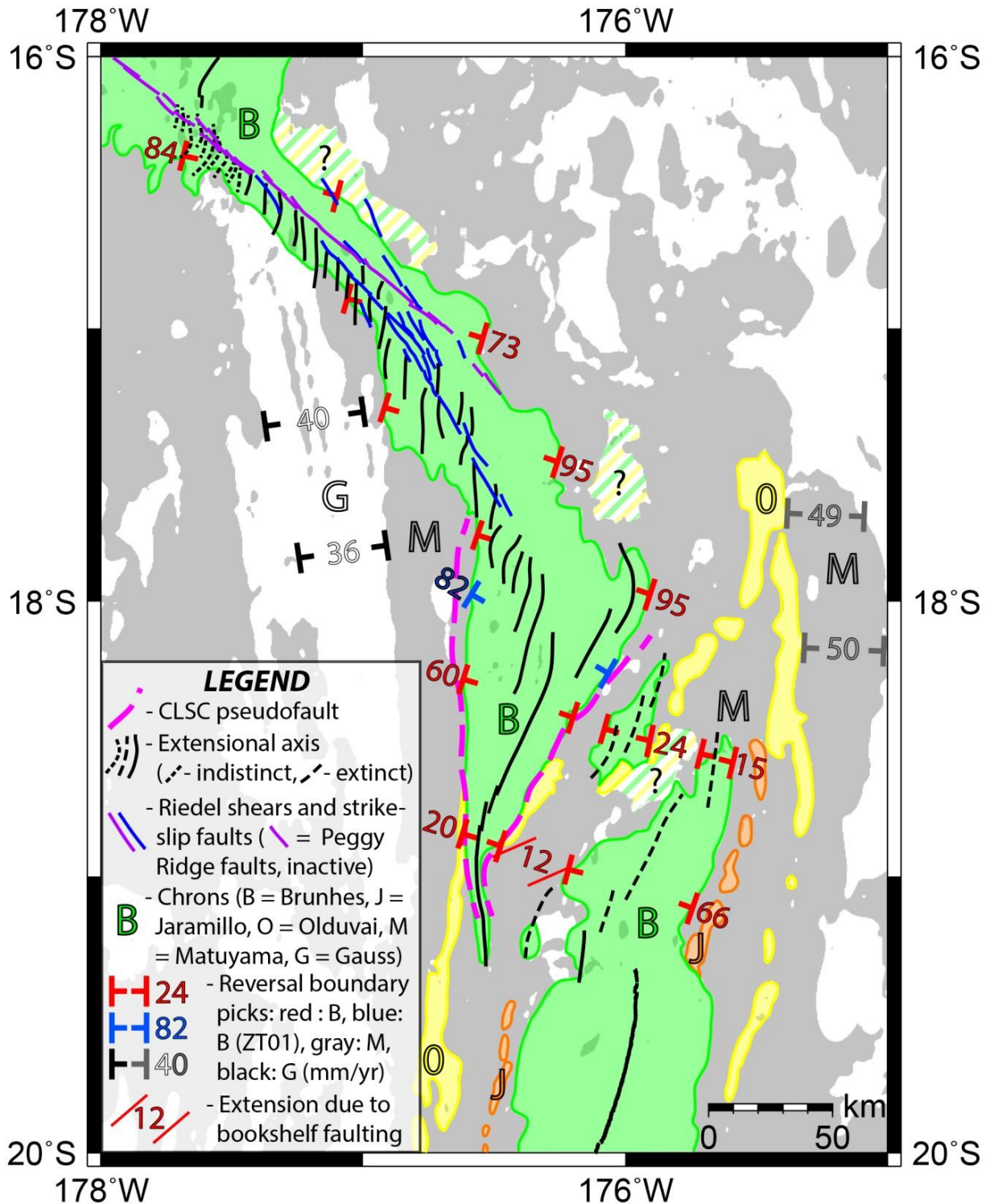


Figure 3.7: A-N boundary magnetic interpretation. a) Compiled magnetization grid from ZT01 (0.002° cell size). Negatively magnetized seafloor is shown in gray, positive in white. Colored zones are labeled as follows: B (green) = Brunhes normal chron, O (yellow) = Olduvai normal sub-chron (within Matuyama reversed chron), J (orange) = Jaramillo normal sub-chron (also within Matuyama reversed chron). The blue "T" symbols labeled "82" show the ZT01 Brunhes pick on which CLSC spreading rates were based. See legend for other symbols. Refer to section 3.4.2 for further discussion.

the Brunhes (a few spot measurements are shown with red “T” symbols on *Fig. 3.7*). Another large zone of positive magnetization extends north of the ELSC, encompassing both the ILSC and three of the extinct segments (*Fig. 3.7*), indicating that these segments were also active for some time during the Brunhes [*Taylor et al.*, 1996]. Quantifying the additional extension on these segments from the magnetic data is, however, complicated by effects of crustal rotations on the magnetization inversion [*Perram et al.*, 1993] within the zone of transferred lithosphere between the CLSC and the extinct segments [*Wetzel et al.*, 1993] (*Fig. 3.7*). Additionally, these dying spreading centers likely continue to accommodate extension tectonically outside of the putative Brunhes crust as indicated by continuing teleseismicity and microseismicity [*Conder and Wiens*, 2011] within areas of low acoustic backscatter, allowing for even higher rates than implied by the width of positively magnetized crust.

Along with tectonic and magmatic extension along the dying northern ELSC segments, additional extension can be accommodated through rotation and bookshelf faulting in pre-existing blocks of transferred lithosphere in the overlap zone between the CLSC and ELSC. This is difficult to quantify precisely, but can be approximated by a simple geometric calculation based on the change in angle from the original orientation, inferred from the fabric off the western flank of the CLSC. As the fabric rotates through left-lateral slip on the bookshelf faults, the originally rectangular piece of crust becomes a parallelogram with a larger overall width (see schematic diagram on *Fig. 3.6a*), accommodating an increasing amount of extension as the rotation angle increases, as well as a small component of shortening in the orthogonal direction. The zone of rotated fabric is labeled on *Fig. 3.6a*, and in *Fig. 3.7* we show an example estimated rate of 12 mm/yr near the southern end of the CLSC. The estimated rate represents an average over the Brunhes, although it was almost certainly active for only a short period of time. The majority of the crust lying between the propagating CLSC and dying ELSC was likely deformed in a similar manner, although highly variable rotation angles indicate that extension varies along strike from a few mm/yr up to perhaps 15 mm/yr where rotation is greatest. The extension is probably accommodated in different ways, giving rise to the varying rotation. Some may be accommodated by continuing rifting at the extinct and dying ELSC spreading centers. Additional extension may be accommodated by bookshelf faulting and crustal rotation in the migrating extensional relay zone [*Kleinrock et al.*, 1989]. The combination of these extensional mechanisms is complementary to that on the CLSC such that the total varies between A-N and

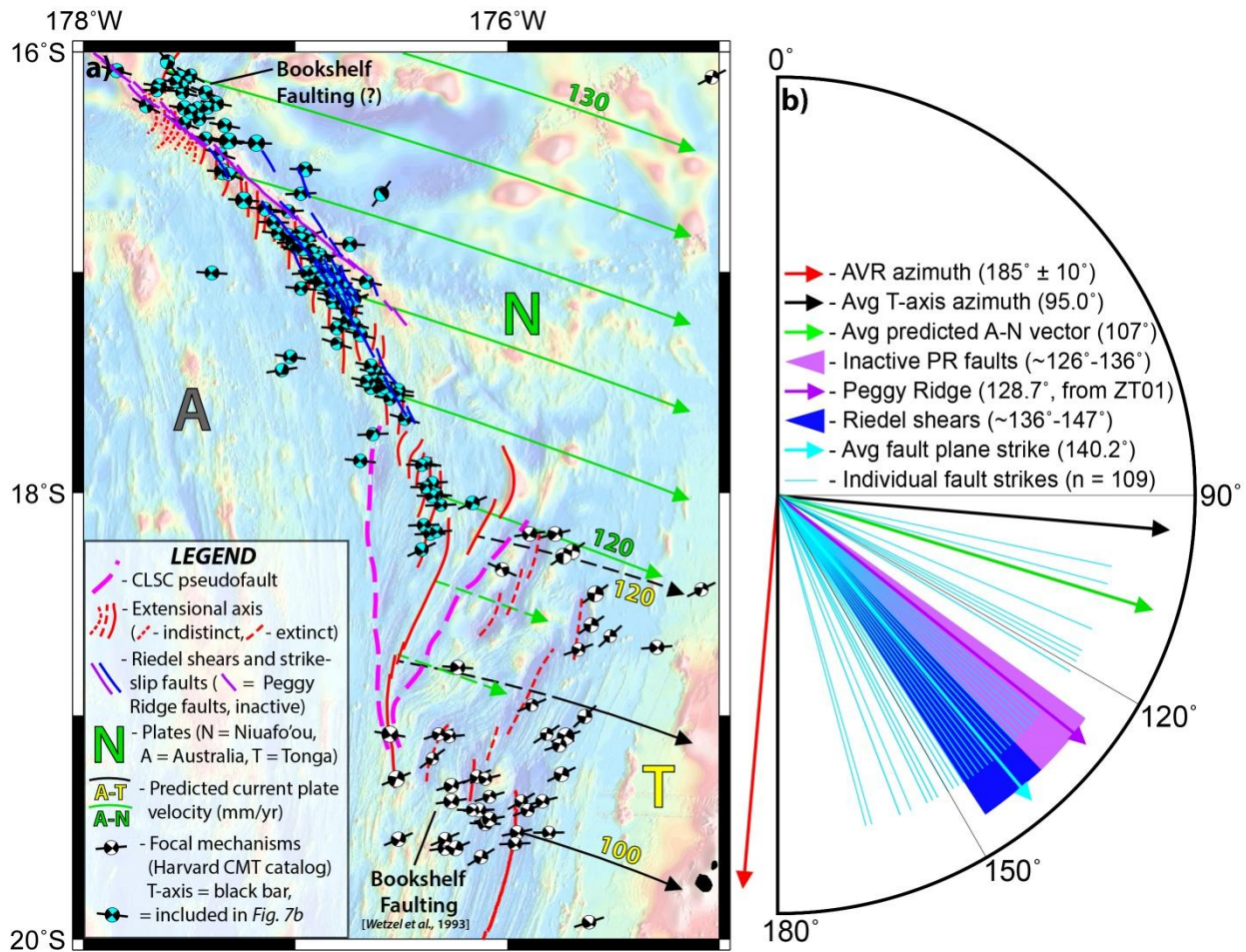


Figure 3.8: A-N boundary tectonics. a) Compiled bathymetry map from Fig. 3.7a with reduced opacity for clarity. See legend for symbols. b) Rose diagram summarizing azimuthal information for the A-N boundary. See figure for color-coding of arrows. Refer to section 3.4.2 for discussion.

A-T extension. Since this additional extension is not accounted for in the ZT01 model, this indicates that the A-N opening rate must be higher than ZT01 predictions.

3.4.2.3. Lau Extensional Transform Zone: extensional structures

The LETZ has been interpreted as an "extensional transform zone" [Taylor et al., 1994], consisting of a series of left-stepping overlapping AVRs and Riedel shears [Riedel, 1929; Hills, 1963] in a NW-trending band linking the CLSC and PR. Extensional transform zones are associated with oblique plate boundaries and accommodate both extensional and strike-slip motion. In the ZT01 model, the LETZ merges with PR toward the NW, and PR is an active transform fault providing a strong azimuthal constraint on Niufo'ou plate motion. Earthquake focal mechanisms (Fig. 3.8a) indicate that this region accommodates significant right-lateral

shear, but the volcanic morphology of the AVRs (*Fig. 3.6c*) and high acoustic backscatter (*Fig. 3.6b*) indicate that they are magmatic extensional features rather than purely tectonic shear structures [Parson *et al.*, 1990]. *Fig. 3.6* presents geologic mapping along the A-N boundary between the CLSC and NWLSC. In general, the character of the AVRs changes toward the NW; they become shorter, shallower, more closely spaced, and less well-defined until they form a coalesced pile of volcanic mounds with poorly-defined ridge-like lineations near the southern termination of the NWLSC (*Fig. 3.6d*). AVR length decreases toward the NW from ~20-30 km, and up to ~50 km along the AVR adjacent to the CLSC, to ~10-15 km south of the NWLSC. Spacing is variable, but generally decreases from ~3-5 km near the CLSC to ~1-2 km south of the NWLSC. Close to the CLSC, AVR crests range in depth from ~2000-2500 m, and morphology varies from a shallow, broad, smooth-flanked volcanic ridge similar to the CLSC to a deeper, narrower ridge within deep tectonized seafloor (*Fig. 3.6c*). The AVRs begin to coalesce north of ~17°S, and there is an abrupt decrease in depth from ~1800 m to ~1000 m (*Fig. 3.6d*). The crests of the poorly-defined AVRs south of the NWLSC reach depths shallower than 500 m in places, and average depths of the coalesced AVRs are shallower than 1000 m. The coalesced AVRs north of ~17°S also have a more hummocky volcanic texture than those to the SE, consisting of volcanic mounds and domes on the order of a few 100 m to ~1 km in diameter (*Fig. 3.6d*).

Individual AVRs trend $\sim 185^\circ \pm 10^\circ$, with the uncertainty reflecting the difficulty in estimating a truly representative azimuth for short curvilinear segments such as these. The ~N-S strike of the AVRs indicates an ~E-W opening direction more consistent with our model predictions (small circles are shown with green arrows in *Fig. 3.8a*) rather than NW-SE, as expected if A-N motion was parallel to PR. Earthquake tension axes (black bars extending from compressional quadrants in the focal mechanism "beachballs" in *Fig. 3.8a*) were calculated from CMT focal mechanisms [Dziewonski *et al.*, 1981; Ekström *et al.*, 2012] in order to estimate the orientation of the extensional component of motion along this boundary. The average T-axis orientation of 95° (black arrow in *Fig. 3.8b*) was calculated using only the events along the LETZ (marked with light blue quadrants on the beachballs in *Fig. 3.8a*), and is orthogonal to the average AVR orientation (red arrow in *Fig. 3.8b*). Since the T-axis orientation reflects the regional stress field and should be aligned with the direction of maximum extensional stress (i.e. σ_3), pure extensional structures should in turn be orthogonal to the T-axes, which is exactly what

is observed. The important observation here is that the entire boundary from the CLSC to the NWLSC shows evidence of recent volcanism and extensional features. Active volcanism and extension along the entire boundary is not consistent with PR being a transform fault [Sclater *et al.*, 1972], which are typically amagmatic features. The zone of positive magnetization along PR and the LETZ (Fig. 3.7), which approximately correlates with the zone of high backscatter (Fig. 3.6b) also indicates significant crustal accretion. If any part of this boundary were purely strike-slip during the Brunhes chron, then the positively magnetized crust would taper to zero width and be truncated and offset along the strike-slip segment. Furthermore, there is a conspicuous lack of teleseismicity (Fig. 3.8a) [Dziewonski *et al.*, 1981; Ekström *et al.*, 2012] and microseismicity (Fig. 3.7a) [Eguchi *et al.*, 1989] along the faults parallel to PR (shown with purple lines on Figs. 3.6-3.8), suggesting that even if it was a transform fault in the past, it is no longer active. Conder and Wiens [2011] showed microseismicity extending north of the Eguchi *et al.* [1989] data set, mostly overlapping the cluster of teleseismicity east of the southern tip of the NWLSC. But within the Eguchi *et al.* [1989] survey area, the microseismicity is concentrated south of the ridge that defines PR on the blue faults in Fig. 3.6, whereas the faults along PR (mapped in purple) appear to be inactive. The interpretation that the faults along PR north of 17°S are inactive is based on the fact that the fault planes in the CMT focal mechanisms do not align with the mapped PR faults but instead are more consistent with Riedel shear trends, which is elaborated upon in the following sub-section. In terms of the consequences for Lau Basin kinematics, if PR is not an active transform fault then it cannot be used as an azimuthal constraint on A-N motion. Thus, not only are opening rates likely to be higher along the A-N boundary, but the vector of Niuafou'ou motion is no longer constrained to be parallel to PR.

3.4.2.4. Lau Extensional Transform Zone: Strike-slip structures

Despite evidence that PR is not an active transform fault and abundant extensional volcanism along the LETZ AVRs, there is a component of right-lateral shear along this oblique plate boundary that is not associated directly with the extensional structures. This is evidenced by teleseismic strike-slip focal mechanisms [Dziewonski *et al.*, 1981; Ekström *et al.*, 2012] (Fig. 3.8a) and linear fault scarps visible along the LETZ that we interpret as Riedel shear structures (blue lines in Fig. 3.6a,d), following Taylor *et al.* [1994]. The azimuthal information for LETZ structures is summarized in a rose diagram in Fig. 3.8b, which includes fault plane strikes (only

those along the LETZ, marked with light blue extensional quadrants in *Fig. 3.8a*), Riedel shear orientations, the PR azimuth from ZT01, the orientation of PR-parallel faults, the average T-axis orientation, and the average predicted A-N motion vector. In terms of Riedel shear theory, the mapped structures (blue lines in *Figs. 3.6,3.7,3.8*) are interpreted as R shears, which form at an approximate angle of $45^\circ - \phi/2$ relative to the direction of plate motion or overall sense of shear (where ϕ is the angle of internal friction) [*Riedel, 1929; Ahlgren, 1999*]. Using the angle of internal friction for basalt of 30° , R shears should form at $\sim 30^\circ$ to the overall sense of A-N motion (green arrows in *Fig. 3.8a,b*), with of course some variability given that it is an evolving natural system. Based on averaging the azimuth of A-N motion at the southern tip of the NWLSC and the northern end of the CLSC, the average predicted azimuth is 107° (*Fig. 3.8b*). The mapped Riedel shears have azimuths of 136° - 147° , at an angle of 29° - 40° relative to A-N motion, in reasonable agreement with the expected orientation. Mapped active Riedel shear azimuths are also comparable to the average fault plane azimuth of 140.2° calculated from the focal mechanisms, and both teleseismicity [*Dziewonski et al., 1981; Ekström et al., 2012*] (*Fig. 3.8a*) and microseismicity (*Fig. 3.6a*) [*Eguchi et al., 1989*] are concentrated along these structures. This indicates that the R shears are the primary structures accommodating the component of right-lateral shear along this boundary. However, the clustering of seismicity near the R shear overlap zones suggests that some slip may be accommodated on unmapped antithetic auxiliary structures linking the R shears, such as R' shears, which form at $\sim 60^\circ$ ($45^\circ + \phi/2$) to the overall sense of plate motion [*Hills, 1963; Ahlgren, 1999*]. The purple faults in *Figs. 3.6,3.7,3.8* are oriented parallel to the morphologic PR and are interpreted to be inactive based on the lack of teleseismic events coinciding with their mapped traces, and the mismatch with the average fault plane strike. Given the uncertainty in the location of the teleseismic events, it is possible that some of these faults segments are still active, but it is clear from the distribution of seismicity that the band of faults to the SE (mapped in blue) are the primary active strikes-slip structures. The Riedel shears cross-cut the AVRs in places but do not form a through-going fault system; instead they cut across a few AVRs before terminating (*Fig. 3.6d*), and in some locations the AVRs are continuous across the R shears. Thus the assembly of AVRs and Riedel shears are individually likely ephemeral features that comprise this evolving oblique plate boundary zone.

One of the remaining conundrums is the cluster of teleseismicity NE of PR on the eastern flank of the NWLSC (*Fig. 3.8a*). The crustal fabric appears to be rotated, similar to the fabric on

the eastern flank of the CLSC, but there are no through-going structures along which seismicity is concentrated. The scattered pattern of seismicity and rotated seafloor fabric are consistent with bookshelf faulting, suggesting that deformation in this region may be similar to the eastern flank of the CLSC [Wetzel *et al.*, 1993]. However, this interpretation is speculative at best, given that the seismicity and apparent crustal rotation is not associated with overlapping spreading centers as on the CLSC flank. Alternatively, it may simply be a zone of diffuse deformation accommodating the transition between the highly oblique LETZ and the southern end of the more orthogonal NWLSC along faults that are too small to resolve in the data.

3.4.3. Australia-Tonga plate boundary: evidence for increasing opening rates over time

The final modification to the ZT01 model involves a slight adjustment to the A-T Euler pole location and predicted opening rates to account for systematic differences between the most recent GPS solutions [Phillips, 2003] and predicted rates based on magnetic data alone. In ZT01, the “Case 2b” model iteration includes both geophysical and geodetic constraints and the predicted rates are as shown in *Fig. 3.2*. “Case 1b” was a model iteration that only included geophysical constraints, and picks of the Brunhes-Matuyama polarity reversal on the ELSC and VFR flanks were the primary constraint on spreading rates. Comparing the geodetic and predicted rates in *Fig. 3.2*, the Tongatapu and Vava’u station rates are ~5 mm/yr faster than predicted velocities, while the Niuatoputapu rate matches the predicted velocity to within ~1 mm/yr. Given the small and inconsistent mismatch between geodetic and magnetically-based opening rates, the conclusion in ZT01 that they are in agreement and the choice of the preferred model iteration using both constraints is justified given the available data at the time. However, using updated geodetic rates in Phillips [2003], this mismatch increases to ~6-8 mm/yr at all three stations. Since the magnetically-based rates represent an average opening rate over the entire Brunhes while the GPS data only measures current motion, the simplest interpretation for the consistently faster GPS rates is that opening rates have increased since the beginning of the Brunhes. Increasing opening rates over time are consistent in a broad sense with the evolution of the Lau Basin from an early phase of diffuse slow spreading similar to what is currently observed in the Havre Trough to the south, to the more rapid recent opening with rates increasing from ~39 mm/yr to over 160 mm/yr from south to north. Taylor *et al.* [1996] also suggested based on the mismatch between geodetic and Brunhes chron spreading rates that opening rates have

increased along the ELSC and CLSC. A simple test to show that rates must be increasing is to look at the overall width of the basin at locations where current geodetic opening rates are known. Dividing rough measurements of basin width at the islands of Vava'u (~390 km) and Tongatapu (~260 km) by the current geodetic opening rates from *Phillips* [2003] (124.4 km/My and 79.6 km/My, respectively) yields extrapolated ages of basin opening of ~3.1-3.3 Ma, much younger than the accepted estimate of ~6 Ma [*Hawkins*, 1994]. The potential for increasing rates can also be tested through measuring the widths of accreted crust in older chrons prior to the Brunhes. A few spot measurements are shown in *Fig. 3.7*, giving a rough estimate of spreading rates along the ELSC during the Gauss chron (C2An.1n, C2An.2n, C2An.3n, 2.58-3.58 Ma, black “T” symbols on *Fig. 3.7*), and the early stage of the Matuyama (C2r.1r, C2r.2r, 1.95-2.58 Ma, gray “T” symbols on *Fig. 3.7*) [*Cande and Kent*, 1995]. The rates shown in *Fig. 3.7* are only measured along one flank of the ELSC and thus represent half-rates (in mm/yr), if we assume symmetric spreading across the ELSC. Using that assumption, we can come up with a rough estimate of ELSC spreading rates during the Gauss chron of ~72-80 mm/yr, increasing to ~98-100 mm/yr in the early part of the Matuyama, compared to the current predicted rate of ~122 mm/yr from our model (green arrows in *Fig. 3.8a*). While there is uncertainty in the exact rates, these spot measurements provide supporting evidence that Lau Basin opening rates have been increasing through time. In terms of consequences for the kinematic model, this means that there is no solution that can simultaneously fit both the current geodetic rates and rates constrained by magnetic data alone. Therefore, A-T velocities in our final model were chosen to match the most recent geodetic rates from *Phillips* [2003].

3.5. Lau Basin kinematic model

3.5.1. New Lau Basin three-plate kinematic model

Our kinematic model (*Fig. 3.9*) incorporates the observations and interpretations discussed in this study to describe the current motions of the Niuafo'ou, Tonga, and Australia plates relative to each other. This model and the accompanying analysis provide valuable kinematic information and tectonic context for future studies in the Lau Basin and give insight into the evolution of the basin through time. The combination of the mismatch between

magnetically and geodetically constrained opening rates and the multiple lines of evidence for increasing opening rates through time led to a divergence in the final model iterations. In the final model shown in *Fig. 3.9* opening rates are calculated to match Australia-fixed GPS velocities [Phillips, 2003] from stations on the islands of Niuaotupapu, Vava'u, and Tongatapu (*Table 1*). An alternate model with slower magnetically-constrained opening rates is also included in the supplementary material (*Fig. 3.11*) to facilitate direct comparison with the measured widths of Brunhes chron crust. It is not considered a valid "final" model as it does not describe current velocities, nor can it be considered a model for average Brunhes velocities as it does not adequately capture the complexity of basin evolution throughout the Brunhes, a concept that is explored further in 5.4. *Fig. 3.9* shows plate boundaries, predicted relative velocities, Euler pole locations, and GPS velocities (see *Fig. 3.9* for legend). The locations of plate boundaries and plate names in our model generally match those of ZT01, although there is still some uncertainty regarding the exact location of the southern N-T boundary. The foundation of both models is the well-constrained A-T Euler pole (yellow star in *Figs. 3.9/3.10*), but the updated geodetic data required moving the pole ~60 km SW of the ZT01 location (from 177.7°W/25°S to 177.85°W/25.5°S). The angular opening rate was then adjusted until a match (within 0.1 mm/yr) was achieved between predicted and geodetic rates at all three GPS stations (*Table 1*). This resulted in a calculated angular opening rate of 8.3°/My (*Fig. 3.10*). The Brunhes model iteration (*Fig. 3.11*) uses the ZT01 pole from the "Case 1b" model iteration, constrained by the geophysical data but not the geodetic data. The pole location is nearly identical to that shown in *Fig. 3.2* (177.6 W/25.1°S in Case 1b vs. 177.7°W/25°S in Case 2b), but the rates are slightly slower (8.1°/My) and provide a better fit to the magnetic constraints. This model was used to directly compare to measured Brunhes widths in *Fig. 3.7*, and incorporates our magnetically- constrained N-T opening rates. In order to estimate the (assumed) increase in opening rate along the N-T boundary, we compared predicted A-T velocities in our Brunhes model with the current model at the adjacent island of Niuaotupapu, and applied the increase of 7.15% to our magnetically-based rates. This resulted in a minor increase in spreading rates along the FRSC and MTJ, from ~8-30 mm/yr based on the magnetic data alone, to ~8-32 mm/yr.

The primary modifications to the ZT01 model lie in our interpretations of the N-T and A-N boundaries, discussed in detail in sections 3.4.1 and 3.4.2, respectively. To summarize, there are two key differences in our interpretation of the N-T boundary: 1) the Euler pole location,

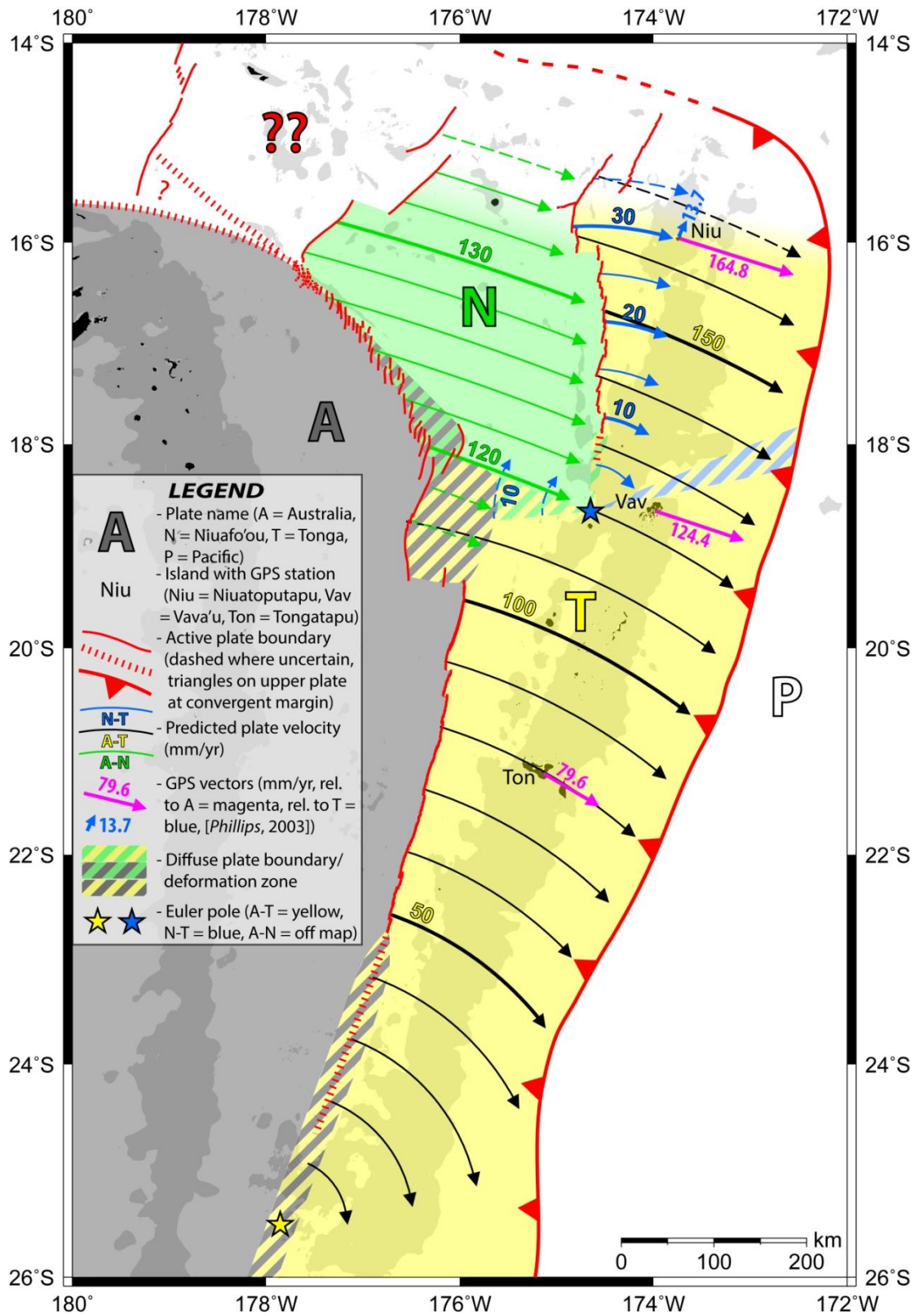


Figure 3.9: New Lau Basin three-plate kinematic model showing plate boundaries, Euler poles, predicted current plate velocities, and GPS velocities, see legend for symbols. Refer to section 3.5 for detailed discussion.

which we place ~200 km NE of the ZT01 pole at 174.65°W/18.65°S, south of the zone of active rifting (blue star in *Figs. 3.9, 3.10, and 3.2*) slow to ultraslow FRSC/MTJ-S spreading rates based on our magnetic profile modeling and geologic interpretation [*Sleeper et al., 2016*]. Our interpretation of the A-N boundary differs in three primary ways: 1) our analysis of flank morphology and the seafloor magnetization pattern around the CLSC suggests that A-N opening rates are higher than predicted in the ZT01 model, 2) the volcanic morphology, distribution of seismicity, and orientations of AVRs and Riedel shears suggest that the A-N boundary is the LETZ extended to its intersection with the NWLSC, 3) the morphologic PR is a fossil feature and not an active transform boundary and therefore not an azimuthal constraint on A-N motion. The A-N Euler pole, located at 175.13°E/37.85°S, was determined geometrically (*Fig. 3.10*) by finding a pole that satisfies three-plate closure criterion (i.e., that it lies on the same great circle as the others (red curve in *Fig. 3.10*), and $A\omega T = A\omega N + N\omega T$, where $A\omega T$ is the vector describing motion of T relative to A [*McKenzie and Parker, 1967; Zellmer and Taylor, 2001*]). The inset in the bottom-right of *Fig. 3.10* shows the angular velocity vectors for each Euler pole, demonstrating three-plate closure. *Table 3.1* summarizes the geodetic and predicted velocities, showing the excellent agreement between the *Phillips* [2003] geodetic rates and our predicted

Table 3.1. GPS velocities, predicted velocities, and predicted spreading rates						
Phillips [2003] GPS velocities, Australia-fixed			Tonga-fixed			
<i>Station</i>	<i>Hor. Vel. (mm/yr)</i>	<i>Azimuth</i>	<i>Hor. Vel. (mm/yr)</i>	<i>Azimuth</i>		
Tongatapu	79.6 +/- 0.3	120.3 +/- 0.2	0.5 +/- 0.3	-		
Vava'u (1)	124.6 +/- 0.4	117.7 +/- 0.2	1.3 +/- 0.4	-		
Vava'u (2)	124.2 +/- 0.2	118.4 +/- 0.1	0.9 +/- 0.2	-		
Niuatoputapu	164.8 +/- 0.6	107.5 +/- 0.3	13.7 +/- 0.7	24.6 +/- 2.8		
Final model velocities (current)			Brunhes model velocities		ZT01 model velocities	
<i>Station</i>	<i>Pred. Vel.</i>	<i>Azimuth</i>	<i>Pred. Vel.</i>	<i>Azimuth</i>	<i>Pred. Vel.</i>	<i>Azimuth</i>
Tongatapu	79.6	119.4	70.4	119.5	72.4	121.2
Vava'u	124.4	117.0	114.2	116.9	117.8	117.9
Niuatoputapu	164.8	111.3	153.8	110.9	158.6	111.7
Predicted spreading rates along each spreading center (mm/yr, south to north)						
<i>Name</i>	<i>Current model</i>	<i>Brunhes model</i>	<i>ZT01 (Case 2b)</i>	<i>Boundary</i>		
VFR	47-69	38-59	39-61	A-T		
ELSC	69-103	59-93	61-97	A-T		
CLSC	101-120	91-109	93-84	A-N/A-T		
LETZ/PR	118-127	108-118	85-78	A-N		
FRSC	8-28	8-26	47-91	N-T		
MTJ-S	27-32	25-30	89-100	N-T		

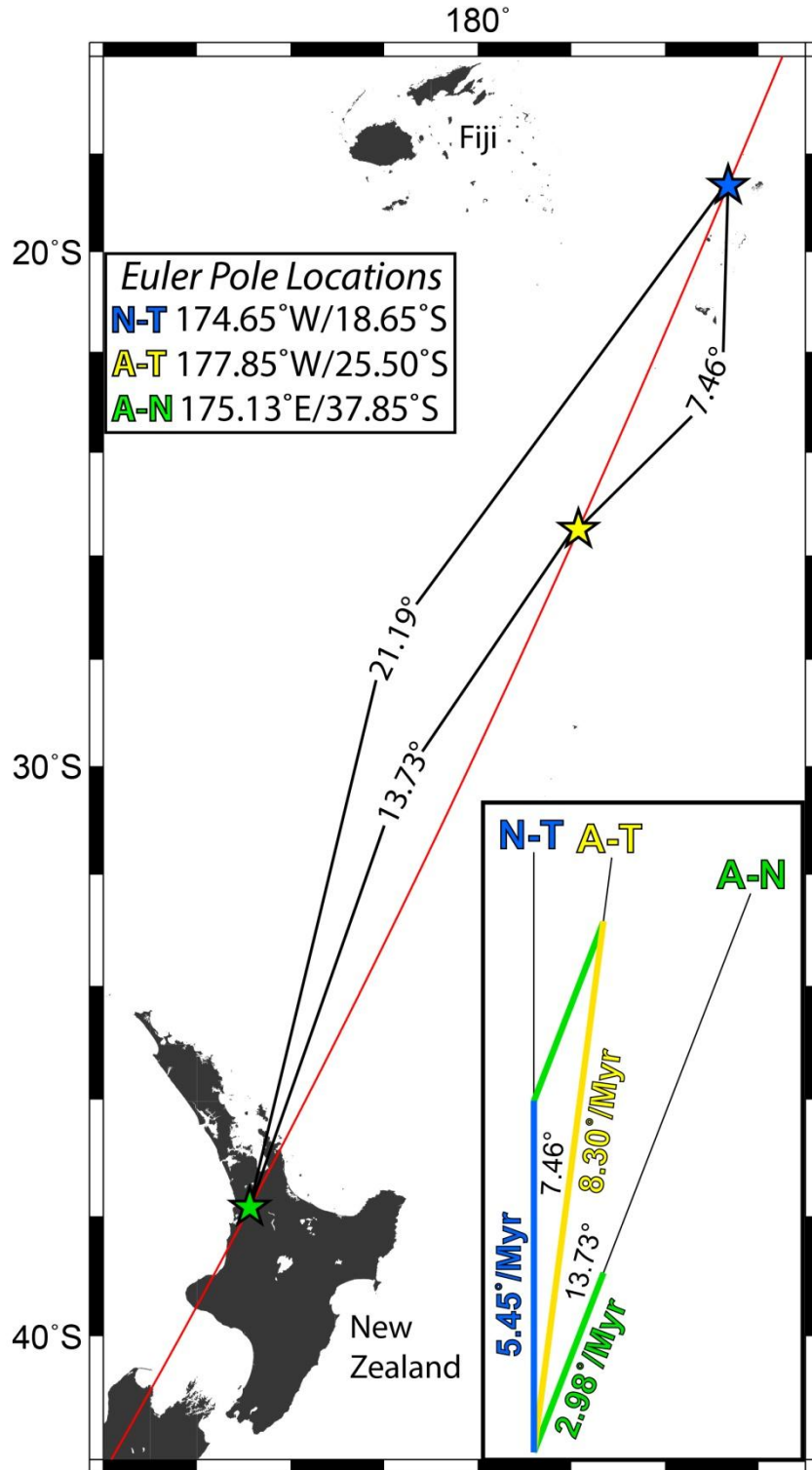


Figure 3.10: Regional map showing Euler pole locations and the great circle (red curve) connecting them. Inset in bottom-right shows angular velocity vectors to demonstrate that the poles and angular opening rates satisfy three plate closure criterion (i.e., $A\omega T = A\omega N + N\omega T$, where $A\omega T$ is the vector describing motion of T relative to A). Inset in top-left lists the three Euler pole locations.

rates, and comparing the predicted spreading rates along each of the named Lau Basin spreading centers in the ZT01 model, our preferred current model, and the alternate model iteration (called "Brunhes model").

One consequence of the increased A-N and A-T opening rates and how they fit into the model as a whole is that the CLSC may no longer be entirely a part of the A-N boundary, as interpreted in ZT01. If the predicted A-N opening rates are projected down to the south end of the CLSC then it should be spreading at ~ 113 mm/yr, ~ 10 mm/yr faster than the adjacent north end of the ELSC. The easiest way to resolve this discrepancy is to consider the CLSC the northern extension of the A-T boundary, for at least the southern portion of the axis. A-N and A-T opening rates converge just south of the 120 mm/yr contour, constraining the most likely location for the southern N-T plate boundary to within the region marked with yellow/green stripes in *Fig. 3.9*. Alternatively, the CLSC may be transitioning between A-T and A-N rates, with total extension partitioned across the northern ELSC, ILSC, and southern CLSC, along with some ongoing tectonic extension within the overlap zone. If the CLSC is entirely a part of the A-N boundary, then the excess motion would have to be taken up within the CLSC/ELSC overlap zone, which is certainly plausible considering that the relative velocity difference is < 10 mm/yr. Thus, it remains an open question as to whether the sliver of crust on the eastern flank of the CLSC is a part of the Niuafu'ou plate or the Tonga plate, or whether it can truly be considered part of a "plate" at all given the active deformation in the overlap zone.

Conder and Wiens [2011] proposed an alternative interpretation that the CLSC/ELSC overlap zone is actually part of a "nanoplate" (~ 1 order of magnitude smaller than a microplate), the limits of which almost exactly coincide with the gray/yellow striped zone east of the CLSC and the gray/green striped zone along the LETZ just to the north in *Fig. 3.9*. While the western and southern boundaries are well-defined and there is significant seismicity along the proposed eastern boundary, the northern boundary is poorly defined, with only a few scattered earthquakes and no morphologic expression of an active plate boundary. Further, the presence of seismicity in the central portion of the nanoplate suggests ongoing deformation, which is not consistent with the definition of a plate. Lastly, the oblong shape of the proposed plate, with the "tail" (gray/green striped zone) extending to the NW, is not consistent with edge-driven microplate kinematics [*Schouten et al.*, 1993]. Thus, while we cannot rule out the possibility of an

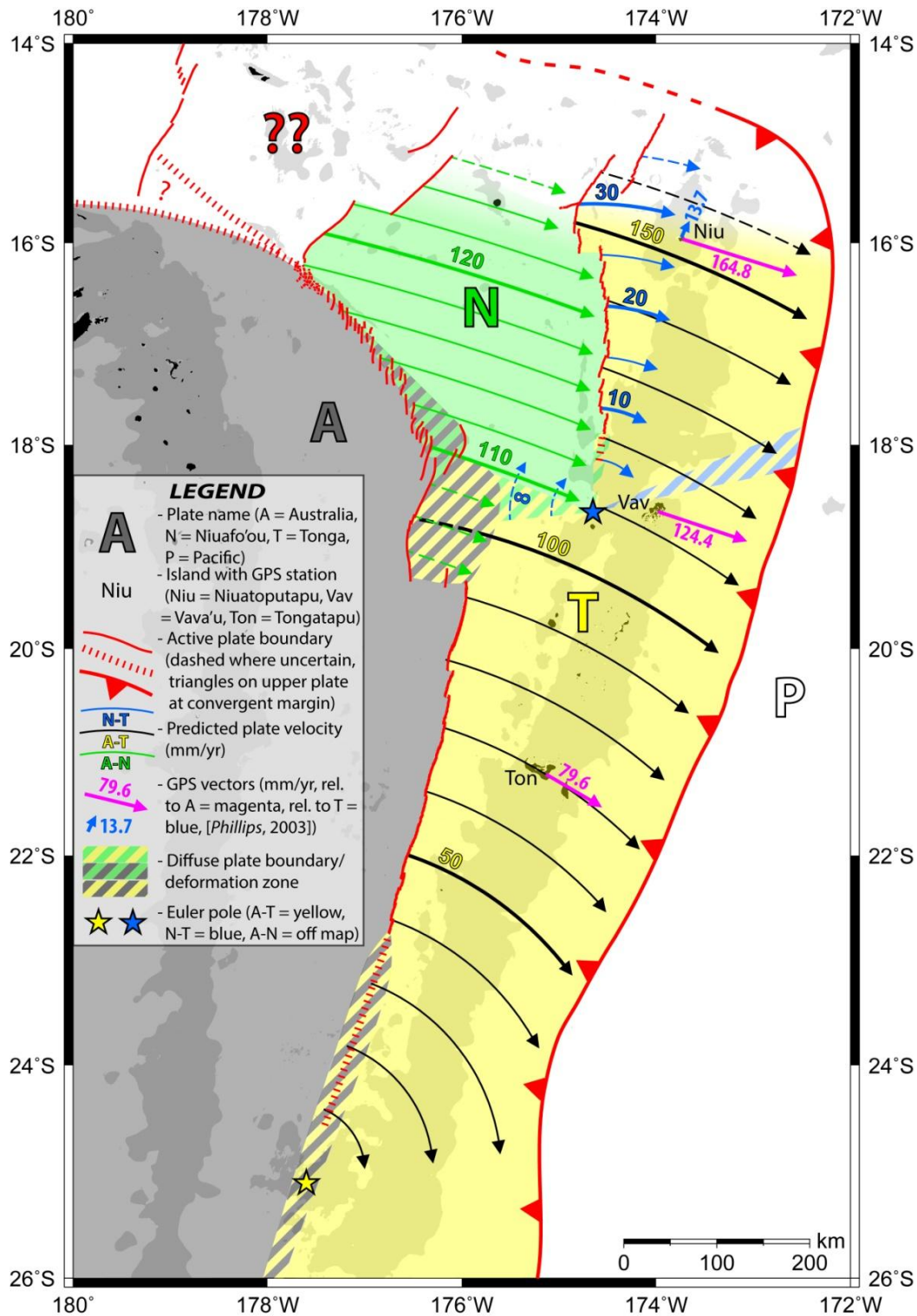


Figure 3.11: Lau Basin kinematic model with basin opening rates constrained by measurements of Brunhes chron widths rather than Australia-Tonga GPS velocities as in Fig. 3.9. Allows for direct comparison with magnetic measurements, but is not considered a valid "final" model due to evidence for changing rates and pole locations throughout the Brunhes chron. A-T pole: 177.6°W/25.1°S, 8.10°/My (from ZT01 Case 1b model); N-T pole: 174.65°W/18.65°S, 5.08°/My (same location as Fig. 3.9, slower rates to match magnetic anomaly modeling); A-N pole: 176.80°E/35.50°S, 3.12°/My (location and rate based on three-plate closure calculations).

ephemeral or incipient nanoplate in this region, we believe that the evidence from morphology and seismicity are more consistent with this being a zone of diffuse deformation.

3.5.2. Niuafu'ou-Tonga southern boundary and the Niuatoputapu plate

While the above revisions resolve most of the geologic discrepancies, there is still a problem of unaccounted-for motion along the southern boundary of the Niuafu'ou microplate. Based on our N-T Euler pole, there should be a small component of relative compression, indicated by dashed blue arrows within the N-T boundary zone (yellow/green stripes in *Fig. 3.9*). The magnitude of this relative motion reaches a maximum of ~10 mm/yr, much smaller than the predicted motion of ~40 mm/yr in the ZT01 model, but large enough that we should expect some evidence of deformation. A potential solution lies in a component of geodetic motion that we have not discussed thus far. The updated geodetic analysis by *Phillips* [2003] indicates that the Niuatoputapu station has a well-defined 13.7 mm/yr northward ($24.6^{\circ} \pm 2.8^{\circ}$) relative motion with respect to the Tongatapu and Vava'u stations (blue arrow in *Fig. 3.9*), which appear fixed with respect to each other (*Table 1*). These GPS data suggest that the Tonga plate ends north of Vava'u and that there may be a separate Niuatoputapu plate to the north [*Conder and Wiens, 2011*], bounded by the FRSC to the west and the Tonga trench to the east and north, with the most likely location for a southern boundary marked with yellow/blue stripes in *Fig. 3.9*. The potential boundary location corresponds to an embayment in the forearc, and there is a change in forearc structure toward the north. The western branch of MTJ and other ~E-W trending extensional structures in the northern basin generally support the existence of a component of northward extension in the northern basin as well. For the purposes of our three-plate model, the hypothesized Niuatoputapu plate largely behaves as if it is part of the Tonga plate. We are not confident in defining a separate plate solely based on motion at one GPS station, and the structures that imply northward extension are all on the opposite flank of the MTJ and NELSC. But if we assume that this northward component indeed represents differential motion of a separate plate, it provides a potential mechanism to relieve the predicted compression at the southern N-T boundary. The magnitude of 13.7 mm/yr is comparable to the maximum predicted compression of ~10 mm/yr and is in approximately the opposite direction, and thus if such a vector also applied to the Niuafu'ou plate it could explain the lack of deformation at the southern N-T boundary while maintaining similar opening kinematics on the FRSC. Furthermore, the

small component of ~N-S shortening due to bookshelf faulting in the ELSC/CLSC overlap zone could be invoked to relieve some of the predicted compression along the N-T boundary. More data are needed to confirm the existence of the Niuatoputapu plate, but even if the northward component does not indicate a separate plate, our model still reduces the predicted relative motion along the southern N-T boundary compared to the ZT01 model and the predicted slow to ultraslow opening rates on the FRSC are more in accord with its geology [Sleeper *et al.*, 2016].

3.5.3. *The nature of Peggy Ridge and insights into A-N boundary evolution*

The interpretation that PR is an active transform fault is not supported by the presence of a surrounding zone of apparently recent volcanism, a comparable zone of positively magnetized crust, the lack of seismicity along the SE portion of the ridge, or the mismatch with the orientation of fault planes in teleseismic strike-slip events (*Fig. 3.8b*), but the exact nature of PR remains uncertain. One significant flaw in our model predictions may actually provide some insight into the nature and evolution of PR. Based on the measured width of the zone of positive magnetization (presumably Brunhes chron crust) along the LETZ and PR, shown in *Fig. 3.7*, there is a strong mismatch with our predicted rates. The spot measurements shown in *Fig. 3.7* vary from 73 mm/yr to 95 mm/yr, but the overall width of positively magnetized crust is highly variable, and measured widths give rates ranging from ~60-100+ mm/yr. Predicted current rates vary from ~120-127 mm/yr (*Fig. 3.9*) and predicted rates based on our magnetically-constrained model vary from ~110-118 mm/yr, so either model provides a poor fit to the measured Brunhes width surrounding PR and the LETZ. One piece of the answer lies in the strike-slip component along this boundary. Since both the purely extensional AVRs and the Riedel shears are active structures, this implies that overall motion along this boundary is partitioned between the extensional and strike-slip components. This is supported by the mismatch between the A-N plate vector of 107° and the expected extension direction of 95° based on AVR and T-axis orientations (*Fig. 3.8b*). Presumably the component of motion not orthogonal to the AVRs can be accommodated as right-lateral slip along the Riedel shears, thus removing the need for oblique spreading along the AVRs. However, this explanation does not solve the problem of the lack of Brunhes crust along this boundary because the strike-slip faults will effectively widen the Brunhes crust as they slip, maintaining or even increasing the overall width.

The simplest way to increase the measured width of Brunhes crust is to make the vector of Niuafu'ou motion more aligned with PR, closer to that predicted by ZT01. However, it is not possible to come up with a fixed three-plate solution using the A-T and N-T poles and opening rates in our model with such a Niuafu'ou plate vector. Furthermore, any azimuth more closely aligned with PR would result in a significant amount of predicted compression along the N-T boundary, which should be evident in both seafloor morphology and seismicity. Therefore, we propose a compromise between the two solutions, where the A-N vector was more closely aligned to PR (not necessarily parallel) during the early part of the Brunhes, and then rotated into its current alignment throughout the Brunhes as the boundary evolved and the CLSC propagated southward. This is also consistent with microplate kinematics in general, in which a growing microplate (surrounded by divergent plate boundaries) must have constantly changing rotation poles if it is edge-driven [Schouten *et al.*, 1993]. The details and timing of this reorganization are poorly constrained and beyond the scope of this study, but this appears to be a plausible way to account for the missing Brunhes crust along the LETZ while still accounting for the geologic and geodetic constraints.

3.5.4. Implications for rigid plate models and the dynamic nature of backarc basins

A number of the observations and interpretations discussed in this study point toward a more rapidly evolving and dynamic history for the Lau Basin than previously described. There are multiple lines of evidence that indicate increasing basin opening rates over time. For the A-T Euler pole, a southward shift was required to precisely match geodetic opening rates, suggesting that this pole may be moving southward over time. It is likely that the N-T pole is also migrating southward over time as well, but we do not have precise enough control on Brunhes spreading rates to predict this motion. Increasing rates and southward Euler pole migration are also consistent with the *Ruellan et al.* [2003] model of zipper-like basin opening from north to south as the Louisville Seamount Chain sweeps southward along the Tonga trench. In addition, there is evidence that the Niuafu'ou plate may be rotating, the A-N plate boundary appears to be in a state of constant evolution and reorganization, and there may even be a separate plate within the Tonga forearc based on the *Phillips* [2003] GPS results discussed in 3.5.2.

The dynamic and rapid nature of basin evolution suggests that kinematic and tectonic models that assume standard rigid plate tectonics in backarc basins should be used judiciously,

and that such models may only be valid for relatively short periods of time. For an example outside of the Lau Basin, *Kato et al.*, [2003] showed evidence for trench-parallel extension within the Mariana forearc based on a mismatch between geodetic data and predicted velocities using a model with a rigid plate rotating about an Euler pole as we have done here. Departures from rigid plate tectonics in the backarc environment are not surprising given that upper plate extension is often driven by trench rollback, which inherently requires large deformation of the lithosphere [*Bevis*, 1988] as the subducting plate departs from a spherical cap at the Earth's surface and sinks into the mantle at the trench. Thus, while rigid plate models for backarc basins are valuable for constraining and predicting spreading rates and plate motion vectors over relatively short timescales, at longer timescales of hundreds of thousands to millions of years, models may need to account for non-rigid behavior induced by trench rollback and its consequences, including migrating poles, rotating plates, propagating boundaries, and intraplate deformation.

3.6. Conclusions

Our revised three-plate kinematic model for the Lau Basin (*Fig. 3.9*) provides a solution that is consistent with geophysical and geodetic constraints, and geological observations along the N-T and A-N boundaries. The morphologic changes along the southern FRSC described in *Sleeper et al.* [2016] are in agreement with our magnetic modeling results, which predict slow to ultraslow rates (~32-8 mm/yr north to south) along the N-T boundary. Our N-T Euler pole location is in agreement with the seismicity pattern and basin morphology, which show no evidence of deformation, volcanism, or extension beyond the arc platform south of the termination of the FRSC axis. For the A-N boundary, we have shown evidence that the entire boundary is volcanically active along a series of en echelon AVR's, suggesting that PR is a fossil feature and thus cannot be used as an azimuthal model constraint for Niuafu'ou microplate motion. Prominent teleseismic strike-slip earthquakes occur predominantly south of PR, have ~E-W oriented T-axes, and their fault planes likely occur on the ephemeral Riedel shears that form as part of the LETZ. We also show evidence from flank morphology and a revised interpretation of the magnetization pattern on the CLSC flanks that opening along the A-N boundary must be faster than the ZT01 model predicts. The increased rates along the A-N

boundary compensate for decreased rates along the N-T boundary, maintaining total A-T opening rates as constrained by GPS stations along the Tonga ridge [Phillips, 2003], which are matched to within 0.1 mm/yr in our final kinematic model. These observations taken together constrain our revised kinematic model (Fig. 3.9), which describes the current motions of the Niufo‘ou and Tonga plates relative to the Australia plate. Our results also provide insight into the complex tectonic history of the Lau Basin, based on evidence for increasing opening rates over time, migrating Euler poles, Niufo'ou plate rotation, and the potential for deformation within the Tonga forearc. These tectonic complications along with evidence for non-rigid plate behavior in other backarc basins suggest that standard models of plate kinematics using rigid plate assumptions should be used judiciously and are likely only valid on relatively short timescales of hundreds of thousands of years or less, depending on overall opening rate and the tectonic setting.

CHAPTER 4: DIFFUSE SPREADING, A NEW MODE OF CRUSTAL ACCRETION IN THE SOUTHERN MARIANA TROUGH BACKARC BASIN

Abstract

We describe a new mode of lithospheric extension and magmatic crustal accretion in backarc basins termed *diffuse spreading* using new observations from the actively opening southern Mariana Trough. Diffuse spreading reflects the abundance and continual addition of slab-derived fluids in backarc basin mantle. Under certain conditions water within the slab-derived fluids may counter the lithospheric dehydration and strengthening predicted to occur beneath mid-ocean ridges, which may help to focus melt generated in broad melting regimes to narrow neovolcanic zones. As a result, backarc extensional deformation, volcanism, and crustal accretion may occur over a broad area instead of along a narrow axis. We interpret diffuse spreading to occur in the southern Mariana Trough, west of the southern terminus of the Malaguana-Gadao Ridge backarc spreading center. The organized narrow spreading axis of this ridge, which forms an axial high in this area, abruptly terminates and is replaced by a broad zone of active volcanism and tectonism characterized by short volcanic ridges, volcanic cones, and deeps. This study uses deep- and shallow-towed sidescan sonar and ship multibeam data, along with archive geophysical, geochemical, and seismicity data in the southern Mariana Trough to describe and distinguish distinct modes of extension spanning tectonic rifting to organized seafloor spreading and the particular features associated with diffuse spreading.

4.1. Introduction

Backarc basins are dynamic and rapidly evolving extensional systems that form within the upper plate and rearward of the volcanic front at many subduction zones. The initial phase of backarc opening involves rifting of weak, thick crust within ~50 km of the arc volcanic front [Chase, 1978; Molnar and Atwater, 1978; Taylor and Karner, 1983]. This is normally followed by a rapid transition from rifting to focused seafloor spreading [e.g., Hussong and Uyeda, 1981; Yamazaki et al., 2003] where new crust is accreted along a narrow segmented axis, in a similar manner to seafloor spreading at mid-ocean ridges (MORs). However, there has long been discussion that in some backarc basins crustal accretion occurs in a "disorganized" manner across a broad region rather than a narrow spreading axis. Early workers [e.g., Hawkins, 1977; Lawver and Hawkins, 1978; Weissel, 1981; Hamburger and Isacks, 1988], based on the complex magnetic anomaly patterns and apparently scattered seismicity in many backarc basins, suggested that backarc spreading may occur in a diffuse manner distributed among multiple sites rather than along a single focused spreading axis. With the benefit of more abundant and higher resolution geophysical data, focused MOR-like spreading axes have been identified in most active backarc basins, including the Mariana Trough [Fryer and Hussong, 1981] and Lau Basin [Parson et al., 1990; Taylor et al., 1996].

The new mode of crustal accretion that we describe here, i.e., diffuse spreading, is different from these previous interpretations. Diffuse spreading is distinct from rifting, which can be magmatic or amagmatic, but always involves deformation of existing lithosphere that predates the extension. It is distinct from organized MOR-like spreading in that the crust is not accreted along a narrow axial zone where volcanism and active faulting are limited to within a few km of the axis, but instead occurs across a broad zone 10's of km across. In diffuse seafloor spreading, all of the crust is newly magmatically accreted with essentially no pre-existing material involved, except perhaps as minor non-deforming slivers trapped between zones of active magmatic spreading. There also is some conflation of the terms "rifting" and "spreading" in the literature. We use these terms herein to describe distinct phenomena. We define "spreading" as lithospheric extension accommodated primarily by magmatic accretion of new crust and advection of asthenospheric material to become new lithosphere. We define "rifting," on the other hand, as lithospheric extension accommodated primarily through the stretching of pre-existing crust and

mantle lithosphere. Volcanism can be associated with rifting as the lithosphere thins and the upwelling asthenosphere undergoes decompression melting, but the extension is primarily accommodated by slip along normal faults, and no new crust or lithosphere are formed. Rifting and spreading are the end-member processes, but intermediate gradations can occur during transitions from one to the other. In oceanic settings, spreading typically takes place in remarkably narrow neovolcanic zones only a few km wide [Macdonald, 1982], whereas in continental rifting extension can occur in zones over a hundred km wide [Buck, 1991]. In true “diffuse spreading,” which we describe here, new crust is magmatically accreted across a broad zone 10's of km wide. This process, although first described in the Lau backarc basin [Martinez and Taylor, 2006], has not generally been recognized as a distinct process, and is often interpreted as rifting or as a transitional phase between rifting and organized spreading. This study describes the volcanic and tectonic structures associated with diffuse spreading and develops a conceptual model to explain the tectono-magmatic conditions that enable this form of extension.

We use ship multibeam, deep-towed sidescan sonar, and gravity data collected during an early 2012 cruise on R/V Thomas G. Thompson (TN273) along with compiled shallow-towed sidescan sonar and geophysical data in the southern Mariana Trough [Becker, 2005] to describe volcanic and tectonic features associated with arc rifting in the Southwest Mariana Rift (SWMR), organized spreading along the Malaguana-Gadao Ridge (MGR, [Becker *et al.*, 2010]), and the intervening ~120 km-long zone that we interpret to be formed through diffuse spreading. These descriptions, combined with analyses of seismicity patterns across the region and geochemical analyses and descriptions of volcanic samples, provide insight into the nature and properties of diffuse spreading.

4.2. Geologic Background: southern Mariana Trough

4.2.1. Mariana Trough opening and tectonics

The Pacific and Philippine Sea plates and the small intervening sliver of Mariana backarc, arc and forearc lithosphere (referred to herein as the Mariana Platelet) all have a WNW component of motion relative to Eurasia determined geodetically [Kato *et al.*, 2003]. Mariana

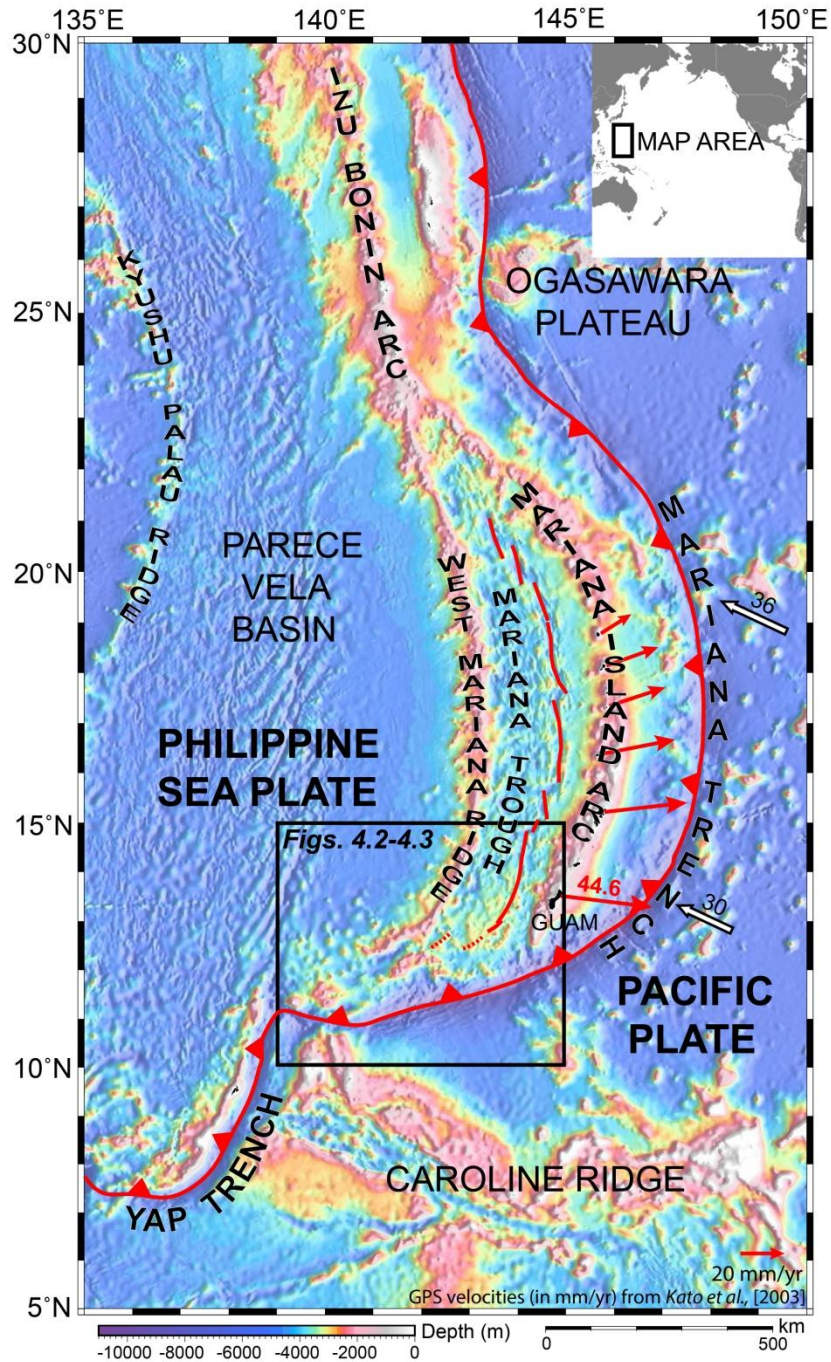


Figure 4.1: Regional bathymetric map using ETOPO2 two arc-minute global relief data [National Geophysical Data Center, 2006]. Major tectonic and volcanic features are labeled, identified spreading axes in the Mariana Trough are marked with black lines, the trench is marked with a bold black line, triangles on the upper plate. GPS vectors from Kato *et al.* [2003] are marked with red arrows (Mariana arc relative to Philippine Sea Plate), and white arrows (Pacific plate relative to the Philippine Sea Plate), all velocities in mm/yr.

Trough opening is driven by a relative lag in the WNW motion of the Mariana Platelet lithosphere relative to that of the Philippine Sea plate. This lag creates a relative rollback of the Mariana Trench and slab with respect to the Philippine Sea plate, although the trench and slab are actually advancing toward Eurasia as indicated by the motion of Mariana island stations [Kato *et al.*, 2003]. The geodetic data [Kato *et al.*, 2003] also indicate second order internal deformation of the Mariana Platelet lithosphere as it bends between the delimiting Ogasawara Plateau and Caroline Ridge [Hsui and Yongquist, 1985; Fryer, 1996, Wallace *et al.*, 2005] (*Fig. 4.1*).

Initial opening of the Mariana Trough began ~10 Ma [Fryer, 1996], separating the remnant arc of the West Mariana Ridge on the western side of the basin and the active Mariana arc along the eastern margin of the basin (*Fig. 4.1*). GPS vectors (relative to the Philippine Sea Plate) from islands along the Mariana arc show that opening rates increase southward with rates of ~15 mm/yr determined near the island of Agrihan (northernmost red arrow on *Fig. 4.1*) to ~45 mm/yr near the island of Guam (*Figs. 4.1, 4.2*) [Kato *et al.*, 2003]. To the south, Seama and Okino [2015] forward modeled spreading rates on each flank of the MGR using two magnetic anomaly profiles across the ridge axis between ~12°50'-13°N, and estimated a rate of 33 mm/yr on the western flank compared to 13 mm/yr on the eastern flank. The total spreading rate of 46 mm/yr is comparable to the GPS results from Kato *et al.*, [2003] at Guam (~13.5°N) although not parallel in direction. While there are no quantitative geodetic or magnetic isochron constraints farther southwest, based on the narrowing width of the basin, presumably opening rates then decrease from the southern tip of the MGR axis toward ~139°30'E/11°30'N, where the Caroline Ridge impinges on the Trench, the rift faults taper out, and seismic evidence of active extension disappears.

Mariana Trench geometry is arcuate and oriented roughly north-south along the central part of the Mariana Trough, but curves strongly toward the SW south of 15°N, becoming nearly E-W where the Caroline Ridge impinges on the Trench, separating the Mariana and Yap Trenches at a sharp cusp in the trench axis (*Fig. 4.1*). The slab contours in *Fig. 4.2* [Hayes *et al.*, 2012] show that the slab geometry generally follows the curvature of the Mariana Trench. This is reflected in the curving backarc seafloor fabric on the Philippine Sea Plate, defined by bathymetric lineations, from ~N-S along the MGR to ENE-WSW west of the MGR terminus

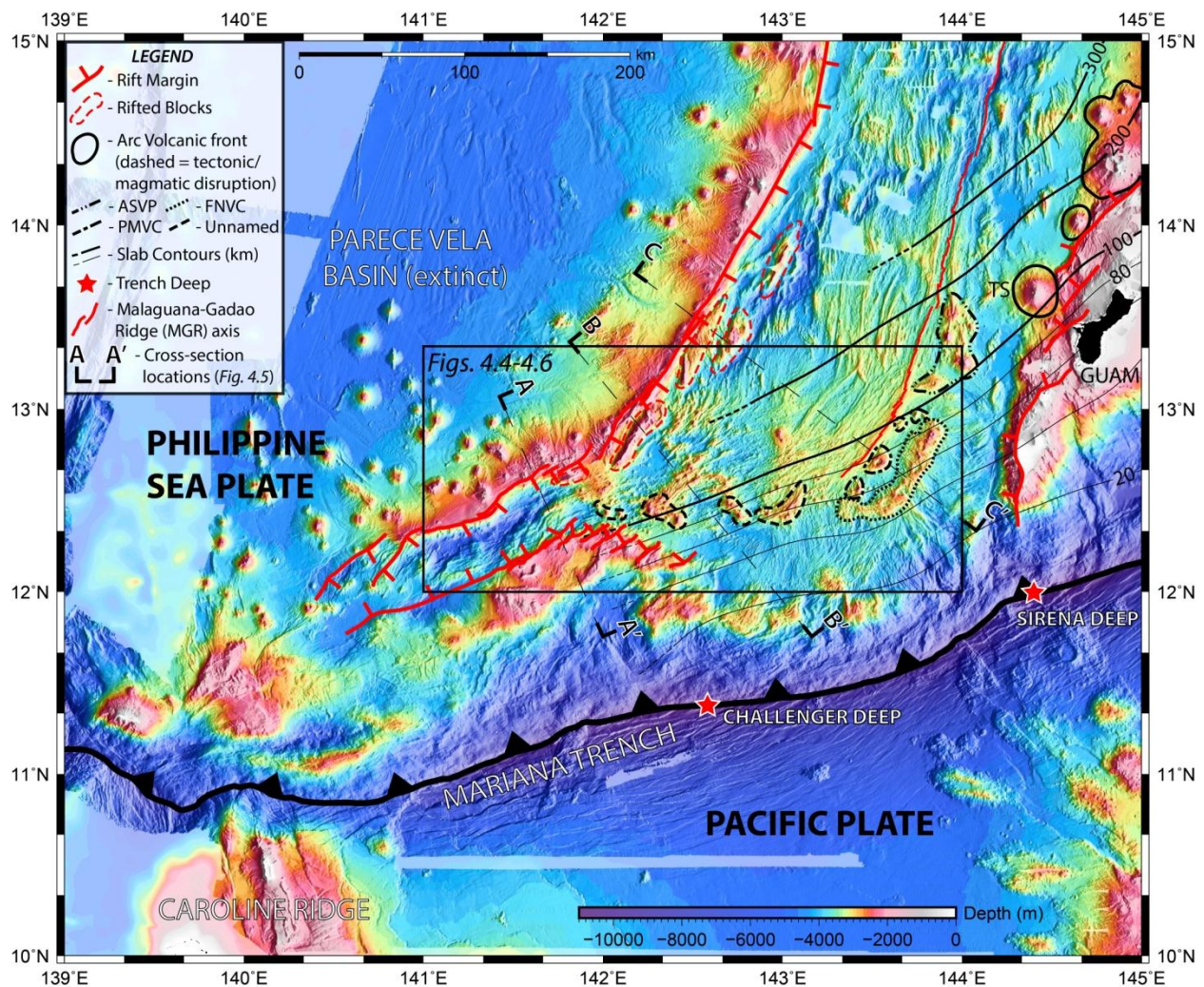


Figure 4.2: Compiled bathymetric map (0.001° cell size) of the southern Mariana Trough showing the relevant tectonic and volcanic features, see legend for symbols. Gaps in multibeam coverage in this and subsequent bathymetric maps are filled with predicted bathymetry from satellite altimeter measurements (reduced opacity) [Smith and Sandwell, 1997]. ASVP = Alphabet Seamount Volcanic Province, FNVC = Fina Nagu Volcanic Chain, PMVC = Patgon Masala Volcanic Chain, TS = Tracey Seamount. Black box shows study focus area and location of Figs. 4.4-4.6. Slab contours are from the Slab 1.0 model [Hayes et al., 2012]. Sections A-A', B-B', and C-C' are shown in Fig. 4.5.

(Fig. 4.3), indicating that the orientation of extensional stresses is rotating in concert with the slab and trench. The overall curvature of the trench and concurrent rotation of extensional fabric are consistent with Mariana Trough opening by rollback relative to the Philippine Sea plate approximately perpendicular to the trend of the Trench [Martinez et al., 2000]. Where the Trench curves to an ~E-W orientation there is a southward component of rollback [Fryer et al., 2003], but there is also an E-W component of extension reflected by the GPS vector at Guam relative to the Philippine Sea plate [Kato et al., 2003]. This E-W component may be faster than the N-S

component and these two extensional components are accommodated differently in the southern Trough. The MGR acts as a discontinuity partitioning extension between its two flanks [Martinez *et al.*, 2000], the Philippine Sea plate and the Mariana Platelet. Crust accreted onto the Philippine Sea plate is passively spread away from the MGR axis as part of a rigid lithosphere and is not further deformed, recording the configuration of the axis at the time of formation through abyssal hills, segmentation boundaries, and other spreading fabric [Martinez *et al.*, 2000]. The Mariana Platelet on the other hand does not behave rigidly and continues to deform after spreading away from the axis, primarily through E-W extension. This controls the formation of the Southeast Mariana Forearc Rift (SEMFR), within the forearc east of $\sim 143^{\circ}30'$, bounded on the north and south by the Fina Nagu Volcanic Chain and the Mariana Trench, and other tectono-magmatic fabric oriented at high angle to the MGR trend (generalized fabric shown in black and labeled on Fig. 4.3; [Martinez *et al.*, 2000; Ribeiro *et al.*, 2013]). This internal deformation of the Mariana Platelet also shows that the overall opening of the Trough can't be explained by an Eulerian rotation of the Philippine Sea plate away from a fixed Mariana Trench and slab. Further west beyond $\sim 142^{\circ}\text{E}$, SWMR morphology is characterized by a deep graben and down-dropped fault blocks typical of an active rift valley. Within the SWMR (labeled on Fig. 4.3), the fabric defined by the major faults is rotated $\sim 15\text{-}20^{\circ}$ counter-clockwise relative to the implied extension direction based on the trench orientation and the overall trend of the rifted margins. This observed obliquity is consistent with global observations as well as numerical and thermochemical modeling [Brune *et al.*, 2012] showing that in the early stages of tectonic rifting, it is mechanically preferred for extensional strain to accumulate on oblique structures rather than orthogonal structures, as is typical for seafloor spreading. It may also be that the oblique structures are part of a zig zag fault pattern that characterizes the shape of the main border faults and develops because of a three-dimensional strain field resulting in an orthorhombic fault pattern [Reches, 1983; Reches and Dieterich, 1983].

4.2.2. Volcanism in the southern Mariana Trough

The central portion of the basin between $\sim 14^{\circ}$ and 19°N has a relatively simple configuration, with a well-defined ~ 200 km wide forearc, a mature arc volcanic front, and focused crustal accretion along a narrow and segmented spreading axis morphologically similar to slow-spreading MORs, the Mariana Trough spreading center. The southernmost segments are

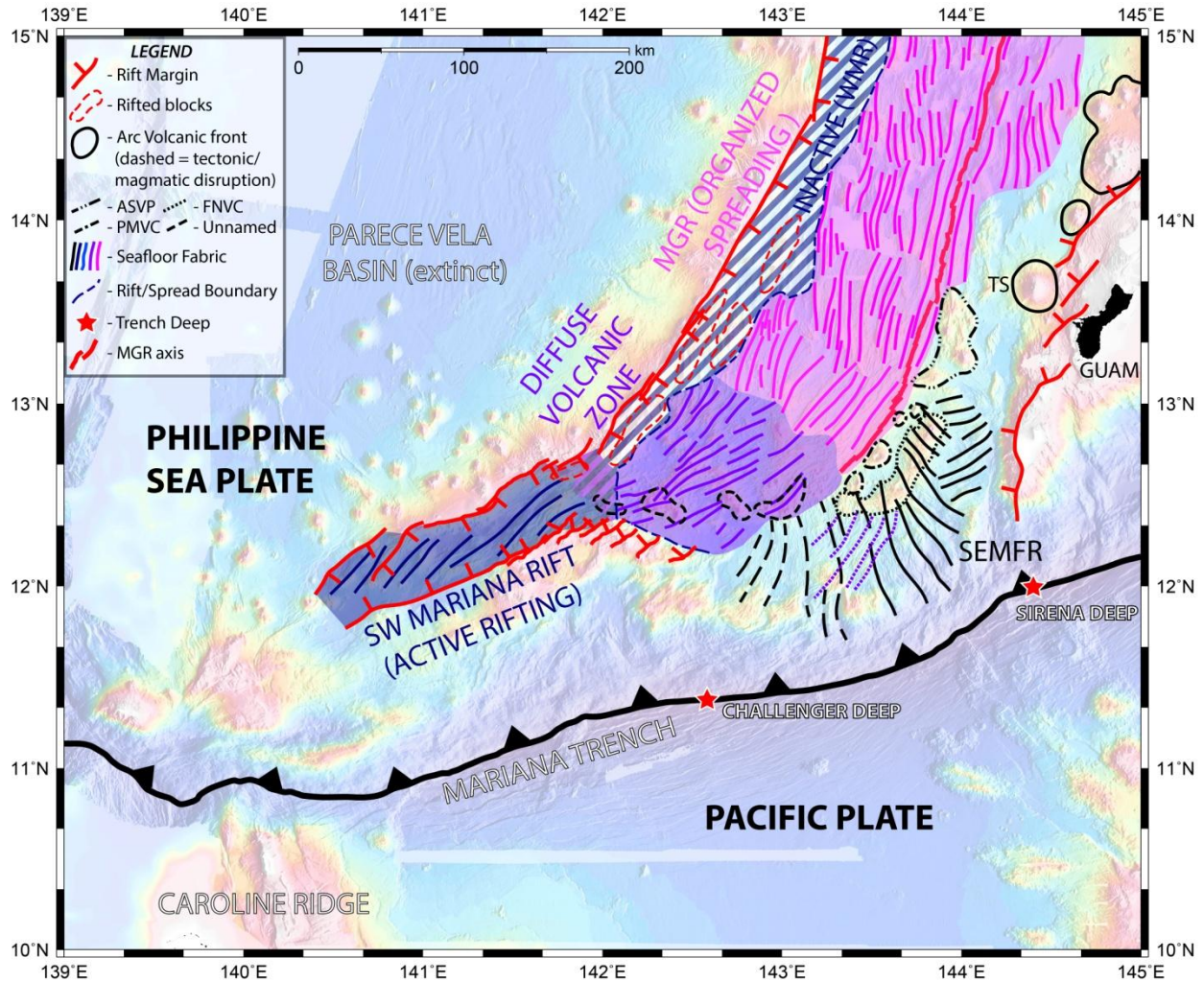


Figure 4.3: Generalized map of southern Mariana Trough seafloor fabric with major volcanic and tectonic lineations mapped. Four regimes are recognized based on seafloor morphology and color-coded: 1) SW Mariana Rift (blue), blue striped zone indicates inactive rift fabric along the West Mariana Ridge. Purple and blue stripes indicate a short transition zone between the SW Mariana Rift and the diffuse spreading zone to the east. 2) diffuse volcanic zone (purple), dotted purple lines indicate aligned relict fabric within the forearc. 3) organized spreading along the MGR (magenta), and 4) SE Mariana Forearc Rift (SEMFR, solid black lines, not the focus of this study). Dashed black lines to the east indicate the less active portion of the forearc. The purple and blue striped boundary represents a short transition zone between the diffuse spreading zone and the SW Mariana Rift. The boundary between rifted and spread crust is shown with a dashed blue line, see legend for symbols.

referred to as the MGR and are magmatically robust, forming an axial high [Martinez *et al.*, 2000; Becker *et al.*, 2010] (solid red line in Fig. 4.2). The bathymetric map (Fig. 4.2) shows the major volcanic and tectonic features of the southern Mariana Trough. The ~200 km wide forearc platform that is continuous toward the north abruptly terminates southwest of Guam, and the forearc between 142°-144°E is undergoing ~E-W extension [Fryer *et al.*, 1998; Kato *et al.*, 2003; Martinez *et al.*, 2000; Ribeiro *et al.*, 2013]. The morphology and character of the arc volcanic front also abruptly changes west of 144°E [Fryer *et al.*, 1998, Stern *et al.*, 2013; Masuda and

Fryer, 2015; Brounce et al., 2016]. At Tracey Seamount, ~30 km northwest of Guam (labeled "TS" on *Fig. 4.2*), and along the arc toward the north, the arc volcanoes form steep-sided conical edifices ~30-100+ km in diameter (solid black outlines in *Fig. 4.2*), reaching depths shallower than 1000 m in many cases, and forming volcanic islands farther north along the chain. The arc volcanoes adjacent to the MGR axis and extending west of the southern terminus have all been tectonically disrupted by extensional faulting and/or magmatically disrupted due to withdrawal of melt likely captured by the adjacent MGR (indicated by dashed outlines on *Fig. 4.2*, different dash styles correspond to different volcanic chains/clusters, see legend) [*Fryer et al., 1998*]. The Alphabet Seamount Volcanic Province arc volcanoes east of the MGR axis from ~13°15'-13°40'N [*Stern et al., 2013*] and the Fina Nagu Volcanic Chain [*Brounce et al., 2016*] southeast of the axis between 12°20'-13°N are smaller and deeper than typical Mariana arc front volcanoes because some of the melt may be captured by the adjacent spreading center [*Becker et al., 2010; Martinez et al., 2000*], and ~axis-perpendicular ridge structures and lineaments indicate some tectonic extension as well [*Fryer et al., 1998*]. *Brounce et al. [2016]* also infer an age progression to the Fina Nagu chain, younging to the NW, such that the extending margin may have distributed volcanism that otherwise would have formed fewer and larger edifices. While there is still some recent volcanism along the Fina Nagu chain, *Masuda and Fryer [2015]* interpret the active arc volcanic front to be the poorly defined chain of seamounts that lies between the MGR axis and the Fina Nagu chain, called the Patgon-Masala Volcanic Chain. Clusters of shallow volcanic cones and ridges southwest of the MGR terminus (outlined in *Fig. 4.2*) mark our interpretation of the poorly defined presumed arc volcanic front extending to the west, following *Fryer et al. [1998]*.

Due to the curvature of the slab (contours from Slab 1.0 model [*Hayes et al., 2012*], *Fig. 4.2*) the entire region between the MGR tip and the SWMR (*Fig. 4.3*) overlies slab depths typical of the arc volcanic front (~80-150 km), implying abundant hydrous flux melting throughout the region [*Fryer et al., 1998*]. Although sampling is relatively sparse and there are only four published analyses, the available descriptions and analyses indicate relatively recent volcanism distributed throughout much of this region. Measurements of water content were conducted on two volcanic samples from ~15-20 km west of the MGR terminus that contain between 1.49-1.93 wt.% H₂O with no resolvable CO₂, making these minimum constraints on the magmatic H₂O contents [*Brounce et al., 2014*]. These H₂O contents are less than typical Mariana volcanic front

lavas, but significantly higher than MORB contents [Kelley *et al.*, 2006; Plank *et al.*, 2013], and are similar to the mean H₂O of Mariana Trough basalts [Stolper and Newman, 1994]. Additional samples were dredged throughout this region in 2006 but none have yet been analyzed beyond onboard descriptions included in the cruise report [Masuda *et al.*, 2006]. The samples are all described as basaltic lavas, many with quenched glass, and particularly fresh lavas from the eastern portion of the region ~15 km west of the MGR terminus. Dredged samples from one of the volcanic cones south of the shallow platform at ~142°E (blue and purple-striped zone in Fig. 4.3) recovered fresh, glassy lavas with arc-like compositions [Becker, 2005; Pearce *et al.*, 2005], indicating recent volcanic activity here. The lack of cones to the west within the SWMR suggests that this is the western terminus of the arc volcanic front within the Mariana Trough. Within the SWMR, Shinkai dives 1400 and 1401 during the YK1413 cruise in 2014 recovered basalts and gabbro with both backarc and arc affinities based on trace element analyses, from the eastern part of the rift near 141°41'E and 141°34'E, respectively [Ohara *et al.*, 2014]. The volcanic cones toward the west end of the SWMR between 140°20'E-141°E are cut by large faults and a dredge on the seamount at ~140°22'E/11°53'N yielded manganese-coated reef-forming coral [Becker, 2005]. Another dredge of a feature at the base of the fault scarp along the NW margin of the SWMR recovered highly altered fragments of basalt, gabbro, and carbonates that were interpreted to be part of a talus pile [Becker, 2005]. Locations of samples collected and analyzed by others within the SWMR and the region to the east are plotted on the sonar backscatter image in Fig. 4.5b.

4.3. Methodology: Geophysical data sets and processing

Bathymetric maps were created from a regional dataset from the University of New Hampshire Center for Coastal & Ocean Mapping/Joint Hydrographic Center (UNH/CCOM-JHC) Law of the Sea expeditions [Armstrong, 2001], supplemented with data from the National Geophysical Data Center (NGDC, ngdc.noaa.gov), and *R/V Thomas G. Thompson* cruise TN273. The final multibeam compilation includes data collected during 43 expeditions from the NGDC database, omitting only data that added noise without increasing the coverage area. During the TN273 expedition, a deep-towed sidescan sonar survey using the 30 kHz IMI-30 instrument covered the southernmost portion of the MGR axis and a small area southwest of the axis,

providing high-resolution imagery (gridded at 0.00003° or ~ 3 m) of fine-scale volcanic and tectonic structures (Fig. 4.7). Due to the limited coverage area of the deep-towed survey, the regional sidescan sonar map in Fig. 4.5b was created from a combined grid of two HMR-1 shallow-towed sidescan sonar surveys in 1997 on *R/V Moana Wave* (MW9719) [Martinez et al., 2000] and 2001 on *R/V Melville* (COOK06MV) [Fryer et al., 2003]. Compiled multibeam backscatter data from the UNH/CCOM-JHC Law of the Sea expeditions were used to fill in around the HMR-1 survey areas. Gravity data from shipboard gravimeters were also compiled from both the NGDC and JAMSTEC databases, and used to calculate mantle Bouguer anomalies using GMT software [Wessel et al., 2013]. Gaps in both the multibeam and gravity datasets were filled with predicted bathymetry and gravity from satellite altimeter measurements [Smith and Sandwell, 1997; Sandwell et al., 2014]. The mantle Bouguer anomaly shown in Fig. 4.6a was calculated by removing the gravitational effects of 6 km-thick crust (MGR crust varies between ~ 5.9 - 6.9 km [Kitada et al., 2006]) from the Bouguer anomaly, using densities of 1035 kg/m^3 for water, 2700 kg/m^3 for crust, and 3300 kg/m^3 for mantle. The gridded gravity data and bathymetry data were resampled in a 2048×2048 cell grid, with a resultant cell spacing of ~ 270 m ($.00244^\circ$), and five terms were used in the Parker expansion. The data still contain the long wavelength signal from the underlying slab, but this does not affect our qualitative interpretations of the much shorter wavelength variations in the backarc region. Earthquake focal mechanisms in Fig. 4.6b were obtained from the Harvard CMT catalog [Dziewonski et al., 1981; Ekström et al., 2012], along with locations of earthquakes (limited to body wave magnitude four or greater) from the International Seismological Centre reviewed event catalogue [International Seismological Centre, 2013]. Depth was limited to ≤ 50 km to isolate upper plate earthquakes. The total moment release discussed in section 4.4.4 was calculated using a formula: $Moment = 10^{(1.5 * Magnitude + 16.1)}$ to convert body-wave magnitude into seismic moment for each event, then the total moment is simply the sum of the moments for each of the earthquakes.

4.4. Observations and results

The evidence for a distinct accretionary magmatic process in the region between the MGR axis and the SWMR to the west comes primarily from contrasts in seafloor morphology and seismicity between the three regions. The following sub-sections present the seafloor

morphology and seismicity associated with rifting in the SWMR, organized spreading along the MGR, and the unnamed intervening region that we refer to as the southern Mariana diffuse volcanic zone (DVZ), providing important insights into the nature of the processes. Bathymetry of the study area (*Fig. 4.4*), zooming in on the SWMR (*Fig. 4.4b*), the DVZ (*Fig. 4.4c*), and the MGR (*Fig. 4.4d*), highlights the morphologic contrasts between the regions. We present the interpreted sonar data (*Fig. 4.5*), with our mapping of the seafloor fabric (defined by tectonic and volcanic lineations) and volcanic cones overlaid on a compiled bathymetry map (*Fig. 4.5a*), a sonar backscatter map (*Fig. 4.5b*), and topographic cross-sections through each of the zones. We mapped the mantle Bouguer anomaly data (*Fig. 4.6a*) and created a map of seismicity overlaid on the bathymetry (*Fig. 4.6b*). Finally, our samples of high-resolution bathymetry and deep-towed IMI-30 sonar data (*Fig. 4.7*), show comparisons of the fine-scale acoustic textures of narrow organized spreading at the MGR axis and the transition to what we interpret as diffuse spreading at the eastern edge of the DVZ.

4.4.1. Southwest Mariana Rift morphology

The SWMR (*Fig. 4.4b*) is characterized by a ~40 km-wide graben, bounded by steep faulted margins with up to 3500 m of relief from the rift floor to the top of the uplifted rift margins. Within the rift, locally reaching depths over 5500 m in some places, are down-dropped fault blocks, the largest and best-defined of which are mapped with dashed red lines in *Figs. 4.2-4.6*. Similar rift-type morphology, consisting of down-dropped blocks separated by steep inward-facing escarpments, can be observed outside of the active SWMR in a ~20-50 km-wide zone along the eastern flank of the West Mariana Ridge (blue striped zone labeled "INACTIVE (WMR)" in *Fig. 4.3*), but these features do not extend into the DVZ or MGR flanks. The narrow zone of rift-type morphology along the eastern West Mariana Ridge implies a distinct rifting phase that rapidly transitions into a different mode of extension in the DVZ, or organized spreading along the MGR flanks.

The SWMR is asymmetric (see cross-section A-A' in *Fig. 4.5*). The NW margin is largely defined by a single normal fault scarp with relief of >3000 m that in some places may splay into multiple surface traces. An example is indicated in *Fig. 4.4b* with a black arrow along the NW margin, where it transitions from a single trace to the west to multiple traces to the east. The SE margin is less continuous and more pervasively faulted, and there is a large heavily deformed

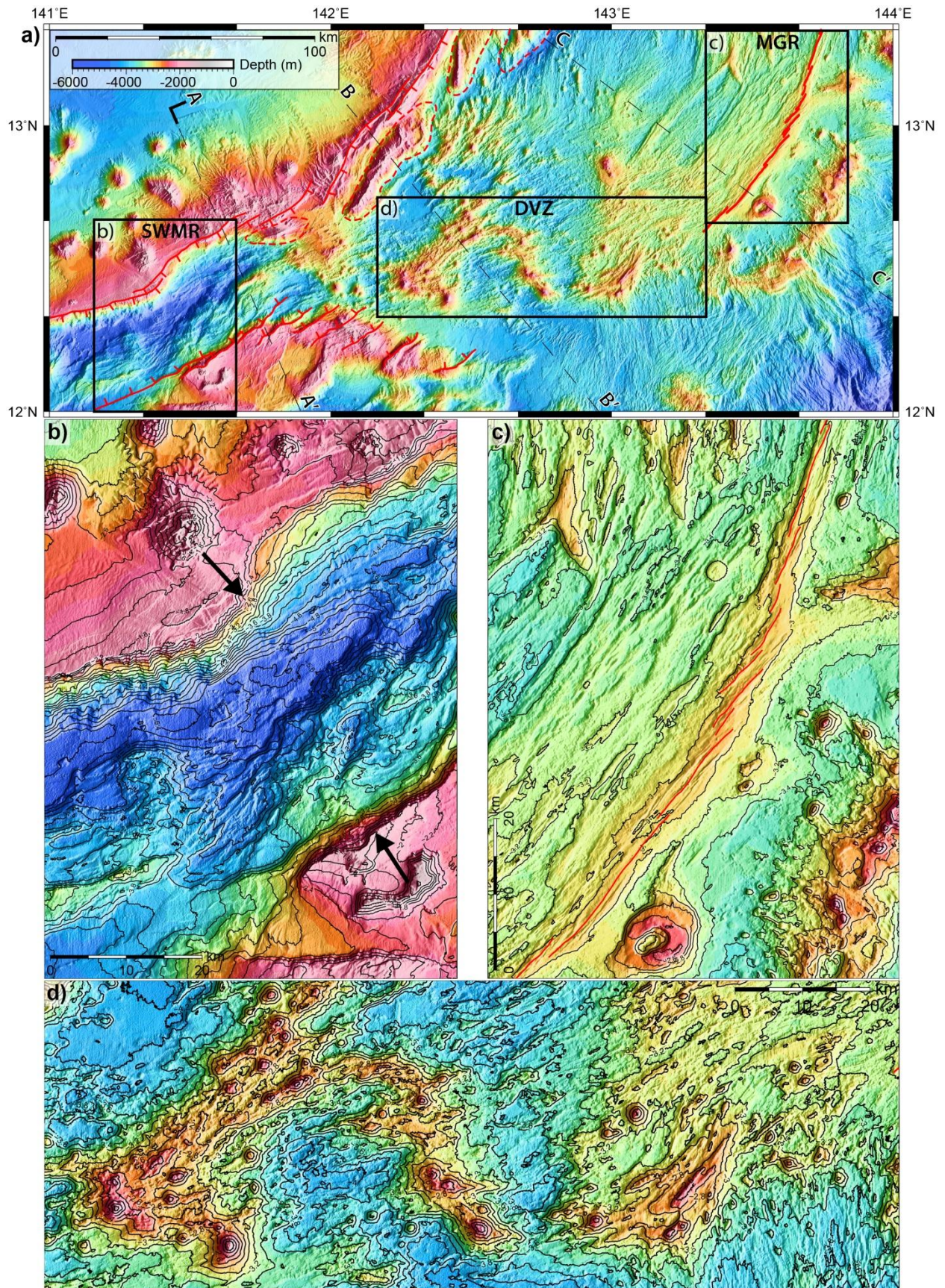


Figure 4.4: Detailed bathymetry maps showing type morphologies for active rifting in the SWMR, the DVZ, and organized spreading along the MGR flanks. a) Compiled bathymetry map (0.001° cell size) of the focus area, black boxes delimit the extent of panels b), c), and d). b) Compiled bathymetry map (0.0003° cell size) showing SWMR morphology. c) Compiled bathymetry map (0.0003° cell size) showing organized spreading morphology on the MGR flanks. d) Compiled bathymetry map (0.0003° cell size) showing DVZ morphology. See section 4.4 for detailed descriptions.

block between the outermost fault scarp (marked with a black arrow in *Fig. 4.4b* along the SE margin) and the deepest part of the rift, causing the SE margin to step down in several blocks rather than as a single steep scarp intersecting the valley floor (*Fig. 4.4b*). The backscatter image in *Fig. 4.5b* shows generally low backscatter intensities within the SWMR consistent with sediment-covered fault blocks, interspersed with irregular lineations interpreted as fault scarps, which appear as either shadows or strong reflections depending on the ensonification direction. There is no clear evidence of recent volcanism within the rift graben based on the backscatter data, the lack of volcanic cones, and the sparse samples that have been recovered, but we can't rule out the possibility of minor fault-controlled volcanism in localized areas. The mantle Bouguer anomaly in *Fig. 4.6a* is consistent with crustal thinning, with the broad lows of the thick arc crust (~-90 to -130 mGal) abruptly transitioning to higher values (~-45 to -90 mGal) within the rift valley where the crust is presumably thinner. The volcanic cones on and south of the shallow platform at ~142°E resemble those found in the DVZ to the east, but the shallow platform has similar gravity anomalies (~-65 to -90 mGal) to the surrounding thick arc crust (*Fig. 4.6a*), indicating that it may be a block of pre-existing crust. The two teleseismically detected earthquakes with normal faulting motions in this area (*Fig. 4.6b*) also indicate ongoing rifting here.

4.4.2. Diffuse volcanic zone morphology

We define the DVZ as extending from 142°05'E to the western end of the MGR at 143°20'E (see purple zone in *Fig. 4.3*). East of ~142°E where the rift margins diverge, the deep grabens, kilometer-scale normal faults, and down-dropped crustal blocks characteristic of the SWMR are no longer observed outside of the narrow inactive rift zone (blue stripes in *Fig. 4.3*) along the West Mariana Ridge. The seafloor in the DVZ has lower relief than the SWMR, with fabric characterized by narrow, closely-spaced ridges, and volcanic cones. The bathymetric map in *Fig. 4.4d* shows the variety of morphologies in the DVZ, and similar volcanic and tectonic features extend northward to the West Mariana Ridge rift margin. The deeper seafloor

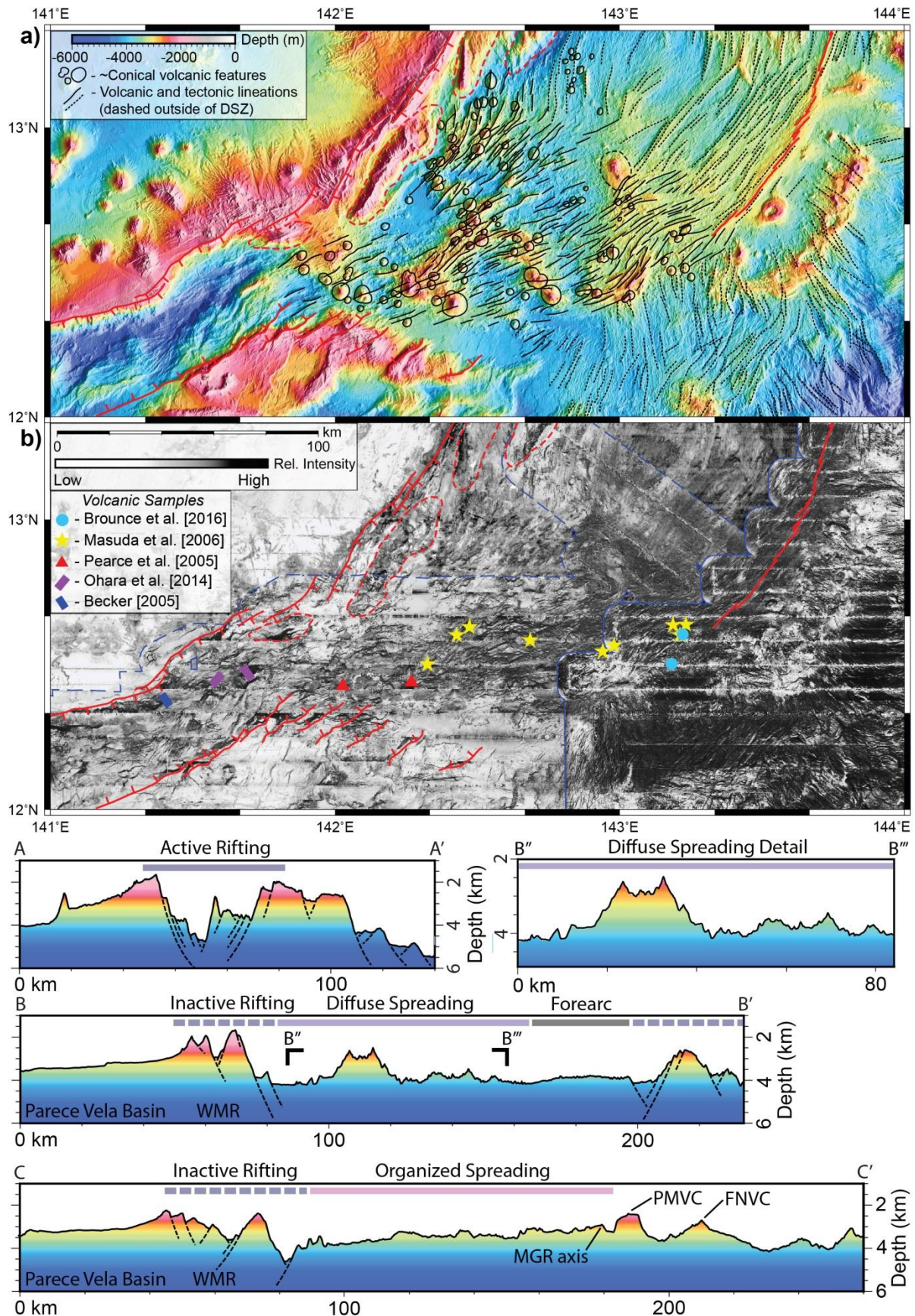


Figure 4.5: Interpreted sonar imagery of study area showing detailed tectonic fabric, along with cross-sections A-A', B-B', C-C', cross section locations shown on *Fig. 4.2*. a) Bathymetry map (same as *Fig. 4.4a*) showing detailed mapping of tectonic and volcanic lineations and conical volcanic features. b) Compiled sonar backscatter map (0.001° cell size) showing both HMR-1 shallow-towed surveys (solid blue line = MW9719 survey limits, dashed blue line = COOK06MV survey limits), with the background filled in using the UNH/CCOM-JHC Law of the Sea compiled multibeam backscatter data. Cross sections: A-A': typical cross-section through the active rift valley, with some of the major rift faults schematically mapped based on the surface topography. B-B': typical cross-section through the DVZ, showing the inactive rift fabric of the West Mariana Ridge (WMR) transitioning abruptly into diffuse volcanic fabric. The cross-section intersects the sedimented basin adjacent to the West Mariana Ridge, along with a shallow volcanic ridge and a deep within the active zone. B''-B''': close-up of a portion of B-B' to show the volcanic terrain in more detail. C-C': typical cross-section across the MGR flanks, showing West Mariana Ridge rift fabric abruptly transitioning into abyssal hill-type fabric on the NW flank of the MGR, and also intersecting the Patgon-Masala and Fina Nagu Volcanic Chains on the SE flank of the MGR.

surrounding the volcanic edifices in the DVZ is over 1000 m shallower than the bottom of the SWMR. Fault scarps in the DVZ reach a maximum height of ~500 m, much smaller than the normal faults bounding the SWMR graben. Cross-section B-B' (*Fig. 4.5*) intersects the inactive rift fabric along the West Mariana Ridge, and crosses the diffuse spreading fabric in the backarc (see B''-B''' for detailed blow-up), showing the contrasts in seafloor depth and relief.

The DVZ is characterized by a variety of morphologies that can be grouped into three main types: volcanic cones, volcanic ridges, and localized deeps. A similar mix of morphologies was described in the Havre Trough backarc basin by *Fujiwara et al.* [2001], and given the term "ridges and knolls" terrain, which aptly describes the overall appearance (although they interpreted the terrain as "rifting," different from herein). While cones, ridges, and deeps are observed throughout the DVZ, there are notable differences between the eastern and western halves, separated by the relatively deep zone at ~142°50'E. The western half is more variable in depth, with rougher topography and relief of up to 2000 m between the high-standing volcanic features and the surrounding deeps, which average ~4000 m in depth. Volcanic cones are more abundant compared to the eastern half (*Fig. 4.5a*) and have shallower summits, with 17 cones shallower than 2500 m compared to only 3 in the eastern half. The eastern half is elevated relative to the western half overall (*Fig. 4.4d*), with the deepest seafloor near the edges reaching ~3600 m, and most of the seafloor surrounding the volcanic constructions varying between ~3000 to 3400 m. The volcanic features also have lower relief of a few 100 m up to ~1200 m along the shallow volcanic ridge located at ~143°05'E/12°27'N, giving the seafloor a smoother appearance relative to the western half. The seafloor depth and overall appearance of the eastern half is similar to the MGR flanks, but with no clear spreading axis, a less well organized fabric, and more abundant cones, particularly in the south along the presumed arc volcanic front.

The volcanic features in the DVZ lie on a morphologic continuum in aspect ratio, from nearly circular cones to elongate cones with rift zones aligned with the local fabric, to linear ridges that shoal toward the center. The cones vary in diameter from a few 100 m to nearly 10 km, with summit depths that vary from ~3500 m to as shallow as ~1800 m. The larger conical features with diameters greater than ~1-2 km are outlined on *Fig. 4.5* to highlight their distribution, along with both the volcanic lineations, defined by the ridge-crests and rift zones extending away from some of the more elongate edifices, and tectonic lineations (consisting of normal fault scarps). The volcanic ridges are not continuous and there is no clear segmentation pattern, but the overall lengths of a few km up to ~20 km are consistent with third-order segment lengths along the MGR. Also, the seafloor on either side of the volcanic ridges is at a similar depth and the ridges themselves have relatively symmetric slopes on both sides. Many of the deeps, particularly in the western half of the DVZ, are bounded by a fault scarp on at least one side, but many are simply defined by being a topographic low between two high-standing volcanic ridges, hence the use of the more general term “deep” as opposed to “graben” to describe these features.

The sidescan sonar imagery of the DVZ (*Fig. 4.5b*) shows a broad zone of high acoustic backscatter that is over 50 km wide near the MGR terminus, tapering down toward the west until it pinches out in the rift valley just west of 142°E. HMR-1 shallow-towed sidescan imagery, described in detail in *Becker* [2005], shows that the high backscatter is related to a combination of effusive volcanism with high backscatter surfaces and lobate margins, and pervasive faulting throughout the region, although most of the faults are too small to resolve in the bathymetry data. The much lower backscatter and subdued topography in the regions to the north and south is consistent with sediment cover, suggesting that the high backscatter zone is at least more recently active in comparison. None of the samples collected by others (shown in *Fig. 5b* and discussed in 4.2.2) have been dated, so we do not have precise control on how recent activity is, but the sample descriptions and available analyses are consistent with relatively recent activity throughout much of the zone of high backscatter in the DVZ.

DVZ terrain consists of higher standing areas including some of the larger cones and ridges separated by bathymetric lows with similar but lower-relief features. The shallow volcanic zones (outlined in black on *Fig. 4.6a*) are associated with lows in the mantle Bouguer anomaly

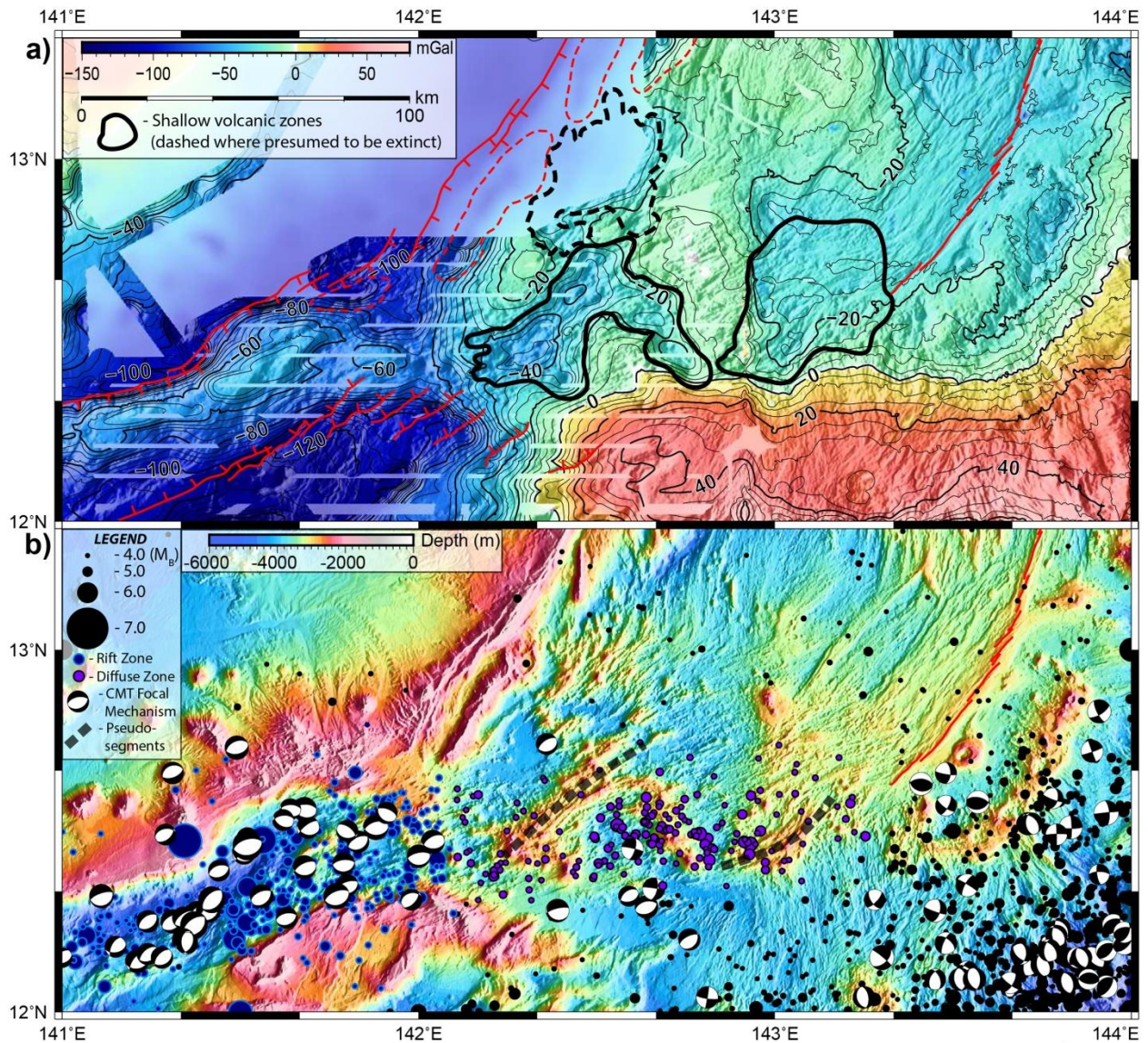


Figure 4.6: a) Mantle Bouguer anomaly map of the study area, calculated by removing the effects of 6 km-thick basaltic crust, see section 3 for details on processing. The white line indicates the boundary between positive (warm colors) and negative (cool colors) anomalies. Black outlines delineate zones of elevated volcanic topography (dashed line indicates features within the low backscatter zone in Fig. 4.5b), showing that they occur in discrete zones rather than being evenly distributed throughout the DVZ. Contour interval = 5 mGal. See section 4.4.4 for descriptions and 4.5.3 for discussion. b) Compiled bathymetry map (same as Fig. 4.4a) overlaid with seismicity data from both the ISC [International Seismological Centre, 2013] and Harvard CMT [Dziewonski et al., 1981; Ekström et al., 2012] catalogs. Blue circles indicate earthquakes within the SWMR and purple circles indicate earthquakes within the active portion of the DVZ. See legend for symbols and section 4.4.4 for analysis.

compared to the surrounding deeps, suggesting thicker crust, as expected given their more robust volcanic appearance. The pervasive lineations throughout the DVZ suggest that tectonic extension is evenly distributed, but the discrete zones of shallower magmatic seafloor fabric show that volcanism is unevenly distributed. Anomalies in the DVZ vary between relative highs

(-5 to -20 mGal, green in *Fig. 4.6a*) similar to the distal MGR flanks to slightly lower values (-20 to -50 mGal, light blue in *Fig. 4.6a*) similar to the MGR near-axis crust, suggesting that variations in crustal thickness and density are similar between the DVZ and MGR flanks. The variations in mantle Bouguer anomalies in the DVZ are generally consistent with seafloor topography, the lows correspond to regions with elevated topography and the highs correspond to the deeps.

4.4.3. MGR flank "organized spreading" morphology

Axial morphology along the southern MGR is characterized by a broad rounded axial high 2-3 km wide up to ~500-600 m above the surrounding seafloor. The axial high itself has narrow, low-relief fissures visible in the IMI-30 sidescan imagery (*Fig. 4.7a*), but any topographic offsets associated with these are below the resolution of the ship multibeam bathymetry. Farther off axis the ridge flanks are cut by axis-parallel normal faults with throws of up to ~200 m, ranging in length from ~10-50 km, resulting in seafloor fabric (*Fig. 4.4c*) that resembles abyssal hills on the flanks of a fast-spreading mid-ocean ridge [*Martinez et al., 2000*], and is the type example of what we refer to as "organized" spreading fabric (see also *Fig. 4.3*). There is a strong asymmetry in the fabric, with the vast majority of accreted crust on the gently sloping northwestern flank of the axis. *Seama and Okino* [2015] interpret this asymmetry to be, in part, due to ridge jumps to the SE. Along the NW flank, there is an abrupt transition between the abyssal hill fabric indicative of seafloor spreading and the relict tectonic rifting fabric bordering the West Mariana Ridge (*Fig. 4.4a*, cross-section C-C' on *Fig. 4.5*), indicating a distinct phase of arc tectonic rifting rapidly transitioning to organized magmatic seafloor spreading. Maps of finely gridded multibeam bathymetry alongside samples of IMI-30 backscatter imagery show organized spreading fabric (*Fig. 4.7a*), the abrupt western termination of the MGR axis (*Fig. 4.7b*), and highlight the difference between organized spreading and DVZ (*Fig. 4.7c*) morphology. The smooth, rounded high of the MGR axis (*Fig. 4.7a*) is cut by small fissures and a few normal faults with apparent throws up to ~150 m that are all aligned parallel to the axis. The western termination of the MGR axis (*Fig. 4.7b*) is abrupt and marks the boundary between axis-parallel organized spreading fabric and the variable fabric of the DVZ (*Fig. 4.7c*). The eastern half of the DVZ immediately SW of *Fig. 4.7b*, consists of a mix of volcanic cones,

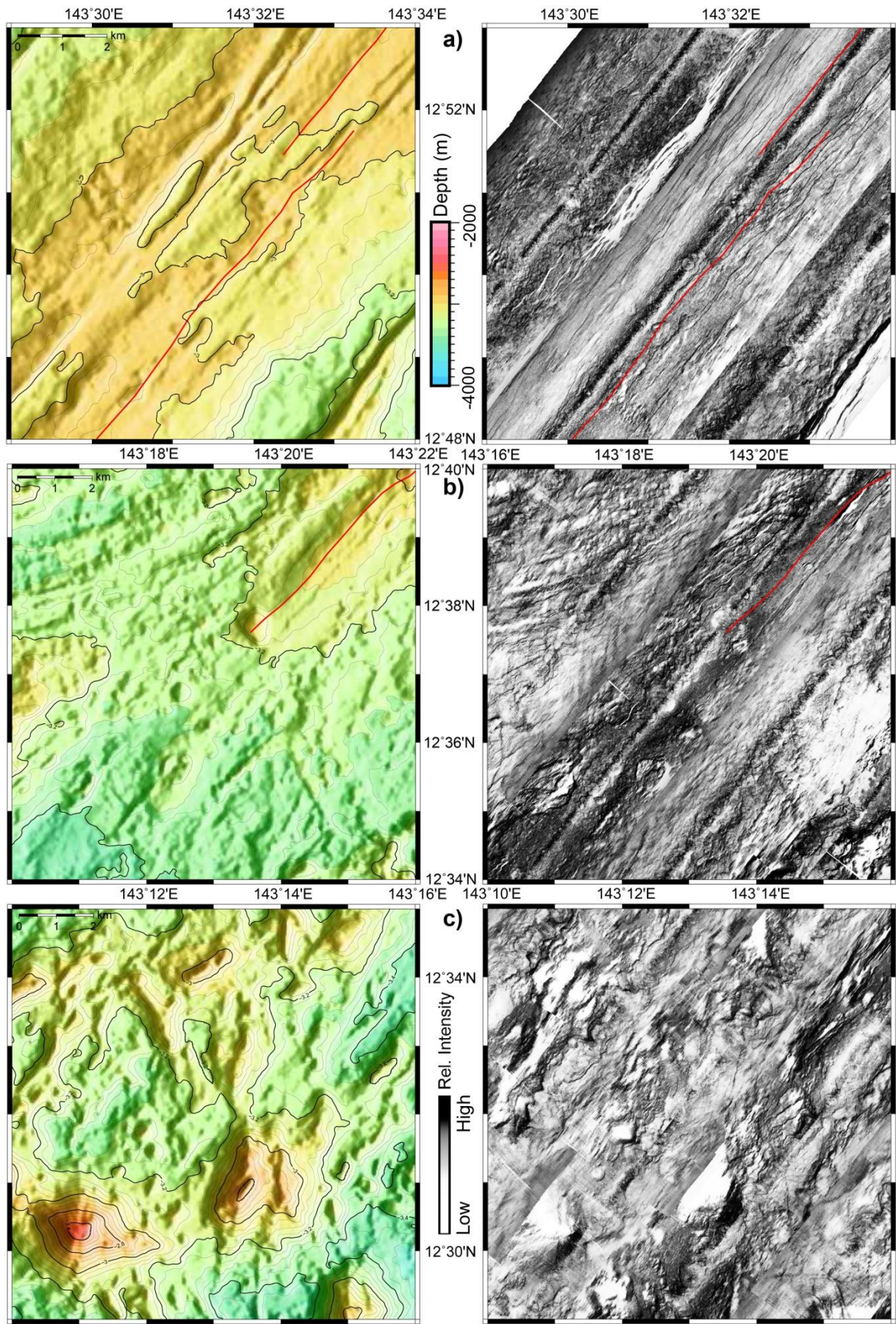


Figure 4.7: Samples of fine-scale bathymetry (0.0001° cell size) on the left side with IMI-30 backscatter imagery (0.00003° cell size) on the right. a) MGR axial morphology. Note the broad rounded axial high with small normal faults and a 3rd order segment offset. The backscatter data show fine-scale axis-parallel fissures and faults that are too small to resolve in the bathymetry data, along with hummocky volcanic textures on the axial flanks. b) The southern terminus of the MGR axis. Note the abrupt end to the axial ridge and the abrupt change in morphology from a rounded volcanic axial high to a field of small volcanic mounds with faults that are no longer sub-parallel to the axis. c) Fine-scale volcanic morphology in the eastern portion of the DVZ. Note the mixture of morphologies in the bathymetry plot, and the mixture of high-backscatter and mottled backscatter volcanic textures in the IMI-30 backscatter data, possibly indicating a mixture of volcanoclastics and effusive hummocky lava flows.

short ridges, and smaller volcanic mounds covering the seafloor (*Fig. 4.7c*), similar to that observed to the west in the rest of the DVZ.

The mantle Bouguer anomaly (*Fig. 4.6a*) varies little along the MGR and across its flanks, with values of ~-20 to -30 mGal near the axis, increasing to as high as -10 mGal within the older seafloor NW of the axis. There is a strong gradient between the negative anomalies (blues and greens) in the backarc and the positive anomalies associated with the thin forearc crust and the underlying subducting slab, which is not accounted for in the data processing. The slab is 60 to over 100 km deep in most of this area and the density contrast (~600 kg/m³) is much smaller than at the seafloor (~1700 kg/m³) so the gravity effect is small and with a long wavelength. The long wavelength slab signal may affect the absolute gravity values, but does not affect our interpretation of the much shorter wavelength backarc variations discussed above.

4.4.4. Seismicity in the southern Mariana Trough

Seismicity in the southern Mariana Trough varies among the three zones and correlates with our morphologic observations. Shallow earthquakes (≤ 50 km) with $M_B \geq 4$ (*Fig. 4.6b*) from the International Seismological Centre's (ISC) reviewed bulletin [*International Seismological Centre, 2013*], are numerous, and focal mechanisms from the Global Centroid Moment Tensor Project (CMT) Catalog [*Dziewonski et al., 1981; Ekström et al., 2012*] are distinct from east to west. From a qualitative perspective, earthquakes within the SWMR are more abundant and larger in magnitude compared to the DVZ. Furthermore, the teleseismic normal faulting events from the CMT catalog are almost exclusively limited to the SMWR. Almost all of these show approximately NNW-SSE extensional focal mechanisms. There is an abrupt decrease in the magnitude of events east of ~142°E near the transition from the SWMR to the DVZ. Events between ~142°30'E to 143°E form a cluster of increased seismicity in the central portion of the DVZ, then seismicity decreases again from 143°E to the MGR. There is no distinct seismicity

associated with the spreading axis itself and only a few small scattered events in the vicinity of the MGR axis and to the northwest, although seismicity increases dramatically in the forearc to the southeast.

In order to quantify the contrasts between SWMR and DVZ seismicity, we selected the ISC events in the SWMR (dark blue circles on *Fig. 4.6b*) and those within the active portion of the DVZ (purple circles on *Fig. 4.6b*), counted the number of events in each region, and then calculated the total moment release. In terms of total number of events (since 1900), the rift zone has 314 versus 183 in the diffuse zone, and because the regions are similar in size there is no need to normalize the number of events per unit area. The total moment release in the SWMR is 23 times greater than in the DVZ, indicating more tectonic extension in the SWMR and more magmatic extension in the DVZ, consistent with the morphologic observations. The contrast in seismicity would likely be more significant if not for the cluster of increased seismicity in the central portion of the DVZ between $\sim 142^{\circ}30'E$ to $143^{\circ}E$ (*Fig. 4.6b*). This cluster of seismicity does not easily fit into either a rifting or spreading interpretation, but regardless of the explanation for the cluster of seismicity, the regional differences in earthquake abundance and seismic moment release between the SWMR and the DVZ are clear and indicate that distinct processes are at work in each of these zones. Additionally, it is important to note that the north-south width of the seismically active part of the DSZ closely matches that of the high-backscatter zone in *Fig. 4.5b*, consistent with a broad zone of recent activity.

4.5. Discussion

Our findings for how extension occurs in the southern Mariana Trough imply a new type of spreading in backarc basins, that is distinct from rifting because new crust and lithosphere are formed, but is also distinct from organized spreading because crustal accretion appears to occur over a broad region rather than along a narrow spreading axis. To show this, we summarize observations of rifting and spreading in the southern Mariana Trough, then discuss an alternative rifting model used to explain a similar region south of Valu Fa Ridge in the Lau Basin, and consider how diffuse or organized the spreading may be in the DVZ. Then we present a conceptual model to explain our observations and schematically illustrate our hypothesis, and

finally consider what the morphologic evidence suggests about how melt is produced in the DVZ.

4.5.1. Summary of observations on the mode of opening in the southern Mariana Trough

Contrasts in seafloor morphology and seismicity between the SWMR, the DVZ, and MGR flanks discussed in the previous section provide strong evidence that each zone is controlled by distinct extensional processes. The SWMR is characterized by tectonic rift-type morphology, with a deep largely amagmatic rift valley bounded by normal faults with scarp heights of up to 3500 m that progressively down-drop basement blocks to the valley floor. Abundant seismicity and normal fault focal mechanisms (*Fig. 4.6b*) indicate ongoing tectonic extension as a primary mode of opening. Relict rift fabric extends northward in a narrow band along the eastern flank of the West Mariana Ridge, suggesting that a similar rifting process characterized the first phase of Mariana Trough opening. Seismicity (with magnitudes of at least 4.0) decreases markedly within the DVZ both in terms of abundance and total moment release, and the morphology is characterized by a mix of closely spaced volcanic features from cones to ridges, forming deeps and highs separated by gradational topographic transitions, rather than by large offset fault blocks. None of the characteristic features of rifting are observed in the DVZ, the topographic ridges are much smaller, more closely spaced, and appear to be largely volcanic based on their morphology. No fault blocks are observed in the bathymetry or gravity data, and the seismically active zone is associated with high acoustic backscatter that is indicative of relatively recent tectonic and volcanic activity. Furthermore, seafloor depth in the DVZ is shallower than the SWMR, is shallower than most of the terrain that borders the rifted margin of the West Mariana Ridge, and it varies in broader undulations associated with volcanic constructional features. DVZ fabric extends northwestward all the way to the narrow band of rift-type fabric along the West Mariana Ridge margin, indicating a relatively short rifting phase that abruptly transitioned into the process that remains active today. This suggests that the active process here is not a transitional phase between rifting and spreading, but rather a stable mode of extension. MGR flank morphology is characterized by shallower abyssal hill-type fabric, consistent with backarc spreading magmatically enhanced by capture of hydrous arc magmas because of proximity to the arc volcanic front [*Becker et al., 2010; Martinez et al., 2000*]. The characteristic MGR flank seafloor spreading fabric extends northwestward to the narrow band of

rift fabric along the West Mariana Ridge, indicating that here rifting rapidly transitioned to organized seafloor spreading along the MGR, which remains active today. Along most of the eastern margin of the West Mariana Ridge the seafloor is deep, isostatically indicating thin crust, before the transition to organized spreading takes place and magmatic accretion causes the seafloor to thicken and shallow somewhat again. A rapid transition from rifting to organized spreading appears to be the norm in backarc basins, as is observed in the northern Mariana Trough at 22°N [Yamazaki *et al.*, 2003], where a broad rift had been inferred previously based on low-resolution data [Martinez *et al.*, 1995].

4.5.2. Diffuse spreading vs. segmented rifting

We interpret the DVZ as a zone of diffuse spreading where new crust is emplaced in a broad region that varies from ~20 to 50 km wide. One of the few known regions with analogous tectonic and volcanic features is the Havre Trough in the southwest Pacific, the southern continuation of the Lau backarc basin. Spreading in the southern half of the Lau Basin is accommodated along the Eastern Lau Spreading Center and its southern extension, Valu Fa Ridge (VFR). VFR is analogous to the MGR in terms of morphology, opening rate, arc proximity, crustal seismic velocity structure [Dunn and Martinez, 2011; Sato *et al.*, 2015], abundance of andesitic lavas and geochemical indicators of subduction influence [Jenner *et al.*, 1987; Masuda and Fryer, 2015]. VFR forms an inflated magmatic axial high varying in separation with the Tofua arc volcanic front from ~50 to 30 km southward and spreading rates vary from ~69 to 47 mm/yr [Sleeper and Martinez, 2016]. The volcanic ridge defining the VFR axis abruptly terminates at ~22°45'S and is replaced by a zone of volcanism and tectonism ~20-50 km wide and ~100 km long, characterized by a mixture of volcanic cones, short volcanic ridges, and shallow grabens [Martinez and Taylor, 2006; Watanabe *et al.*, 2010] similar to those observed in the DVZ. Slab depths vary between ~100-150 km and the adjacent arc volcanic front shows evidence of extensional deformation, again similar to the southern Mariana Trough. The seafloor volcanism is also characterized by lavas with strong arc affinities [Haase *et al.*, 2009] like those few we have sampled in the southern Mariana Trough [Becker, 2005; Pearce *et al.*, 2005; Brounce *et al.*, 2014]. South of the Lau Basin "ridges and knolls" terrain there is a broad backarc basin (Havre Trough) rather than a narrow rift valley like the SWMR. The rift margins representing the initial opening phase are ~150 km apart, and the seismicity is more diffuse than

the SWMR. Analogous patterns in seafloor morphology between backarc extensional systems from two entirely different convergent margins suggest that a common process may be responsible. *Martinez and Taylor* [2006] interpreted the region south of VFR and zones of similar fabric identified in the Lau Basin to be “diffuse patches of seafloor spreading,” where magmatic accretion accommodates extension, consistent with our interpretation for the DVZ. However, *Fujiwara et al.* [2001] interpreted the region south of VFR to be in a magmatic phase of rifting, where volcanism is fed by intrusions along rift-related faults, to which they gave the term “segmented rifting.”

The segmented rifting model has not been specifically applied to the southern Mariana Trough, but based on the similarities in morphology and tectono-magmatic conditions, it is a viable alternative to our interpretation of diffuse spreading and thus must be addressed. Segmented rifting is also analogous to the *Becker* [2005] interpretation that the DVZ is actively rifting, but that arc melts intrude the rifted blocks and accrete new crust. A similar model has also been applied to the southern Havre Trough, where volcanism across the backarc is inferred to be fed by magmatic intrusion of rifted arc crustal blocks [*Wysoczanski et al.*, 2010]. In the case of the southern Mariana Trough there is one critical observation that effectively eliminates the rifting interpretation. It is generally agreed and consistent with morphologic and geophysical observations [*Seama and Okino*, 2015] that the entire ~100+ km-wide zone of abyssal hill fabric along the MGR flanks is magmatic crust spread from the MGR. The zone of DVZ fabric immediately west of the MGR is also >100 km wide, tapering down toward the SWMR. Thus, a rift interpretation would juxtapose two terrains created by fundamentally different processes, rifting to the west and organized spreading to the east, which should create an observable tectonic boundary or morphologic discontinuity between the two different types of lithosphere. No such tectonic boundary is observed, not even a poorly defined fault zone. Rather, the transition is marked by a change in seafloor fabric from more abyssal hill-like fabric flanking the MGR to a more finely lineated “ridges and knolls” terrain in the DVZ over a gradational transition zone ~10 km wide. This indicates a transition in mode of magmatic spreading (focused to diffuse), but is not consistent with a transition from tectonic rifting to magmatic spreading. Further, the segmented rifting model would also juxtapose older, thicker fault blocks with younger volcanism and potentially new crust and we would therefore expect to see evidence of thick, lower density blocks in the mantle Bouguer anomaly data, like the mapped blocks along

the WMR that are associated with -20 to -30 mGal anomalies relative to the surrounding seafloor (see *Fig. 4.6a*). Instead we observe Bouguer lows under the shallow volcanic terrain (outlined in black in *Fig. 4.6a*) and Bouguer highs under the deeper seafloor, consistent with variations in crustal thickness due to volcanic processes. However, although we consider it highly unlikely due to the finely lineated structure of the DVZ, we cannot rule out the possibility that small (~5 km wide or less) slivers of older rifted crust exist that may not show up in the gravity data, which has a grid cell size of ~270 m. The existence of slivers of pre-existing crust may seem to blur the distinction between rifting and spreading, but the critical aspect here is the active process that accommodates the extension. Once mechanically weak zones of magmatic crustal accretion are formed any slivers of pre-existing colder, thicker, and stronger lithosphere are unlikely to continue to deform. Thus, the process should still be considered spreading even if pre-existing slivers are interspersed between zones of accretion, because new crust and lithosphere are still being formed to accommodate extension and any pre-existing material forms passive inclusions and do not accommodate extension by themselves deforming.

Another logical argument against rifting is the width of the DVZ compared to the SWMR. If the crust in the DVZ is rifted, then the initially ~20 km wide block of arc crust at the base of the SWMR graben would have to be stretched to as much as 100 km without accreting any new crust. Presumably, there is a certain limit that the pre-existing material could be stretched before new crust must be accreted or mantle is exposed. There is no evidence of large-scale detachment faults, mullions, or mantle exposures within the DVZ, thus this implies that new crust must be forming to accommodate the extension of the basin. While the abrupt decrease in seismicity between the SWMR and the DVZ indicates a decrease in tectonic deformation, the increased seismicity in the DVZ relative to the MGR could be interpreted as consistent with a magmatic mode of rifting like that hypothesized in the segmented rifting model. However, the increased seismicity is also consistent with a diffuse form of spreading. If crust is accreted along short spreading axes throughout the DVZ, the crust surrounding the zones of magmatic accretion would have to accommodate the strain tectonically, resulting in increased seismicity relative to organized spreading where extension is accommodated magmatically along a narrow boundary. It is also possible that the increased seismicity may be related to forearc deformation extending into the DVZ, and thus the seismicity could be partly reflecting trench-parallel forearc extensional processes. We noted previously that where spreading is organized along the MGR,

forearc extension is decoupled by the axis and does not affect the trailing part of the Philippine Sea plate. Within the DVZ, however, the decoupling may be less complete and trench-parallel extension may bleed into this zone, as there is no sharp plate boundary zone. Lastly, if the volcanic ridges are produced by intrusion along fault blocks of arc crust, there should be asymmetry in seafloor depth on either side of the ridge, wherein the footwall side is elevated relative to the hanging wall, and this asymmetry is not observed (see cross-section B"-B'" in *Fig. 4.5*). This is consistent with volcanic eruptions occurring along opening-mode fissures and fractures typical of spreading axes rather than along normal faults with vertical offset.

4.5.3. Diffuse spreading vs. organized spreading

The observations presented herein favor the interpretation of the DVZ as a zone of spreading where new crust is accreted, but there is some uncertainty as to how diffuse or organized it is. The similar ~20-50 km widths of the zone of high backscatter and seismicity support the interpretation that the entire zone is active, but without analyses of volcanic samples throughout the region, including radiometric ages, we cannot say anything more definitive than that the seismically active high backscatter zone is generally more recently active than the low backscatter zones to the north and south. The few lava sample analyses we have indicate some recent activity at both the western [*Becker, 2005; Pearce et al., 2005*] and eastern [*Brounce et al., 2014*] ends of the DVZ (*Fig. 5b*). The lava samples with intact glass [*Masuda et al., 2006*] (*Fig. 5b*) are consistent with relatively recent volcanism, but the lack of analyses on these samples leaves the open question of how recent it is, and the limited distribution means that these samples may not be representative of all of the DVZ. Thus, it is difficult to say for certain whether new crust is accreting across the entire width of the DVZ essentially contemporaneously, or if there is some degree of focusing or organization toward a spreading axis. The main observation in favor of some degree of organization are the elongate topographic highs that we term here pseudo-segments marked in *Fig. 6b*. The NW pseudo-segment is defined by a shallow ridge ~10 km wide and ~50 km long dotted with volcanic cones, trending in a NE-SW direction. The SE pseudo-segment is poorly defined in comparison, and is dominated by a broad crescent-shaped ridge. This ridge terminates by ~143°07'E, and there is a gap of ~20 km between the ridge and the MGR terminus, within which there is no clear continuation of this feature. One of the most striking contrasts between DVZ morphology and the MGR flanks are

the lack of small seamounts on the MGR flanks and their prevalence within the DVZ. The presence of these cones is consistent with volcanism fed by small batches of melt erupting throughout the DVZ, but if they exist beneath the MGR they are mostly homogenized in a continuous sub-axial magmatic system [Becker *et al.*, 2010] so that they do not erupt as individual cones. This indicates a lack of such homogenization in the DVZ and a very different accretionary process than along the MGR. Thus, the argument for the existence of spreading segments here is relatively weak, but without more information the possibility cannot be ruled out. If these segments indeed exist and represent some degree of focusing of crustal accretion within the DVZ, then the cluster of increased seismicity between 142°30'-143°E (*Fig. 6b*) could be explained as tectonic deformation in the overlap zone between these two segments. While this is an appealing argument to explain the cluster of seismicity, we are not confident in defining spreading segments here based on the available information. Instead, we favor the interpretation that the pseudo-segments and other high-standing volcanic features are the volcanic expression of the 3-D pattern of buoyant upwelling of hydrous melts in the mantle wedge, an idea that is explored further in 4.5.5.

4.5.4. *Hydrous lithosphere model*

The consistencies between the zones of hypothesized diffuse spreading in the southern Mariana Trough and the southern Lau Basin provide some indications of the tectono-magmatic conditions needed for diffuse spreading to occur. First, both zones lie near the expected locus of the arc volcanic front with slab depths of ~60-150 km indicating that high mantle water content and resultant flux melting might play a role. Second, both systems convert from diffuse to organized spreading as opening rates increase above ~45 mm/yr, suggesting that opening rate also might be important. In order to understand the significance of the interplay between opening rate and mantle water content, it is instructive to compare these backarc environments with a typical mid-ocean ridge (MOR), where the axis advects drier mantle. At MORs, the small amount of mantle water [Kelley *et al.*, 2006] is extracted into the melt, dehydrating the residual mantle. Magmatic dehydration greatly increases the viscosity and strength of the residual mantle [Karato, 1986; Hirth and Kohlstedt, 1996]. The abrupt increase in viscosity of this "compositional lithosphere" [Phipps Morgan, 1997] is thought to help focus the melt from a broad ~200 km wide zone of melt generation toward a narrow neovolcanic zone at the surface

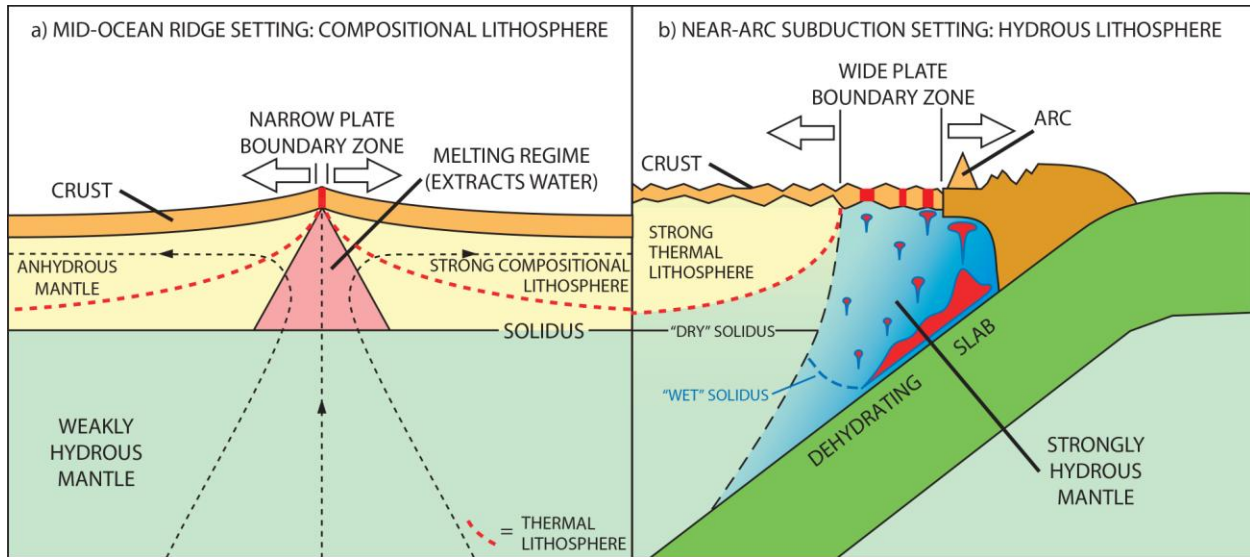


Figure 4.8: a) Simplified conceptual cross-section through a typical mid-ocean ridge, based on the compositional lithosphere model of Phipps Morgan [1997]. Melting and melt extraction within the sub-ridge melting regime dehydrates the residual mantle and creates a dry and strong compositional lithosphere that helps to focus melt and deformation to a narrow plate boundary zone. b) Simplified conceptual depiction of the hydrous lithosphere model [Martinez et al. 2012], showing a cross-section through a subduction zone with active near-arc extension analogous to the southern Mariana Trough DVZ. The dehydrating slab continually adds water to the overlying mantle and lithosphere, so that even though mantle melting occurs residual mantle retains significant water [Hirth and Kohlstedt, 2003] and a strong compositional lithosphere cannot form. Deformation and volcanism cannot focus and are distributed in a broad plate boundary zone. Thick red bars in the crust depict distributed volcanism, red dashed line shows the base of the thermal lithosphere, red blob and diapirs schematically depict hydrous melt, other features are labeled. The blue gradient within the mantle wedge represents increasing mantle water content toward the arc, and the dashed black line marks the hypothesized sharp boundary between a strongly hydrous mantle wedge and less hydrous mantle away from the arc [Dunn and Martinez, 2011; Sleeper and Martinez, 2014] discussed in Chapter 1 in relation to Fig. 1.1. See 4.5.4 for discussion.

(Fig. 8a) [Braun et al., 2000; Key et al., 2013]. In our "hydrous lithosphere" model (Fig. 4. 8b) [Martinez et al., 2012], the continuous flux of water into the mantle wedge near the arc volcanic front inhibits dehydration of the residual mantle and opposes the viscosity increase, and instead produces a broad zone of weak hydrous lithosphere. A simple way to conceptualize the process is as a balance between the rate of water influx from the subducted slab and the rate of mantle lithospheric dehydration by melting. Increasing opening rates increase upwelling and melting and thus increase the rate of water extraction from the mantle, whereas increasing water flux from the slab acts to increase lithospheric hydration. As long as water flux remains high and opening rates remain low, then the process of diffuse spreading is likely to continue and therefore not become organized. The ultra-slow opening Havre Trough south of the Lau Basin may be a steady state example of diffuse seafloor spreading [Martinez et al., 2013].

4.5.5. Melt production within the DVZ: passive plate-driven melting vs. active buoyancy-driven melting

The distribution and morphologic variety of volcanic features within the DVZ implies local variability in both melt production and tectonic extension, and provides insight into the primary mechanism of melt generation. At arc-proximal backarc spreading centers, melt is generated both from passive plate-driven upwelling and decompression melting similar to that beneath MORs and from active buoyant upwelling due to hydrous melts generated by flux melting above the subducting slab [Kelley *et al.*, 2006; Martinez and Taylor, 2006]. The relative contribution of plate-driven upwelling and melting depends on the opening rate, and the relative contribution of buoyant upwelling and hydrous flux melting varies primarily with proximity to the arc volcanic front. Passive plate-driven upwelling dominates along arc-distal spreading centers, and at fast opening rates. Buoyant upwelling becomes increasingly important as the spreading axis approaches the arc volcanic front, where water flux and flux melting are greatest, and as opening rates decrease [Sleeper *et al.*, 2016]. Thus, in arc-proximal settings there can be contributions to melt production from both plate-driven and hydrous buoyant upwelling processes, whereas in arc-distal settings only the plate-driven component remains and the axes resemble MORs at similar spreading rates.

In the southern Mariana Trough, both the southern end of the MGR and the DVZ overlie slab depths typically associated with arc volcanism, sampled lavas show strong affinities to the arc volcanoes [Becker, 2005; Pearce *et al.*, 2005; Brounce *et al.*, 2014], and minimum magmatic water contents range between ~1.5-2% [Brounce *et al.*, 2014]. This indicates abundant hydrous flux melt production and buoyant upwelling within the underlying mantle wedge. Meanwhile, plate-driven upwelling presumably decreases with opening rates westward as the basin narrows ultimately to the width of the SWMR. In addition, the distributed nature of crustal accretion and the broad zone of active extension here may prevent a focused two-dimensional upwelling zone from developing, and thus further reduce overall plate-driven upwelling. As discussed in 4.4.2 the shallow volcanic terrain is organized into discrete irregular zones rather than distributed across the DVZ (outlined in black in *Fig. 4.6a*), whereas the lineations that indicate tectonic extension are more uniformly distributed. If plate-driven upwelling and melting were dominant, volcanism should be more evenly distributed throughout the region, and we would not expect

discrete zones of increased volcanism. Further, if there is no organized spreading center to focus mantle advection and melts, individual mantle upwelling instabilities (diapirs) probably source the melts that give rise to the distinctly shallower volcanic zones, resulting in variations in crustal thickness and depth. If there is a broad zone of weak, hydrous lithosphere, then these diapirs might be able to intrude and erupt throughout the DVZ. In this way, the irregular shape of the shallow volcanic zones might be a direct reflection of the three-dimensional pattern of buoyant upwelling in the mantle wedge.

4.6. Conclusions

Extensional processes at divergent plate boundaries are generally classified as either rifting or spreading. In rifting, extension is primarily accommodated by thinning and deformation of pre-existing lithosphere, sometimes accompanied by magmatic intrusion along normal faults that feeds volcanism within the rift graben. In spreading, extension is primarily accommodated by magmatic accretion of new crust and formation of new lithosphere, along with a component of tectonic extension of the new lithosphere. At both MORs and backarc spreading centers, volcanism and deformation of the newly accreted crust is typically limited to a narrow axial neovolcanic zone a few km wide. This study describes a new mode of crustal accretion that we call “diffuse spreading,” where the zone of active deformation, crustal accretion, and volcanism is ~20-50 km wide. We propose that the DVZ, a ~120 km-long region in the southern Mariana Trough between the southern terminus of the MGR and the SWMR to the west was formed by diffuse spreading. DVZ seafloor morphology is characterized by a distinctive mixture of volcanic cones and ridges that is unlike rifting and is also unlike the typical abyssal hill fabric associated with organized spreading. Similar seafloor fabric has also been identified in the Lau-Havre backarc system, however, suggesting that diffuse spreading occurs in other backarc basins, although it was interpreted as a form of rifting in that case [*Fujiwara et al.*, 2001; *Watanabe et al.*, 2010; *Wysoczanski et al.*, 2010]. The key to creating and maintaining a broad zone of weak hydrous lithosphere is the continuous flux of water from the underlying subducted slab that counteracts mantle dehydration through melting, and thus we would not expect diffuse spreading outside of a convergent margin setting. Spreading rate also appears to be a factor, as it exerts primary control on the rate of upwelling and melting, and thus the rate of water extraction

from the mantle. As long as the water flux from the slab and the rate of extraction due to melting remain within some threshold, diffuse spreading will continue, although the water flux is likely to diminish away from the trench as a backarc basin widens and the zone of spreading is increasingly removed from the subducted slab and its water flux.

Diffuse spreading is not a transitional phase from rifting to organized spreading, but rather a distinct class of seafloor spreading associated with particular tectono-magmatic conditions in backarc basins. In addition to the DVZ in the southern Mariana Trough, parts of the Havre Trough south of the Lau Basin may represent steady-state examples. We consider the phenomenon of generally diffuse volcanism for the DVZ, as a whole, to be more consistent with the model of a highly water-saturated suprasubduction-zone mantle beneath this area. More detailed exploration and analysis of samples from the area is needed to elucidate the precise nature of response to extension in this part of the Mariana Trough. One question is whether the entire zone is simultaneously active or whether activity jumps from one short-lived structure to another over time, which could be addressed by collecting and dating more volcanic samples from throughout the DVZ. Seismic reflection and refraction along with magnetotelluric surveys would also be helpful in understanding the structure of the hydrous crust and lithosphere, which we can only generally describe in a conceptual model (*Fig. 4.8b*) using the available data. The results of this study provide a first step toward wider recognition of the diffuse spreading process that will hopefully spur further investigations in the future.

CHAPTER 5: CONCLUSIONS

This dissertation has explored the interactions of plate-driven and mantle-driven processes in backarc basins and how they influence the geologic, geophysical, and geochemical characteristics of extensional systems, the mode of crustal accretion, and basin evolution. Chapter 2 describes analogous morphologic and geophysical variations with arc proximity along the Fonualei Rift and Spreading Center (FRSC) and the southern branch of the Mangatolu Triple Junction (MTJ-S) as those observed along other backarc spreading centers that vary in proximity to the arc volcanic front. These trends reflect the varying contribution of mantle-driven hydrous flux melting and subduction-related effects on mantle wedge rheology and flow patterns. The southern segments of the FRSC represent an exception to the trends observed elsewhere. Located ~25-50 km from the Tofua arc volcanic front and spreading at ultraslow rates (~8-14 mm/yr), they demonstrate how the spreading center responds when plate-driven upwelling and decompression melting is minimized and mantle-driven hydrous flux melting and buoyant upwelling is maximized. The axis preferentially expresses the inherently three-dimensional structure of buoyant upwelling by forming distinct isolated volcanic cones unlike the shallow volcanic ridge of the segments to the north. This morphologic change is analogous to that observed along ultraslow MORs, but the high water flux from the subducting slab greatly enhances melting relative to weakly magmatic ultraslow MORs. This study represents the first detailed description of ultraslow spreading in the backarc environment, which may aid in the interpretation of similar morphologies in other backarc basins and in clarifying the transition from arc rifting to the earliest phase of seafloor spreading.

Chapter 3 presents a revised kinematic model describing the current relative motions between the three primary plates in the Lau Basin: the Australian Plate to the west, the Tonga Plate to the east, and the Niuafu'ou microplate that lies between them in the northern half of the basin. It builds upon the three-plate model of *Zellmer and Taylor* [2001], resolving some discrepancies in that model while still satisfying geologic, geophysical, and geodetic constraints. The results provide insight into how opening geometry and non-rigid behavior influences the evolution of the various plate boundaries and the basin as a whole. The Lau Basin is opening in a zipper-like manner from north to south, causing the extensional stresses to rotate as opening proceeds. This leads to increasing opening rates over time, propagating and reorganizing plate

boundaries, migrating Euler poles, and rotating vectors of plate motion. These departures from standard rigid-plate tectonics and Eulerian rotations over time suggest that models using these assumptions should only be used to describe motions over relatively short time periods of hundreds of thousands of years at most. This study also provides valuable kinematic and geologic information that will aid future studies in the Lau Basin and other backarc basins,

Chapter 4 describes a new mode of magmatic seafloor spreading called diffuse spreading, facilitated by a particular balance between plate-driven and mantle-driven processes. We interpret diffuse spreading to occur in the ~120 km long region between the southern terminus of the Malaguana-Gadao Ridge, a backarc spreading center in the southern Mariana Trough, and the Southwest Mariana Rift, a zone of active arc rifting to the west. It is characterized by a broad zone (~20-50 km across) of volcanism and magmatic crustal accretion cut by closely-spaced faults, in contrast to the typical narrow plate boundary zone at MORs and BASCs. Seafloor fabric is characterized by a mix of volcanic cones, short volcanic ridges, and deeps, with pervasive trench-normal lineations. The region overlies slab depths typical of the arc volcanic front and sparse volcanic samples show strong similarities to arc lavas and elevated water contents, indicating abundant water flux from the subducting slab. The continuous water flux opposes dehydration during melting, creating a broad zone of weak hydrous lithosphere on top of which new crust is magmatically accreted. As long as the balance between plate-driven melting and dehydration and water flux from the slab remains within some threshold, diffuse spreading should continue. Thus, it is not simply a transitional phase between rifting and spreading, but rather a distinct mode of magmatic crustal accretion associated with arc-proximal extension in subduction zones.

REFERENCES

- Ahlgren, S. G. (1999), The nucleation and evolution of Riedel shear zones as deformation bands in porous sandstone, *M.S. Thesis, University of Arizona*, May 1999.
- Arculus, R. A. (2004), NoToVE-2004 (Northern Tonga Vents Expedition) Submarine hydrothermal plume activity and petrology of the northern Tofua Arc, Tonga, *Voyage Summary SS11/2004*, Marine National Facility, Hobart, Tasmania, Australia.
- Becker, N. C. (2005), Recent volcanic and tectonic evolution of the southern Mariana arc, PhD dissertation, Univ. of Hawai'i at Mānoa, May 2005.
- Becker, N. C., P. Fryer, and G. F. Moore (2010), Malaguana-Gadao Ridge: Identification and implications of a magma chamber reflector in the southern Mariana Trough, *Geochem. Geophys. Geosyst.*, *11*, Q04X13, doi:10.1029/2009GC002719.
- Bevis, M. (1988), Seismic slip and down-dip strain rates in Wadati-Benioff zones. *Science*, *240*, 1317-1319.
- Bevis, M., F. W. Taylor, B. E. Schutz, J. Recy, B. L. Isacks, S. Helu, R. Singh, E. Kendrick, J. Stowell, B. Taylor, and S. Calmant (1995), Geodetic observations of very rapid convergence and backarc extension at the Tonga arc, *Nature*, *374*, 249-251.
- Bevis, M. (1997), Geodetic measurements in the Tonga-Lau arc system (abstract), *Eos Trans. AGU*, *78*, 697-698.
- Billen, M., and M. Gurnis (2001), A low viscosity wedge in subduction zones, *Earth Planet. Sci. Lett.*, *193*, 227-236.
- Braun, M. G., G. Hirth, and E. M. Parmentier (2000), The effects of deep damp melting on mantle flow and melt generation beneath mid-ocean ridges, *Earth and Planet. Sci. Lett.*, *176*(3-4), 339-356.

- Brounce, M. N., K. A. Kelley, and E. Cottrell (2014), Variations in $\text{Fe}^{3+}/\Sigma\text{Fe}$ of Mariana arc basalts and mantle wedge $f\text{O}_2$, *J. Petrology*, *55*(12), 2513-2536, doi:10.1093/petrology/egu065.
- Brounce, M. N., K. A. Kelley, R. J. Stern, F. Martinez, and E. Cottrell (2016), The Fina Nagu Volcanic Complex: Unusual submarine arc volcanism in the rapidly deforming southern Mariana margin, *Geochem. Geophys. Geosyst.*, *17*, doi:10.1002/2016GC006457.
- Brune, S., A. A. Popov, and S. V. Sobolev (2012), Modeling suggests that oblique extension facilitates rifting and continental break-up, *J. Geophys. Res.*, *117*, B08402, doi:10.1029/2011JB008860.
- Buck, W. R. (1991), Modes of Continental Lithospheric Extension, *J. Geophys. Res. Solid Earth*, *96*(B12), 20,161-20,178.
- Canales, J. P., J. J. Dañobeitia, R. S. Detrick, E. E. E. Hooft, R. Bartolomé, D. F. Naar (1997), Variations in axial morphology along the Galápagos spreading center and the influence of the Galápagos hotspot, *J. Geophys. Res.*, *102*, 27341-27354.
- Canales, J. P., G. Ito, R. S. Detrick, and J. Sinton (2002), Crustal thickness along the western Galapagos Spreading Center and the compensation of the Galapagos hotspot swell, *Earth Planet. Sci. Lett.*, *203*, 311-327, doi:10.1016/0012-821X(94)90137-6.
- Cande, S. C., and D. V. Kent (1995), Revised calibration of the geomagnetic polarity time scale for the Late Cretaceous and Cenozoic, *J. Geophys. Res.*, *100*, 6093-6095.
- Caress, D. W., and D. N. Chayes (2006), MB-System: Mapping the Seafloor, <http://www.mbari.org/data/mbsystem> and <http://www.ldeo.columbia.edu/res/pi/MB-System>.
- Chase, C. G. (1978), Extension behind island arcs and motions relative to hot spots, *J. Geophys. Res.*, *83*, 5,385-5,387.

- Cherkis, N.Z. (1980), Aeromagnetic investigations and seafloor spreading history in the Lau Basin and northern Fiji Plateau, *SOPAC Tech. Bull.*, 3, 37-45.
- Choblet, G., and Parmentier, E. M. (2001), Mantle upwelling and melting beneath slow spreading centers: effects of variable rheology and melt productivity, *Earth Planet. Sci. Lett.*, 184(3-4), 589-604.
- Conder, J. A., and D. A. Wiens (2011), Shallow seismicity and tectonics of the central and northern Lau Basin, *Earth Planet. Sci. Lett.*, 304, 538-546.
- Dewey, J. F. (1980), Episodicity, sequence, and style at convergent plate boundaries, in *The Continental Crust and Its Mineral Deposits*, edited by D.W. Strangway, Geol. Assoc. of Can., Waterloo, Ontario, 554-573.
- Dick, H. J. B., J. Lin, and H. Schouten (2003), An ultraslow-spreading class of ocean ridge, *Nature*, 426, 405-412.
- Dunn, R., and F. Martinez (2011), Contrasting crustal production and rapid mantle transitions beneath backarc ridges, *Nature*, 469, 198-202, doi:10.1038/nature09690.
- Dziewonski, A. M., T.-A. Chou, and J. H. Woodhouse (1981), Determination of earthquake source parameters from waveform data for studies of global and regional seismicity, *J. Geophys. Res.*, 86, 2825-2852.
- Eguchi, T., T. Fujinawa, and M. Ukawa (1989), Microearthquakes and tectonics in an active backarc basin: The Lau Basin, *Phys. Earth Planet. Inter.*, 56, 210-229.
- Elsasser, W. M. (1971), Sea-floor spreading as thermal convection, *J. Geophys. Res.*, 76, 1,101-1,112.
- Ekström, G., M. Nettles, and A. M. Dziewonski (2012), The global CMT project: 2004-2010: Centroid-moment tensors for 13,017 earthquakes, *Phys. Earth Planet. Inter.*, 200-201, 1-9, doi:10.1016/j.pepi.2012.04.002.
- Escrig, S., A. Bézous, S. L. Goldstein, C. H. Langmuir, and P. J. Michael (2009), Mantle source variations beneath the Eastern Lau Spreading Center and the nature of subduction

- components in the Lau basin Tonga arc system, *Geochem. Geophys. Geosyst.*, *10*, Q04014, doi: 10.1029/2008GC002281.
- Escrig, S., A. Bézoz, C. H. Langmuir, P. J. Michael, and R. Arculus (2012), Characterizing the effect of mantle source, subduction input and melting in the Fonualei Spreading Center Lau Basin: Constraints on the origin of the boninitic signature of the backarc lavas, *Geochem. Geophys. Geosyst.*, *13*, Q10008, doi:10.1029/2012GC004130.
- Falloon, T. J., A. Malahoff, L. P. Zonenshain, and Yu. A. Bogdanov (1992), Petrology and geochemistry of backarc basin basalts from Lau basin spreading ridges at 15°, 18°, and 19°S, *Mineral. Petrol.*, *47(1)*, 1-35.
- Fryer, P., and D. M. Hussong (1981), Seafloor spreading in the Mariana Trough: Results of Leg 60 drill site selection surveys. In *Initial Reports of the Deep Sea Drilling Program, Leg 60*, edited by D.M. Hussong, and S. Uyeda, et al., pp. 45-55, US Government Printing Office, Washington DC.
- Fryer, P., H. Fujimoto, M. Sekine, L.E. Johnson, J. Kasahara, H. Masuda, T. Gamo, T. Ishii, M. Ariyoshi, and K. Fujioka (1998), Volcanoes of the southwestern extension of the active Mariana island arc: New swath-mapping and geochemical studies, *Island Arc*, *7*, 596-607.
- Fryer, P., N. Becker, B. Applegate, F. Martinez, M. Edwards, and G. Fryer (2003), Why is the Challenger Deep so deep?, *Earth Planet. Sci. Lett.*, *211*, 259-269, doi:10.1016/S0012-821X(03)00202-4.
- Fujiwara, T., T. Yamazaki, and M. Joshima (2001), Bathymetry and magnetic anomalies in the Havre Trough and southern Lau Basin: from rifting to spreading in backarc basins, *Earth Planet. Sci. Lett.*, *185*, 253-264.

- German, C. R., E. T. Baker, D. P. Connelly, J. E. Lupton, J. Resing, R. D. Prien, S. L. Walker, H. N. Edmonds, and C. H. Langmuir (2006), Hydrothermal exploration of the Fonualei Rift and Spreading Center and the Northeast Lau Spreading Center, *Geochem. Geophys. Geosyst.*, 7, Q11022. doi:10.1029/2006GC001324.
- Goodliffe, A. M. (1995), Preliminary Cruise Report Hakurei Maru No. 2, Lau Basin, Leg 1, SOPAC Cruise Report 144, Suva, Fiji, 12.
- Govers, R., and M. J. R. Wortel (2005), Lithosphere tearing at STEP faults: Response to edges of subduction zones, *Earth Planet. Sci. Lett.*, 236, 505-523.
- Haase, K. M., S. Fretzdorff, R. Mühe, D. Garbe-Schönberg, P. Stoffers (2009), A geochemical study of off-axis seamount lavas at the Valu Fa Ridge: Constraints on magma genesis and slab contributions in the southern Tonga subduction zone, *Lithos*, 112, 137-148, doi: 10.1016/j.lithos.2009.05.041.
- Hamburger, M. W., and B. L. Isacks (1988), Diffuse backarc deformation in the southwestern Pacific, *Nature*, 332, 599-604.
- Hawkins, J. W. (1977), Petrologic and geochemical characteristics of marginal basin basalts, in Hayes, D.E. ed. *Island arcs, deep sea trenches, and backarc basins*, AGU Geophysical Monograph Series, 23, Washington, DC, 355-365.
- Hawkins, J. W. (1994), Petrologic Synthesis: Lau Basin Transect (Leg 135), in *Proceedings of the Ocean Drilling Program Leg 135, Scientific Results*, edited by J. Hawkins, et al., pp. 879–905, Ocean Drilling Program, College Station, TX.
- Hawkins, J. W., and J. T. Melchior (1985), Petrology of Mariana Trough and Lau Basin basalts, *J. Geophys. Res.*, 90, 11,431–11,468.
- Hasegawa, A., and Nakajima, J. (2004), Geophysical constraints on slab subduction and arc magmatism, in *The State of the Planet: Frontiers and Challenges in Geophysics*,

- Geophys. Monogr. Ser.*, edited by R. Stephen, J. Sparks, and C. J. Hawkesworth, pp. 81-94 American Geophysical Union, Washington D.C..
- Hayes, G. P., D. J. Wald, and R. L. Johnson (2012), Slab1.0: A three-dimensional model of global subduction zone geometries, *J. Geophys. Res.*, *117*, B01302, doi:10.1029/2011JB008524.
- Hills, E. S. (1963), *Elements of Structural Geology*. Methuen & Co. Ltd., London.
- Hirth, G., and D. L. Kohlstedt (1996), Water in the oceanic upper mantle: implication for rheology, melt extraction, and the evolution of the lithosphere, *Earth Planet. Sci. Lett.*, *144*, 93-108.
- Hirth, G., and D. L. Kohlstedt, (2003), Rheology of the upper mantle and the mantle wedge: A view from the experimentalists, in *Inside the Subduction Factory*, edited by J. Eiler, pp. 83-105, American Geophysical Union, Washington D.C..
- Hochstaedter, A. G., P. Kepezhinskas, M. Defant, M. Drummond, and A. Koloskov (1996), Insights into the volcanic arc mantle wedge from magnesian lavas from the Kamchatka arc, *J. Geophys. Res.*, *101*, 697-712.
- Hsui, A. T., and S. Yongquist (1985), A dynamic model of the curvature of the Mariana Trench, *Nature*, *318*(6045), 455-457.
- Hussong, D. M., and S. Uyeda (1981), Tectonic processes and the history of the Mariana arc: A synthesis of the results of Deep Sea Drilling Project Leg 60, *Initial Rep. Deep Sea Drill. Proj. 60*, 909-929.
- International Seismological Centre (2013), *On-line Bulletin*, <http://www.isc.ac.uk>, Internatl. Seis. Cent., Thatcham, United Kingdom.
- Ishizuka, O., M. Yuasa, R. N. Taylor, and I. Sakamoto (2009), Two contrasting magmatic types coexist after the cessation of backarc spreading, *Chem. Geol.*, *266*, 283-305.

- Jacobs, A. M., A. J. Harding, and G. M. Kent (2007), Axial crustal structure of the Lau backarc basin from velocity modeling of multichannel seismic data, *Earth Planet. Sci. Lett.*, *259*, 239-255.
- Jenner, G. A., P. A. Cawood, M. Rautenschlein, and W. M. White (1987), Composition of backarc basin volcanics, Valu Fa Ridge, Lau basin: Evidence for a slab-derived component in their mantle source, *J. Volcanol. Geotherm. Res.*, *32*, 209-222
- Karato, S.-I., M. Paterson, and J. Fitzgerald (1986), Rheology of Synthetic Olivine Aggregates: Influence of Grain Size and Water, *J. Geophys. Res.*, *91*, 8151-8176.
- Karig, D. E. (1970), Ridges and basins of the Tonga-Kermadec island arc system, *J. Geophys. Res.*, *75*, 239-254.
- Karig, D. E. (1971), Origin and Development of Marginal Basins in the Western Pacific, *J. Geophys. Res.*, *76*, 2,542-2,561.
- Kato, T., J. Beavan, T. Matsushima, Y. Kotake, J.T. Camacho, and S. Nakao (2003), Geodetic evidence of backarc spreading in the Mariana Trough, *Geophys. Res. Lett.*, *30*(12), 1625, doi:10.1029/2002GL016757.
- Keller, N. S., R. J. Arculus, J. Hermann, and S. Richards (2008), Submarine backarc lava with arc signature: Fonualei Spreading Center, northeast Lau Basin, Tonga, *J. Geophys. Res.*, *113*, B08S07, doi:10.1029/2007B005451.
- Kelley, K. A., T. Plank, T. L. Grove, E. M. Stolper, S. Newman, and E. Hauri (2006), Mantle melting as a function of water content beneath backarc basins, *J. Geophys. Res.*, *111*, B09208, doi:10.1029/2005JB003732.
- Key, K., S. Constable, L. Liu, and A. Pommier (2013), Electrical image of passive mantle upwelling beneath the northern East Pacific Rise, *Nature*, *495*, 499-502.
- Kincaid, C., D. W. Sparks, and R. Detrick (1996), The relative importance of plate-driven and buoyancy-driven flow at mid-ocean ridges, *J. of Geophys. Res. Solid Earth*, *101*(B7), 16177-16193.

- Kitada, K., N. Seama, T. Yamazaki, Y. Nogi, and K. Suyehiro (2006), Distinct regional differences in crustal thickness along the axis of the Mariana Trough, inferred from gravity anomalies, *Geochem. Geophys. Geosyst.*, 7, Q04011.
- Kleinrock, M. C., and R. N. Hey (1989), Migrating transform zone and lithospheric transfer at the Galapagos 95.5°W propagator, *J. Geophys. Res. Solid Earth*, 94, 13,859-13,878.
- Kuo, B.-Y., and D. W. Forsyth (1988), Gravity anomalies of the ridge-transform system in the south Atlantic between 31 and 34.5°S: Upwelling centers and variations in crustal thickness, *Mar Geophys Res*, 10(3-4), 205-232.
- Langmuir, C. H., J. F. Bender, and R. Batiza (1986), Petrologic and tectonic segmentation of the East Pacific Rise, 5°30' -14°30' N, *Nature*, 322, 422-429.
- Langmuir, C. H., E. M. Klein, and T. Plank (1992), Petrological systematics of mid-ocean ridge basalts: constraints on melt generation beneath ocean ridges, in *Mantle flow and Melt generation at mid-ocean ridge*, edited by J.P. Morgan, D.K. Blackman, and J.M. Sinton, pp. 183-280, American Geophysical Union, Washington D.C..
- Laughton, A. S., R. C. Searle, and D. G. Roberts (1979), The Reykjanes Ridge crest and the transition between rifted and non-rifted regions, *Tectonophysics*, 55, 173-177.
- Lawver, L. A., and J. W. Hawkins (1978), Diffuse magnetic anomalies in marginal basins: Their possible tectonic and petrologic significance, *Tectonophysics*, 45(4), 323-339, doi:10.1016/0040-1951(78)90167-1.
- Leat, P. T., R. A. Livermore, I. L. Millar, and J. A. Pearce (2000), Magma supply in backarc spreading centre segment E2, East Scotia Ridge, *J. Petrol.*, 41, 845-866.
- Luis, J. F. (2007), Mirone: A multi-purpose tool for exploring grid data, *Computers & Geosciences*, 33, 31-41.
- Macdonald, K. C., S. P. Miller, S. P. Huestis, and F. N. Spiess (1980a), Three-dimensional modeling of a magnetic reversal boundary from inversion of deep-tow measurements, *J. Geophys. Res.*, 85, 3661-3670.

- Macdonald, K. C., D. S. Scheirer, and S. M. Carbotte (1991a), Mid-Ocean Ridges: Discontinuities, Segments, and Giant Cracks, *Science*, v. 253, 986-994.
- Macdonald, K. C. (1982), Mid-ocean ridges: Fine scale tectonic, volcanic and hydrothermal processes within the plate boundary zone. *Annual Review of Earth and Planetary Science*, 10, 155-190.
- Macdonald, K. C., P. J. Fox, S. Miller, S. Carbotte, M. H. Edwards, M. Eisen, D. J. Fornari, L. Perram, R. Pockalny, D. Scheirer, S. Tighe, C. Weiland, and D. Wilson (1992), The East Pacific Rise and its flanks 8-18N: History of segmentation, propagation, and spreading direction based on SeaMARC II and Sea Beam studies, *Mar. Geophys. Res.*, 14, 299-344.
- Martinez, F., P. Fryer, N. A. Baker, and T. Yamazaki (1995), Evolution of backarc rifting: Mariana Trough, 20°-24°N, *J. Geophys. Res.*, 100, 3807-3827.
- Martinez, F., P. Fryer, and N. Becker (2000), Geophysical characteristics of the Southern Mariana Trough, 11°50'N-13°40'N, *J. Geophys. Res.*, 105, 16591-16608.
- Martinez, F., and B. Taylor (2002), Mantle wedge control on backarc crustal accretion, *Nature*, 416, 417-420.
- Martinez, F., and B. Taylor (2003), Controls on backarc crustal accretion: Insights from the Lau, Manus, and Mariana basins, in *Intra-Oceanic Subduction Systems: Tectonic and Magmatic Processes, Special Publications*, vol. 219, edited by R.D. Larter and P.T. Leat, pp. 19–54, Geological Society, London, U.K.
- Martinez, F., and B. Taylor (2006), Modes of Crustal Accretion in Back arc Basins: Inferences from the Lau Basin, in *Back arc Spreading Systems: Geological, Biological, Chemical, and Physical Interactions, Geophys. Monogr. Ser.*, vol. 166, edited by D.M. Christie, et al., pp. 5-30, American Geophysical Union, Washington, D.C..
- Martinez, F., B. Taylor, E. T. Baker, J. A. Resing, and S. L. Walker (2006), Opposing trends in crustal thickness and spreading rate along the backarc Eastern Lau Spreading Center: Implications for controls on ridge morphology, faulting, and hydrothermal activity, *Earth Planet. Sci. Lett.*, 245, 655-672.

- Martinez, F., Kelley, K. A., and Stern, R. J. (2012), Creation and Deformation of Hydrous Lithosphere at the Southern Mariana Margin, *EGU General Assembly 2012*, Vienna, Austria, Abstract EGU2012-6643.
- Martinez, F., R. A. Dunn, and J. D. Sleeper (2013), Seafloor spreading in the Lau-Havre Backarc Basins: from fast to ultra slow, *American Geophysical Union Fall Meeting 2013*, San Francisco, CA, Abstract V21C-2739.
- Masuda, H., and P. Fryer (2015), Geochemical Characteristics of Active Backarc Basin Volcanism at the Southern End of the Mariana Trough, in: *Subseafloor Biosphere Linked to Hydrothermal Systems: TAIGA Concept*, eds. J.-i. Ishibashi et al., 261-273, doi:10.1007/978-4-431-54865-2_20.
- McKenzie, D. P., and R. L. Parker (1967), The North Pacific: an example of tectonics on a sphere, *Nature*, 216, 1276-1280.
- McKenzie, D. P. (1969), Speculations on the consequences and causes of plate motions, *Geophys. J. R. Astr. Soc.*, 18, 1-32.
- Mendel, V., M. Munsch, and D. Sauter (2005), MODMAG, a MATLAB program to model marine magnetic anomalies, *Computers & Geosciences*, 31, 589-597.
- Michael, P. J., Langmuir, C. H., Dick, H. J. B., Snow, J. E., Goldstein, S. L., Graham, D. W., Lehnert, K., Kurras, G., Jokat, W., Muhe, R., and Edmonds, H. N. (2003), Magmatic and amagmatic seafloor generation at the ultraslow-spreading Gakkel ridge, Arctic Ocean, *Nature*, 423, 956-965.
- Millen, D. W., and M. W. Hamburger (1998), Seismological evidence for tearing of the Pacific plate at the northern termination of the Tonga subduction zone, *Geology*, 26(7), 659-662.
- Moberly, R. (1972), Origin of lithosphere behind island arcs, with reference to the western Pacific, in *Studies in Earth and Space Sciences, A Memoir in Honor of Harry H. Hess*,

- Memoir 132*, edited by R. Shagam, R.B. Hargraves, W.J. Morgan, F.B.V. Houten, C.A. Burk, H.D. Holland and L.C. Hollister, pp. 35-55, Geological Society of America, Boulder, Colorado.
- Molnar, P. and T. Atwater (1978), Interarc spreading and cordilleran tectonics as alternates related to the age of subducted oceanic lithosphere, *Earth Planet. Sci. Lett.*, *41*, 330-340.
- National Geophysical Data Center (2006), 2-minute gridded global relief data (ETOPO2) v2, National Geophysical Data Center, NOAA, doi:10.7289/V5J1012Q (accessed 2 Dec 2014)
- Oakley, A. J., B. Taylor, G. F. Moore, and A. Goodliffe (2009), Sedimentary, volcanic, and tectonic processes of the Mariana Arc: Mariana Trough backarc basin formation and the West Mariana Ridge, *Geochem., Geophys., Geosyst.*, *10*, Q08X07, doi:10.1029/2008GC002312.
- Ohara, Y., F. Martinez, M. N. Brounce, I. Pujana, T. Ishii, R. J. Stern, J. Ribeiro, K. Michibayashi, K. A. Kelley, M. K. Reagan, H. Watanabe, T. Okumura, S. Oya, T. Mizuno, and YK14-13 science party (2014) The first Shinkai dive study of the southwestern Mariana arc system, *American Geophysical Union Fall Meeting 2013*, San Francisco, CA, Abstract T53A-4651.
- Parker, R. L. (1973), The Rapid Calculation of Potential Anomalies, *Geophys. J. R. astr. Soc.*, *31*, 447-455.
- Parker, R. L., and S. P. Huestis (1974), The inversion of magnetic anomalies in the presence of topography, *J. Geophys. Res.*, *79*, 1587-1593, doi:10.1029/JB079i011p01587.
- Parmentier, E. M., and J. Phipps Morgan (1990), Spreading-rate dependence of three-dimensional structure in oceanic spreading centers, *Nature*, *348*, 325-328.

- Parson, L. M., J. A. Pearce, B. J. Murton, and R. A. Hodkinson (1990), Role of ridge jumps and ridge propagation in the tectonic evolution of the Lau backarc basin, southwest Pacific, *Geology*, *18*, 470-473, doi:10.1130/0091-7613(1990)018<0470: RORJAR>2.3.CO;2.
- Parson, L. W., and D. Tiffin (1993), Northern Lau Basin: Backarc extension at the leading edge of the Indo-Australian Plate, *Geo-Mar. Lett.*, *13*, 107-115.
- Pearce, J. A., M. Ernewein, S. H. Bloomer, L. M. Parson, B. J. Murton, and L. E. Johnson (1995), Geochemistry of Lau basin volcanic rocks: Influence of ridge segmentation and arc proximity, in *Volcanism Associated With Extension at Consuming Plate Margins*, vol. 81, edited by J.L. Smellie, pp. 53-75, Geol. Soc. Spec. Publ., London, U.K., doi:10.1144/GSL.SP.1994.081.01.04.
- Phipps Morgan, J. (1997), The generation of a compositional lithosphere by mid-ocean ridge melting and its effect on subsequent off-axis hotspot upwelling and melting, *Earth Planet. Sci. Lett.*, *146*, 213-232.
- Pierce, C., I. M. Turner, and M. C. Sinha (2001), Crustal structure, accretionary processes and rift propagation: a gravity study of the intermediate-spreading Valu Fa Ridge, Lau Basin, *Geophys. J. Int.*, *146*, 53-73.
- Pelletier, B. and R. Louat (1989), Seismotectonics and present day relative plate motions in the Tonga-Lau and Kermadec-Havre region, *Tectonophysics*, *165*, 237-250.
- Pelletier, B., Y. Lagabriele, M. Benoit, G. Cabioch, S. Calmant, E. Garel, C. Guivel (2001), Newly identified segments of the Pacific-Australia plate boundary along the North Fiji transform zone, *Earth Planet. Sci. Lett.*, *193*, 347-358.
- Perram, L. J., M-H. Cormier, and K. C. Macdonald (1993), Magnetic and Tectonic Studies of the Dueling Propagating Spreading Centers at 20°40'S on the East Pacific Rise: Evidence for Crustal Rotations, *J. Geophys. Res.*, *98*(B8), 13,835-13,850.
- Phillips, D. A. (2003), Crustal motion studies in the southwest Pacific: geodetic measurements of plate convergence in Tonga, Vanuatu, and the Solomon Islands, *PhD Dissertation*,

University of Hawai'i at Mānoa, December 2003, URL:
<http://scholarspace.manoa.hawaii.edu/handle/10125/6903>.

- Plank, T., K. A. Kelley, M. M. Zimmer, E. H. Hauri, and P. J. Wallace (2013), Why do mafic arc magmas contain ~4 wt% water on average?, *Earth Planet. Sci. Lett.*, *364*, 168-179.
- Reches, Z. (1983), Faulting of rocks in three-dimensional strain fields II. theoretical analysis, *Tectonophysics*, *95*, 133-156.
- Reches, Z. and J. H. Dieterich (1983), Faulting of rocks in three-dimensional strain fields I. failure of rocks in polyaxial, servo-control experiments, *Tectonophysics*, *95*, 111-132.
- Reid, I., and H. R. Jackson (1981), Oceanic spreading rates and crustal thickness, *Mar. Geophys. Res.*, *5*(2), 165-172.
- Resing, J., and R. Embley (2012), *R/V Roger Revelle* expedition RR1211/2012, Submarine Ring of Fire-2012 (SRoF-12) Northeast Lau Basin, Sept 9-25 2012 cruise report, <http://oceanexplorer.noaa.gov/explorations/12fire/logs/summary/srof12-cruisereport-final.pdf>.
- Ribeiro, J. M., R. J. Stern, F. Martinez, O. Ishizuka, S. G. Merle, K. Kelley, E. Y. Anthony, M. Ren, Y. Ohara, M. Reagan, G. Girard, and S. H. Bloomer (2013), Geodynamic evolution of a forearc rift in the southernmost Mariana Arc, *The Island Arc* *22*, 453-476.
- Riedel, W. (1929), Zur mechanik geologischer brucherscheinungen. Zentralblatt für Mineralogie, Geologie und paleontologie, *B*, 354-368.
- Ruellan, E., J. Delteil, I. Wright, and T. Mastumoto (2003), From rifting to active spreading in the Lau Basin – Havre Trough backarc system (SW Pacific): Locking/unlocking induced by seamount chain subduction, *Geochem. Geophys. Geosyst.*, *4*(5), 8909, doi:10.1029/2001GC000261.
- Sandwell, D. T., R. D. Muller, W. H. F. Smith, E. Garcia, R. Francis (2014), New global marine gravity model from CryoSat-2 and Jason-1 reveals buried tectonic structure, *Science*, *346*, no. 6205, 65-67, doi: 10.1126/science.1258213.

- Sato, T., M. Mizuno, H. Takata, T. Yamada, T. Isse, K. Mochizuki, M. Shinohara, and N. Seama (2015), Seismic structure and seismicity in the southern Mariana Trough and their relation to hydrothermal activity, in: *Subseafloor Biosphere Linked to Hydrothermal Systems:TAIGA Concept*, eds. J.-i. Ishibashi et al., 229-240, doi:10.1007/978-4-431-54865-2_18.
- Schouten, H., K. D. Klitgord, and D.G. Gallo (1993), Edge-driven microplate kinematics, *J. Geophys. Res. Solid Earth*, 98(B4), 6689-6701.
- Sclater, J. G., J. W. Hawkins, J. Mammerickx, and C.G. Chase (1972), Crustal extension between the Tonga and Lau ridges: petrologic and geophysical evidence, *Geol. Soc. Am. Bull.*, 83, 505-518.
- Seama, N. and K. Okino (2015), Asymmetric Seafloor Spreading of the Southern Mariana Trough Backarc Basin, in: *Subseafloor Biosphere Linked to Hydrothermal Systems: TAIGA Concept*, eds. J.-i. Ishibashi et al., 253-260, doi:10.1007/978-4-431-54865-2_20.
- Sinton, J. M., and P. Fryer (1987), Mariana Trough Lavas from 18-Degrees-N - Implications for the Origin of Back Arc Basin Basalts, *J. Geophys. Res.*, 92(B12), 12782-12802.
- Sinton, J. M., L. L. Ford, B. Chappell, and M. McCulloch (2003), Magma genesis and mantle heterogeneity in the Manus backarc basin, Papua New Guinea, *J. Petrol.*, 44, 159-195.
- Sleeper, J. D., and F. Martinez (2014), Controls on segmentation and morphology along the backarc Eastern Lau Spreading Center and Valu Fa Ridge, *J. Geophys. Res. Solid Earth*, 119, 1678-1700, doi:10.1002/2013JB010545.
- Sleeper, J. D., and F. Martinez (2016), Geology and kinematics of the Niuafu'ou microplate in the northern Lau basin, *J. Geophys. Res. Solid Earth*, 121, doi:10.1002/2016JB013051.
- Sleeper, J. D., F. Martinez, and R. Arculus (2016), The Fonualei Rift and Spreading Center: Effects of Ultraslow Spreading and Arc Proximity on Axial Morphology, *J. Geophys. Res. Solid Earth*, 121, doi:10.1002/2016JB013050.
- Smith, W. H. F., and D. T. Sandwell (1997), Global seafloor topography from satellite altimetry and ship depth soundings, *Science*, 277, 1957-1962.

- Standish, J. J., H. J. B. Dick, P. J. Michael, W. G. Melson, and T. O'Hearn (2008), MORB generation beneath the ultraslow spreading Southwest Indian Ridge (9-25°E): Major element chemistry and the importance of process versus source, *Geochem. Geophys. Geosyst.*, 9(5), Q05004, doi:10.1029/2008GC001959.
- Stern, R. J., Y. Tamura, H. Masuda, P. Fryer, F. Martinez, O. Ishizuka, and S. H. Bloomer (2013), How the Mariana volcanic arc ends in the south, *Island Arc*, 22, 133-148.
- Stolper, E., and S. Newman (1994), The role of water in the petrogenesis of Mariana trough magmas, *Earth Planet. Sci. Lett.*, 121, 293-325.
- Tamura, Y., Y. Tatsumi, D. Zhao, Y. Kido, and H. Shukuno (2002), Hot fingers in the mantle wedge: new insights into magma genesis in subduction zones, *Earth Planet. Sci. Lett.*, 197, 105-116.
- Tatsumi, Y. (1986), Formation of the volcanic front in subduction zones, *Geophys. Res. Lett.*, 13, 717-720.
- Tatsumi, Y., and S. Eggins (1995), *Subduction zone magmatism*, 211 pp., Blackwell Science, Cambridge, Mass., USA.
- Taylor, B., and G. D. Karner (1983), On the evolution of marginal basins, *Rev. Geophys. and Space Phys.*, 21(8), 1727-1741.
- Taylor, B., K. Crook, and J. Sinton (1994), Extensional transform zones and oblique spreading centers, *J. Geophys. Res.*, 99, 19707-19718.
- Taylor, B., K. Zellmer, F. Martinez, and A. Goodliffe (1996), Sea-floor spreading in the Lau backarc basin, *Earth Planet. Sci. Lett.*, 144, 35-40.
- Taylor, B., F. Martinez, and A. Goodliffe (1996a), Rifting, oblique spreading, and an extensional transform zone in the Lau Basin: RN Moana Wave 9603 preliminary cruise report, *SOPAC Cruise Report 145*, 1-29.
- Taylor, B., and F. Martinez (2003), Backarc basin basalt systematics, *Earth Planet. Sci. Lett.*, 210, 481-497.

- Tian, L., P. R. Castillo, D. R. Hilton, J. W. Hawkins, B. B. Hanan, and A. J. Pietruszka (2011), Major and trace element and Sr-Nd isotope signatures of the northern Lau Basin lavas: Implications for the composition and dynamics of the backarc basin mantle, *J. Geophys. Res.*, *116*, B11201, doi:10.1029/2011JB008791.
- Vallier, T. L., G. A. Jenner, F. A. Frey, J. B. Gill, A. S. Davis, A. M. Volpe, J. W. Hawkins, J. D. Morris, P. A. Carwood, J. L. Morton, D. W. Scholl, M. Rautenschlein, W. M. White, R.W. Williams, A. J. Stevenson, and L. D. White (1991), Subalkaline andesite from Valu Fa Ridge, a backarc spreading center in southern Lau Basin: petrogenesis, comparative chemistry, and tectonic implications, *Chemical Geology*, *91*(3), 227-256.
- Von Stackelberg, U., and M. Weidicke (1990), Interpretation of Bottom Photographs from Active Spreading Ridges in the Lau Basin, *Marine Mining*, *9*, 247-270.
- Wallace, L.M., R. McCaffrey, J. Beavan, and S. Ellis (2005), Rapid microplate rotations and backarc rifting at the transition between collision and subduction, *Geology* *33*, 857-860.
- Watanabe, M., K. Okino, and T. Kodera (2010), Rifting to spreading in the southern Lau Basin: Variations within the transition zone, *Tectonophysics*, doi:10.1016/j.tecto.2010.09.001.
- Weissel, J. K. (1981), Magnetic lineations in marginal basins of the western Pacific, *Royal Society of London Philosophical Transactions, ser. A*, v. 300, 223-247.
- Weissel, J. K. (1977), Evolution of the Lau Basin by the growth of small plates, in: *Island Arcs, Deep Sea Trenches, and Back Arc Basin*, edited by M. Talwani and W.C. Pitman, *Maurice Ewing Ser. 1*, pp. 429-436 American Geophysical Union, Washington, D.C..
- Wessel, P., W. H. F. Smith, R. Scharroo, J. F. Luis, and F. Wobbe (2013), Generic Mapping Tools: Improved version released, *EOS Trans. AGU*, *94*, 409-410.
- Wetzel, L. R., D. A. Wiens, and M. C. Kleinrock (1993), Evidence from earthquakes for bookshelf faulting at large offset non-transform ridge offsets, *Nature*, *362*, 235- 237.

- White, S. M., J. D. Meyer, R. M. Haymon, K. C. Macdonald, E. T. Baker, and J. A. Resing (2008), High-resolution surveys along the hot spot-affected Galapagos Spreading Center: 2. Influence of magma supply on volcanic morphology, *Geochem. Geophys. Geosyst.*, 9, Q09004, doi:10.1029/2008GC002036.
- Wiedecke, M., and J. Collier (1993), Morphology of the Valu Fa Spreading Ridge in the Southern Lau Basin, *J. Geophys. Res.*, 98(B7), 11,769-11,782.
- Wiedicke, M., and W. Habler (1993), Morphotectonic Characteristics of a Propagating Spreading System in the Northern Lau Basin, *J. Geophys. Res.*, 98(B7), 11,783-11,797.
- Woodhead, J., S. Eggins, and J. Gamble (1993), High field strength and transition element systematics in island arc and backarc basin basalts: Evidence for multiphase melt extraction and a depleted mantle wedge, *Earth Planet. Sci. Lett.*, 114, 491-504.
- Wysoczanski, R. J., E. Todd, I. C. Wright, M. I. Leybourne, J. M. Hergt, C. Adam, and K. Mackay (2010), Backarc rifting, constructional volcanism, and nascent disorganized spreading in the southern Havre Trough backarc rifts (SW Pacific), *J. Volcanol. Geotherm. Res.*, 190, 39-57.
- Yamazaki, T., N. Seama, K. Okino, K. Kitada, M. Joshima, H. Oda, and J. Naka (2003), Spreading process of the northern Mariana Trough: Rifting-spreading transition at 22°N, *Geochem., Geophys., Geosyst.*, 4(9), 1075, doi:10.1029/2002GC000492.
- Zellmer, K. E. and B. Taylor (2001), A three-plate kinematic model for Lau Basin opening, *Geochem., Geophys., Geosyst.*, 2, Paper number: 2000GC000106.